UNIVERSITY OF CALIFORNIA

Santa Barbara

Marine Methane Biogeochemistry Investigated with Isotope-based Studies in the Field and the Laboratory

A dissertation submitted in partial satisfaction of the

requirements for the degree Doctor of Philosophy

in Marine Science

by

Qianhui Qin

Committee in charge:

Professor David L. Valentine, Chair

Professor Morgan Reed Raven

Professor Elizabeth Wilbanks

March 2024

The dissertation of Qianhui Qin is approved.

Morgan Reed Raven

Elizabeth Wilbanks

David L. Valentine, Committee Chair

March 2024

Marine Methane Biogeochemistry Investigated with Isotope-based Studies in the Field and the Laboratory

ACKNOWLEDGEMENTS

I extend my deepest gratitude to my mentor, Dr. David Valentine. Over the past 8 and a half years, he has exemplified true mentorship, both in science and life. Dave's boundless curiosity, passion, and love for science have been truly inspiring. He has always welcomed ideas and thoughts from fellow students in our lab without hesitation. Besides, he also demonstrated care and consideration as a mentor. I vividly recall the anxiety I felt when I shared news of my pregnancy with him in my second year, fearing the challenges that many female Ph.D. students face. Yet, Dave's genuine congratulations and unwavering support immediately eased my worries. He provided guidance on safety precautions in the lab during my pregnancy, readily approved my maternity leave, and made efforts to secure a research assistantship for me for the two quarters after I had my baby. Furthermore, when the pandemic broke out, Dave graciously accommodated my need to return to my home country, navigating all the ensuing changes and challenges with grace.

I owe thanks to my committee members, Dr. Morgan Raven and Dr. Elizabeth Wilbanks. I somehow had to rush through both my Ph.D. qualification exam and my Ph.D. dissertation, both times they were incredibly flexible and understanding, despite their busy schedules. I truly appreciate their support.

I am immensely grateful for the unconditional support of my husband, Zuopin, parents, and in-laws. Their selfless contributions of time, resources, and encouragement have been invaluable. They have steadfastly supported my academic journey throughout the years. I would not have been able to complete my Ph.D. without their assistance in sharing childcare and family duties.

I also want to express my gratitude to my daughter, Shuzhan. Despite the challenges of balancing motherhood with Ph.D. studies, she has been a beacon of motivation, infusing our lives with laughter and joy. She has inspired me to strive for personal growth and to foster a nurturing environment for her upbringing.

I'm grateful to UCSB for providing a comprehensive and accommodating academic and cultural environment, as well as all the resources and benefits for graduate students. These factors have made my life as a student parent much easier.

I am indebted to my lab mates, past and present, for their kindness, camaraderie, and acceptance. Their support has been instrumental in my journey, particularly during moments of self-doubt and cultural adjustment.

Special thanks to Dr. Isabella Lin, my psychologist, whose help and guidance has been irreplaceable in navigating the complexities of motherhood and academia.

Lastly, I am grateful to our neighbors, relatives, and friends for their support throughout my Ph.D. journey.

VITA OF Qianhui Qin
March 2024

EDUCATION

Bachelor of Science in Chemistry (Marine Chemistry), Ocean University of China, June 2012
Master of Science in Marine Sciences, The University of Georgia, December 2015
Doctor of Philosophy in Marine Science, University of California, Santa Barbara, March 2024 (expected)

PROFESSIONAL EMPLOYMENT

2012: Technician, Marine Ecology Research Center, the First Institute of Oceanography, State Oceanic Administration of China.
2015-2023: Teaching Assistant/Research Assistant, Department of Earth Science/Marine Science Institute, University of California, Santa Barbara

PUBLICATIONS

Campbell B. J., Sessions A. L., Fox D. N., Paul B. G., **Qin Q.**, Kellermann M. Y., Valentine D. L. (2017). Minimal Influence of [NiFe] Hydrogenase on Hydrogen Isotope Fractionation in H_2-Oxidizing Cupriavidus necator. Frontiers in Microbiology 8, 1886.

Qin, Q., Kinnaman, F. S., Gosselin, K. M., Liu, N., Treude, T., & Valentine, D. L. (2022). Seasonality of water column methane oxidation and deoxygenation in a dynamic marine environment. Geochimica et Cosmochimica Acta, 336, 219-230.

Krause, S. J., Liu, J., Yousavich, D. J., Robinson, D., Hoyt, D. W., **Qin, Q.**, ... & Treude, T. (2023). Evidence of cryptic methane cycling and non-methanogenic methylamine consumption in the sulfate-reducing zone of sediment in the Santa Barbara Basin, California. Biogeosciences, 20(20), 4377-4390.

RECENT AWARDS

2022.4 Interdepartmental Graduate Program in Marine Science Block Grant, UCSB
2021.8 CARES Summer Research Grant, Graduate Division, UCSB

FIELDS OF STUDY

Oceanic methane biogeochemistry
Stable carbon and hydrogen isotopes
Microbiology of marine archaea and bacteria

ABSTRACT

Marine Methane Biogeochemistry Investigated with Isotope-based Studies in the Field and the Laboratory

by

Qianhui Qin

The ocean is a dynamic environment for methane's biogeochemical processes. Three major processes take center stage: biological methanogenesis, anaerobic methane oxidation, and aerobic methane oxidation. These three key methane biogeochemical processes are intricately balanced within the oceanic environment, resulting in minimal methane escaping into the atmosphere. This dissertation aims to integrate fieldwork with laboratory research, combining investigative tools such as chemical measurements, radiotracer incubations, anaerobic cultivation, and stable isotope probing. The objective is to probe the behaviors of aerobic methane oxidation in relation to the ocean's oxygen availability and isotopic signatures during methanogenesis from methyl-based compounds.

Chapters 1 and 2 of my dissertation delve into the effectiveness and efficiency of aerobic methane oxidation in the ocean's water column. The Santa Barbara Basin (SBB) is known for experiencing seasonal deoxygenation and reoxygenation cycles, resulting in fluctuating methane concentrations in the deep water column. In chapter 1, my study comprehensively investigated this seasonal cycle through a nine-month period of repeated sampling and measurement of key parameters associated with methane biogeochemistry in

the deep waters of the SBB. These parameters include oxygen, nitrate, methane concentrations, and the rate of aerobic methane oxidation. My findings revealed a sequential pattern. First, a decline in oxygen concentration was observed to precede a decrease in nitrate concentration. Second, the accumulation of methane followed, with a marked decline in both oxygen and nitrate levels. Finally, changes in the methane oxidation rate, which reflects the activity of the methanotroph community, occurred subsequently, albeit with a slight time lag. I also discovered that the rate of methane oxidation is primarily dependent on the availability of methane within the water column. Furthermore, my research uncovered that the transient methane pulse accompanying the observed oxygen depletion in the SBB triggered the development of a persistent methanotrophic community, even after methane concentrations had returned to normal levels – an ecological memory effect.

In Chapter 2, beyond the analysis of observed trends, I utilized methane concentrations, methane oxidation rates, and vertical methane diffusion to calculate the minimum methane source required for the deep water column. This computation was conducted across a range of contrasting environmental conditions, ultimately revealing that anoxic conditions demand a greater influx of methane into the water column. A comparison to data collected during a 2023 oceanic research expedition revealed an even greater demand for methane input, in the presence of well-established and persistent anoxic conditions.

Chapter 3 of my dissertation is dedicated to investigating mechanistic underpinnings of stable carbon isotope fractionations during methylotrophic methanogenesis by marine archaea. Understanding these mechanistic underpinnings enables the inclusion of methylotrophic methanogenesis in isotopically informed biogeochemical reaction networks for anaerobic environments. This study included wild type methylotrophic methanogens as

well as a mutant strain in which the reduction of methylated substrates is coupled to hydrogen oxidation or acetate oxidation, providing further mechanistic insight of isotopic variations originating at the reaction branch point.

TABLE OF CONTENTS

Chapter 1- Seasonality of Water Column Methane Oxidation and Deoxygenation in a Dynamic Marine Environment

This research was previously published as:

Qianhui Qin, Franklin S. Kinnaman, Kelsey M. Gosselin, Na Liu, Tina Treude, and David L. Valentine (2022) Seasonality of Water Column Methane Oxidation and Deoxygenation in a Dynamic Marine Environment, Geochimica et Cosmochimica Acta, 336: 219-230.

Abstract

Most of the methane input to the world's oceans is intercepted by microorganisms in sediment and the overlying water column and oxidized before it has an opportunity to reach the atmosphere, where it acts as a greenhouse gas. The factors controlling methane consumption in the ocean are not well established and its biogeochemistry in dynamic marine environments is understudied in-part because of challenges in capturing spatial and temporal variability. Our study focused on the factors that structure methane's biogeochemistry in a dynamic marine environment, the Santa Barbara Basin. The deep-water column of the Santa Barbara Basin experiences seasonal oxygen loss and episodic replenishment which we found to be major factors in structuring the accumulation of methane and the rate at which microorganisms consumed that methane. We found the gradual decline in oxygen that commonly occurs through the summer culminated with a pronounced accumulation of methane

in the water column during the fall. Rates of methane oxidation remained low in summer, increased with the buildup of methane in fall, and remained elevated into spring, even after methane concentration had declined. However, results from methane oxidation kinetics experiments revealed a zero-order kinetic dependence on oxygen concentration, indicating that oxygen's effect on methanotrophy at the ecosystem scale is likely indirect. We also captured an apparent mixing event during fall that drove spatial and temporal variability in oxygen, nitrate and methane concentrations in the Santa Barbara Basin, with stark variations at the investigated timescale of 8 days and along isobaths at a spatial scale of 7 km. Collectively, these results indicate the seasonal development and attenuation of a methanotrophic community associated with restricted circulation, but also of a spatiotemporal variability not previously appreciated for this environment.

1. Introduction

The ocean is not a major source of methane to the atmosphere (~ 4-15 Tg yr^{-1}, less than 2.5% of total methane sources, Solomon et al., 2007), even though a significant amount of methane (at least 85 Tg yr^{-1}) is consistently produced in marine environments through microbial or thermal transformation of organic carbon (Hinrichs et al., 1999; Reeburgh, 2007; Zhang et al., 2011; Reay et al., 2018). Instead, anaerobic oxidation of methane (AOM) occurs in marine sediment, and together with aerobic methane oxidation (hereafter MOx) near to the seafloor and in the overlying water column, acts as a biological filter (Reeburgh, 2007; Mau et al., 2013; Torres-Beltrán et al., 2016; Steinle et al., 2017). AOM can consume ~ 75% - 80% of the produced methane in the sediment (Strous and Jetten, 2004; Treude, 2004; Knittel and Boetius, 2009; Torres-Beltrán et al., 2016) and commonly occurs at a banded interface in the

sediment known as the sulfate-methane transition zone. In diffusive systems, AOM usually quantitatively consumes sedimentary methane (Knittel and Boetius, 2009), but in sediments with advective transport or gas ebullition methane can bypass the benthic microbial filter and enter the water column (Reeburgh, 2007; Knittel and Boetius, 2009).

Since the first measurements of dissolved methane concentrations in the ocean's water column were reported in the late 1960s (Reeburgh, 2007), various groups have studied water column methane concentrations and MOx rates in different oceanic environments (Griffiths et al., 1982; Ward et al., 1987, 1989; Reeburgh et al., 1991; de Angelis et al., 1993; Ward and Kilpatrick, 1993; Valentine et al., 2001; Mau et al., 2012, 2013; Heintz et al., 2012; Pack et al., 2015; Steinle et al., 2015, 2016, 2017). Most studies represent snapshots of oceanographic conditions and have collectively demonstrated that the rate of MOx depends on the availability and concentrations of the two substrates of the reaction, methane and oxygen, together with other physicochemical controls like temperature, salinity, nutrients, etc (Ward et al., 1987; Valentine et al., 2001; Mau et al., 2012, 2013; Heintz et al., 2012; Pack et al., 2015; Steinle et al., 2015, 2016).

Many oceanic environments are dynamic because of seasonal, spatial, and other physiochemical factors. Methane concentration and MOx rate variability together control the atmospheric release of methane and knowledge of these processes is therefore import for predicting future changes in methane emissions. Numerous studies have considered the spatial variability of MOx (Reeburgh, 2007; Mau et al., 2012, 2013; Steinle et al., 2016), but fewer studies have considered the temporal variability (Tavormina et al., 2010; Kessler et al., 2011; Heintz et al., 2012; Crespo-Medina et al., 2014; Steinle et al., 2015, 2017; Torres-Beltrán et al.,

2016) and the coupled understanding of spatial and temporal variability for MOx is minimal (Gründger et al., 2021).

The Santa Barbara Basin (SBB) is a depression between the California mainland and the northern Channel Islands. The SBB is physically constrained and experiences seasonal deoxygenation. The maximum water depth is about 589 m at the depocenter and the deep basin is fully enclosed at depths > 475m. The SBB is bounded by a shallow Eastern sill, and exchanges water with the Pacific Ocean over the 475m Western sill. Because of the depth difference between sill and depocenter, SBB bottom waters are poorly circulated and are regularly deoxygenated (to <1 μM O_2) following periods of increased surface productivity (Bograd et al., 2002; Goericke et al., 2015). Low oxygen condition is interrupted ~annually by strong springtime upwelling events where deep-water cascades over the sill from the greater Pacific and into the SBB. In the process, existing bottom waters are flushed and the deep SBB becomes temporarily oxygenated to ~20 μM. The introduced oxygen gets quickly consumed by heterotrophic organisms scavenging organic matter, and the deep water oxygen concentration returns to < 1 μM, typically by the end of summer (Sholkovitz and Gieskes, 1971; Sholkovitz, 1973; Sholkovitz and Soutar, 1975; Reimers et al., 1990; Goericke et al., 2015). SBB bottom water is low in oxygen throughout the year, and is classified as hypoxic seawater (oxygen concentration < 63 μM, according to Middelburg and Levin, 2009). As reference, seawater at a temperature of 5 ℃ and a salinity of 34 PSU, which is typical for SBB deep water, would have an oxygen concentration of ~ 319 μM when in equilibrium with the atmospheric gases at 1 atm pressure (Weiss, 1970).

A temporal perspective for the SBB derives from the long-term hydrographic data set collected by the California Cooperative Oceanic Fisheries Investigations (CalCOFI), since

1986 (https://calcofi.org/data/). A compilation of relevant CalCOFI data (Fig. 1) illustrates the seasonal deoxygenation pattern of the SBB deep water column. Bottom water dissolved oxygen and nitrate typically peak in spring with upwelling events, and then gradually decrease after, until the next upwelling events occur. The seasonal deoxygenation occurs ~ annually, typically coupled with extensive denitrification (Sigman et al., 2003).

The SBB is known for having one of the largest natural methane seep areas in the world, thus many previous studies focused on this environment (Hornafius et al., 1999; Hill et al., 2003; Mau et al., 2007, 2010; Ding and Valentine, 2008; Du et al., 2014; Padilla et al., 2019; Joung et al., 2020). The deeper water column of the SBB has been less studied with regard to methane due to the logistical challenges that arise with monitoring methane-related processes over time. In the deep SBB the methane sources are mainly diagenetic (Warford et al., 1979; Kosiur and Warford, 1979; Li et al., 2009) with methane produced by benthic methanogenic archaea and consumed mainly anaerobically by archaea in the sediment and by aerobic bacteria in the water column (Hinrichs et al., 2003; Pack et al., 2011). This study aims to build on our understanding of methane dynamics in low oxygen marine systems. Our goal is to construct a depth-resolved time series of methane concentration and oxidation rate nested within the seasonal cycle of oxygen decline and renewal in the deep SBB. Furthermore, we also aim to explore the factors influencing kinetics of methane oxidation. In doing so, this study identified unanticipated spatiotemporal variability of key compounds – methane, oxygen and nitrate – within the enclosed reaches of the SBB.

2. Materials and Methods

2.1 Sampling Time and Locations

Our sampling plan involved the collection of deep-water column samples from the SBB throughout a deoxygenation and reoxygenation cycle, with a sampling time span of ~ one year. Within this year, one to two sampling expeditions were executed every month. Restrictions associated with the COVID-19 pandemic prevented any sampling from the end of March 2020, limiting the time span of our study to 266 days. Nonetheless, we were still able to capture key features of the cycle as presented in this work. Sampling was conducted from several different research vessels (Table 1), with the first sampling expedition executed on 2019-6-28, 15 more sampling expeditions (18 more hydrocasts) performed afterwards, with the last sampling expedition conducted on 2020-3-20.

A series of 10 sampling expeditions using UCSB's *R/V Connell* were conducted to collect deep SBB water samples, in order to study the changes of deep SBB water column oxygen, nitrate, and methane concentrations, and MOx rates. During each *R/V Connell* sampling, a rosette equipped with 6 4-liter Niskin bottles was deployed and deep-water samples of six different depths were collected (Table 1). These six depths were selected to emphasize changes in deep water characteristics, especially for depths lower than the western sill (depth > 475m). The in-situ temperature profiles were recorded by a conductivity–temperature–depth (CTD) package (Seabird SBE 19+ V2 SeaCAT Profiler) attached to the rosette.

Five additional hydrocasts were conducted during the AT42-19 BASIN19 cruise (2019-10-29 to 2019-11-10) onboard *R/V Atlantis*, using *R/V Atlantis*' CTD (Seabird 911+) rosette with 24 10-liter Niskin bottles. In-situ temperature was recorded by CTD, in-situ oxygen concentration was recorded by an oxygen sensor that was mounted on the rosette. Water samples were collected for four of these five hydrocasts, from 24 depths. And for the collected

water samples, oxygen concentrations were measured using ODF Winkler titration method, nitrate concentrations were measured by flow injection analysis, methane concentrations were measured using a headspace equilibration method.

Available data from four additional cruises were also used for time series analysis including: water column oxygen concentrations from cruise SR1919 onboard *R/V Sally Ride*, which took place in December 2019 (data provided by Dr. Alyson Santoro); oxygen and nitrate concentration data collected by CalCOFI during three quarterly surveys CalCOFI 1907BH, CalCOFI 1911OC, and CalCOFI 2001RL (Data available on CalCOFI's website).

All samples were collected from three different stations within the deep SBB: CalCOFI station 081.8 046.9 (CalCOFI here after), which lies to the north of the shipping lanes that cut across SBB, with a position of (34.2749, -120.0252); South Depocenter Radius Origin (SDRO), which lies to the south of the shipping lanes, with the position (34.2008, -120.0417); and North Depocenter Radius Origin (NDRO), which also lies to the north of the shipping lane, with the position (34.2625, -120.0313). The distance between station NDRO and SDRO is ~ 7 km. Stations were selected arbitrarily within the depocenter of the SBB, and were treated interchangeably (based on an assumption of lateral homogeneity) when external factors (strong winds, fog, rough seas, shipping traffic) favored access to one station over another. The sampling depths and additional details about samples and measurements are listed in Table 1.

2.2 Dissolved Oxygen Concentration Sample Collection and Measurement

Dissolved oxygen concentration sample collection and measurement were conducted using a University of California, San Diego Oceanographic Data Facility (ODF) designed automated titration system. Deep water samples were collected by Niskin bottles and

introduced into Winkler flasks through Tygon tubing immediately after the Niskin bottles were opened. Per depth, two replicate samples were collected. Each Winkler flask was filled for at least 3 volumes of water to overflow. Temperature was recorded for each sample during the overflow process. After the water sample was collected, manganese chloride and sodium hydroxide-sodium iodide were added below surface of liquid into the flask immediately, then a ground glass stopper was inserted, and the flask was inverted several times to mix the reagents with the seawater. After precipitates formed (~ 30 min), the flasks were inverted several times again to make sure the reagents acted fully. Then the samples were transported to lab with water around the neck of the flask to prevent air from entering the flask during transportation, and then stored in the dark until analysis.

Back in the lab, dissolved oxygen concentration was measured by ODF automated titration system. Sulfuric acid was added just before analyzing to free iodine, and then oxygen concentration was measured by an automated oxygen titrator using photometric end-point detection based on the absorption of 365 nm wavelength ultra-violet light.

2.3 Nitrate Concentration Sample Collection and Analysis

Dissolved nitrate concentration sample collection was conducted following UCSB Marine Science Institute Analytical Lab's requirement. Deep water samples from Niskin bottles were filtered through a 0.4 μm polycarbonate filter introduced into clean, pre-rinsed plastic HDPE 20 mL scintillation vials. ~ 17 mL water was filtered into each vial, and then the vial was capped closed. Per depth, two replicate samples were collected. Dissolved nitrate concentrations were analyzed in the deep-water samples by flow injection analysis (FIA)

according to the procedure described by (Segarra Guerrero et al., 1996) using the QuikChem 8500 Series 2 (Lachat Instruments, Zellweger Analytics Inc.).

2.4 Dissolved Methane Concentration Sample Collection and Analysis

Dissolved methane concentration sample collection and analysis were made as described in Heintz et al., 2012, with the following modifications: Seawater was collected by Niskin bottles and introduced into 120 mL serum bottles using 20-30 cm length Tygon tubing with long glass tips. The serum bottles were filled from bottom to the top and flushed 3 times of their volume to minimize contact of the sampled water with the surrounding air. The serum bottles were then closed carefully without gas bubbles using chlorobutyl stoppers and then crimp sealed. For each depth, duplicate methane concentration samples were collected immediately after oxygen concentration samples. The samples were kept cold during transport back to lab for analysis. Samples were preserved using 0.3 mL of 10M NaOH solution by volume exchange with water. For the *R/V Connell* cruises, samples were preserved upon return to the laboratory, 2-4 hours following collection. For the BASIN19 cruise, samples were preserved shipboard ~ 1 hour after collection. Following addition of the preservative, 10 mL headspace of ultrahigh-purity nitrogen (Airgas Ultra High Purity Grade Nitrogen, Manufacturer Part #:UHP300) was added by displacement into each bottle. Then the sample bottles with headspace were shaken vigorously for 1 minute and left upside down in the dark at 4°C for one day to equilibrate. After equilibration, an aliquot of 2 mL of the headspace was taken out using a syringe and injected to either a Shimadzu GC-14A or Shimadzu GC-8A equipped with flame ionization detector to measure the methane concentration in the headspace. For GC-14A, a 100 µL sample loop and a 3.66 m, 2-mm inner-diameter, n-octane Res-Sil C

packed column (Restek) with N_2 as the carrier gas (20 mL min^{-1} flow rate) were used (Kinnaman et al., 2007). For GC-8A, the same setting was used except that the sample loop was 500 μL. Calibration standards were obtained from Scott Specialty Gasses and Gasco Precision Calibration Mixtures, and a minimum three-point calibration was conducted daily prior to analyzing samples. Analyses were performed both shipboard (for BASIN19 cruise) and upon return to the laboratory (for *R/V Connell* cruises) with the same instrument and standards. All samples were analyzed within 2 weeks.

2.5 Fractional Methane Turnover Rate Sample Collection and Analysis

The fractional methane turnover rate (d^{-1}) is defined as the ratio of the activity of ^3H in the produced water divided by the total activity of ^3H in the sample, then further divided by the incubation time of the sample (days) shown in Eq. 1.

$$\text{Fractional methane turnover rate} = \frac{^3H-H_2O}{^3H-CH_4+^3H-H_2O} * \frac{1}{\text{incubation time}} \quad \text{(Eq. 1)}$$

Sample collection was similar to methane concentrations (see above), except that seawater was introduced to 72 mL serum bottles. Three replicate samples were collected per depth.

The fractional methane turnover rate was analyzed based on the ^3H-labeled methane incubation protocol by Bussmann et al., 2015, with the following modifications: In the lab, approximately 10 μL of gaseous ^3H-CH_4 tracer (~ 0.8 kBq, specific activity 37-740 GBq·$mmol^{-1}$) was added into each sample bottle and the bottle was shaken vigorously for 2 min to facilitate dissolution of methane. Then the samples were kept in the dark at in-situ temperature (5-7°C) and incubated for 68-90 hours. After incubation with ^3H-CH_4 for approximately three days, samples were taken out from the incubator and microbial activity was stopped by adding 0.2 mL 25% H_2SO_4. Then the sample bottles were opened, and immediately a 2 mL aliquot was

pipetted each into two 7 mL scintillation vials. To one of the 7 mL scintillation vials immediately 5 mL scintillation cocktail (Ultima Gold LLT) was added followed by liquid scintillation counting (Beckman LS 6500) to determine $^{3}H\text{-}CH_4$ + $^{3}H\text{-}H_2O$. The aliquot in the other 7 mL scintillation vial was air-bubbled for 5 minutes to remove $^{3}H\text{-}CH_4$ before adding scintillation cocktail and liquid scintillation counting to determine $^{3}H\text{-}H_2O$.

For all sampling expeditions involving methane turnover rate determinations, three additional bottles were prepared the same way as the samples, from three out of the six sampling depths, one sample of each depth, to serve as killed controls. For controls, 0.2 mL 25% H_2SO_4 was added first to stop the microbial activity before the addition of $^{3}H\text{-}CH_4$. For the majority of the samples, the resulting activities in killed controls were several orders of magnitude lower compared to samples. A mathematical test to determine the level of detection was also performed on the methane turnover rate results. Samples whose methane turnover rate values were higher than the average killed control value plus three times of the standard deviation were kept. For the samples with methane turnover rate values lower than the level of detection (21 out of 126 samples), their methane turnover rates were considered zero. For samples with values higher than the level of detection, mean values of controls were subtracted from sample values in order to correct for minor amounts of impurity in the stock solution and any abiotic conversion.

2.6 MOx Rate Calculation

Microbially mediated MOx occurs ideally by the reaction shown in Eq. 2.

$$CH_4 + 2O_2 \rightarrow CO_2 + 2H_2O \qquad \text{(Eq. 2)}$$

We used fractional methane turnover rate and ambient methane concentration to calculate the methane oxidation rate, assuming adherence to the first-order rate law (Eq. 3), and assuming the oxidation rate is proportional to methane concentration (Valentine et al., 2001).

$$r_{ox} = k' \times [CH_4] \quad \text{(Eq. 3)}$$

r_{ox} is the methane oxidation rate (concentration per time), and k' is the effective first-order rate constant ($time^{-1}$). In our experiment setting, k' has the value of the measured fractional methane turnover rate, and $[CH_4]$ is the ambient methane concentration. All methane oxidation rates were calculated according to Eq. 3.

Since we only added a very small amount of ^3H-CH_4 into each sample bottle, the ambient methane concentration was increased insignificantly (~ 0.01-0.04 nM). Therefore, ambient methane concentrations were used for the calculation of MOx.

2.7 Time Course Experiment to Validate Incubation Duration

Incubation time for methane turnover rate measurement was 3 days according to Bussmann et al., 2015. To verify this, a time course experiment was also performed on samples from Connell-092419 to test if the uptake rate of ^3H-CH_4 is linear over the incubation time. Nine samples were collected at each sampling depth (6 sampling depths in total), and then divided into 3 groups of triplicate samples. Each sample was treated the same, with ~ 10 μL ^3H-CH_4 tracer and then incubated in the dark at in-situ temperature for 1, 2, and 2.85 days in group 1, 2, 3, respectively. At the end of the incubation, samples were killed and oxidation rates quantified as described above.

2.8 Oxygen or Methane Concentration as a Control on MOx Rate

Oxygen and methane concentration alteration experiments were performed to test the influence of oxygen and methane concentration on MOx rate (Table 2). The purpose of the two experiments was to test the assumption that MOx in the SBB deep water column follows assumed kinetic behavior. The oxygen concentration alteration experiment was conducted on samples from Connell-100419 (Table 1). Nine samples were collected at each sampling depth, and then divided into 3 groups of triplicate samples. Group 1 had ambient oxygen concentrations (the average value of two measured replicate samples). Group 2 was treated with an addition of 30 μL pure oxygen using a 100 μL gas-tight syringe (SGE, 23G, bevel type tip), which increased the oxygen concentration by 17.6 μM. Group 3 was treated with an addition of 60 μL pure oxygen, which increased the oxygen concentration by 35.2 μM. The methane concentration alteration experiment was conducted on samples from Connell-092419 (Table 1). Nine samples were collected at each sampling depth, and then divided into 3 groups of triplicate samples. Group 1 had ambient methane concentrations (the average value of two measured replicate samples). Group 2 was treated with an addition of 4 μL 4% gaseous methane (96% N_2) using a 25 μL gas-tight syringe (SGE, 23G, bevel type tip), which increased the methane concentration by 100 nM. Group 3 was treated with an addition of 12 μL 4% gaseous methane (96% N_2), which increased the methane concentration by 300 nM. For both concentration alteration experiments, 10 μL ^3H-CH_4 tracer was added into each sample bottle after altering initial oxygen or methane of the sample bottle and incubated at in-situ temperature in the dark for 3 days. Fractional methane turnover rates were measured from each incubation, and MOx rate was calculated based on first order kinetics assumption. The

resulting MOx rates were plotted against initial oxygen or methane concentrations to evaluate the influences of oxygen or methane concentrations on MOx.

2.9 Visualization of Time Series Data

Time series maps were generated using Ocean Data View version 5.6.0-64 bit. For each sampling date and each sampling depth, the average value of duplicate (oxygen, nitrate and methane concentrations) or triplicate (MOx rate) samples was used. Gridded fields were calculated using DIVA gridding algorithm, with X scale-length of 400 and Y scale-length of 350. We chose a slightly higher value for X scale-length to highlight the changes with time.

2.10 Depth-Integrated Oxygen and Methane Concentrations

Depth-integrated oxygen and methane concentrations were estimated by calculating the area under the oxygen and methane concentration depth profile curves of 2019-10-30 and 2019-11-07 to demonstrate the spatiotemporal variability of oxygen and methane for this 8-day interval.

3. Results

3.1 Time Series of Water Column Parameters

To describe time-course changes of solute concentrations and MOx rates, we divided the deep SBB water column (440m to bottom) into three layers based on biogeochemical patterns: top layer, 440 – 500 m; middle layer, 500 – 550 m; and bottom layer, 550 m – seafloor. We further divided time by season to capture temporal changes of the measured parameters:

summer (June, July and August); fall (September, October and November); winter (December, January and February); spring (March, April and May).

Oxygen concentrations started at an average of ~ 12 μM in the deep SBB water column in early summer 2019, with the lowest concentration in the middle layer (Fig. 3A). Oxygen concentration subsequently decreased throughout the SBB deep water column, with the bottom layer experiencing the most rapid decline. By early fall 2019, the bottom and middle layers, and the lower part of the upper layer all exhibited oxygen concentration <5 μM. The only exception was the upper reaches of the top layer, which had an oxygen concentration of ~ 10 μM. During this three-month period (June to September), dissolved oxygen decreased by ~ 12 μM for the bottom layer, ~ 4 μM for the middle layer, and ~ 2 μM for the top layer. Low oxygen conditions persisted for fall 2019, with a gradual subsequent increase apparent from winter 2019.

Nitrate concentration displayed a similar vertical pattern as oxygen concentration in early summer 2019, with the lowest concentration in the middle layer ~ 25 μM, and higher concentrations in the top and bottom layers, ~ 30 μM (Fig. 3B). Nitrate concentration decreased throughout fall 2019, reaching an observed minimum of ~ 19 μM in the bottom layer in mid fall 2019. Starting from January 2020 (mid-winter), nitrate concentration gradually increased with time.

For the five sampling events in summer 2019 (Connell-062819, Connell-071819, Connell-080119, Connell-081319, and Connell-082619), methane concentrations were relatively low throughout the deep water column (Fig. 3C). Even at the deepest sampling depth, methane concentrations were less than 25 nM. Starting from early fall 2019, we observed a substantial increase of methane concentration in the bottom layer. A trend of exponential

increase persisted for about a month and expanded from the bottom to the middle layer. Conversely, the top layer experienced minimal change. Methane concentration reached its peak value at late fall, to ~ 300 nM, followed by a rapid decline. From late October to early November, methane concentration decreased by more than half in the middle and bottom layer. By early spring 2020, deep water methane concentration returned to < 25 nM in the bottom layer.

For the three sampling events in summer 2019 (Connell-062819, Connell-071819, and Connell-080119), MOx rates (Fig. 3D) were low throughout the water column. For the top and middle layers, MOx rates were less than 0.05 $nM \cdot d^{-1}$; for the bottom layer, MOx rates were slightly higher, ~ 0.2 $nM \cdot d^{-1}$. Starting from early fall 2019, MOx rates began to increase. The increase was first observed in the bottom layer, where MOx rates increased to ~ 0.5 $nM \cdot d^{-1}$ on Connell-092419 (early fall), followed by an increased MOx rate in the middle layer. On Connell-100419 (mid fall), bottom layer MOx rates reached a peak value of 2.5 $nM \cdot d^{-1}$. The increase of MOx rates was concurrent with the increase of methane concentration in the deep water column, indicative of an active microbial response. On Connell-102119 (mid fall 2019), MOx rates for the bottom and middle layers remained high; rates declined for the two sampling events in late winter and early spring 2020, though more gradually compared to the abrupt decrease in methane concentration. For the final sampling event on Connell-031920 (early spring 2020), MOx rates were still relatively high compared to the initial sampling events, despite similarly low methane concentration.

3.2 Variability at Short Spatial and Temporal Scales

Time series data collected for this study originated from three stations in the Deep Santa Barbara Basin, which we initially considered to be interchangeable based on the assumption of lateral homogeneity. To test this assumption, we compared the oxygen and methane concentration profiles at two stations (NDRO and SDRO, with a distance of 7 km) sampled in rapid succession on 2019-10-30 and again on 2019-11-07. From the four resulting depth profiles (Fig. 4A, 4B, 4D and 4E) we identify substantial spatial and temporal variability.

On 2019-10-30, the oxygen content of the SBB deep water was similar between SDRO and NDRO, with a consistent decrease from 450 m to 500 m depth and a uniform concentration below 500 m, as is apparent in their difference plot (Fig. 4G). The depth-integrated amount of oxygen was similar for the two stations, 246 $mmol \cdot m^{-2}$ for NDRO and 274 $mmol \cdot m^{-2}$ for SDRO. Methane exhibited somewhat greater variability on this date. While both stations contained similar integrated quantities of methane (17.1 $mmol \cdot m^{-2}$ for NDRO and 17.2 $mmol \cdot m^{-2}$ for SDRO), that methane was distributed to shallower depths at NDRO.

In contrast to the consistency observed between stations on 2019-10-30, substantial heterogeneity was apparent on 2019-11-7. At NDRO, there was an increased amount (~ 220 $mmol \cdot m^{-2}$, from 246 $mmol \cdot m^{-2}$ on 2019-10-30 to 466 $mmol \cdot m^{-2}$ on 2019-11-7) of oxygen in the top layer of the deep SBB, whereas SDRO exhibited substantially increased oxygen (~ 137 $mmol \cdot m^{-2}$, from 274 $mmol \cdot m^{-2}$ on 2019-10-30 to 411 $mmol \cdot m^{-2}$ on 2019-11-7) together in both the top layer and the middle layer. Both stations experienced significant drops in methane concentration throughout the middle and bottom layers of the deep water column. The depth-integrated quantity of methane, dropped by ~ 11.5 $mmol \cdot m^{-2}$ (67% of the amount on 2019-10-30) for NDRO, and dropped by ~ 14.5 $mmol \cdot m^{-2}$ (84% of the amount on 2019-10-30) for SDRO. Station SDRO exhibited a greater methane concentration decline compared to station

NDRO. On 2019-11-7, station SDRO exhibited less integrated oxygen (~ 55 $mmol \cdot m^{-2}$) and methane (~ 2.8 $mmol \cdot m^{-2}$) throughout the deep water column compared to station NDRO, as shown by Fig. 4H.

3.3 Kinetic Controls on Methanotrophic Bacterial Community

In order to assess the efficacy of our approach to methane oxidation rate measurement in the SBB, we conducted 3 experiments (time course incubation experiment, oxygen concentration alteration experiment, and methane concentration alteration experiment) to determine how the metabolism of the methanotrophic microbial community varied with respect to duration of incubation and supplementation of substrates – methane and oxygen. Due to limited sample volume available per sampling, each experiment was performed during a different sampling expedition.

Results from time course incubations (samples from Connell-092419), including sample sets for six different depths each collected at three different times, indicate a linear consumption of substrate over time for each sample set – between 1 and 3 days of incubation (Fig. 5A). In turn, these results indicate a constant rate of metabolism by the methanotrophic community over this period of time, for each sample set. The implication of this observation is that the metabolic rate of the methanotrophic community tends to be consistent for a given set of conditions in the incubations, as has been observed in other systems (Bussmann et al., 2015).

Results from the oxygen concentration alteration experiment (samples from Connell-100419) are displayed in Fig. 5B, which was designed to assess the effect of oxygen on the rate of methane consumption for the low-oxygen waters of the SBB. In this case, sample sets

from six different depths were amended with oxygen to achieve three different oxygen concentrations. The results show no appreciable impact of oxygen concentration on the rate of consumption, even for the samples collected at depths with ambient oxygen of < 5 μM.

Unlike oxygen, methane concentration (samples from Connell-102119) exhibited a linear relationship with oxidation rate for all six sample sets investigated (Fig. 5C). Such a linear relationship has been observed previously (Mau et al., 2013; Bussmann et al., 2015) and is consistent with the kinetic relationship used to derive in-situ rates (Eq. 3).

4. Discussion

4.1 Driving Forces of Methane Concentration and MOx Rate Changes

A comparison of time series changes in oxygen concentration, nitrate concentration, methane concentration and MOx rate (Fig. 3) provides new insight as to how these parameters change over a seasonal deoxygenation and reoxygenation event. From Figure 3 a sequential behavior is apparent in the deep water column, with a decline in oxygen concentration leading the decline of nitrate concentration. Methane accumulation preceded a pronounced decline of oxygen and nitrate. Changes to MOx rate, which reflects the activity of the methanotroph community, followed methane concentration change, with a short lag in time.

Previous studies have demonstrated that anoxic and hypoxic conditions can cause the buildup of methane in the water column (Fanning and Pilson, 1972; Reeburgh, 1976; Reeburgh et al., 1991; Pack et al., 2015). We attribute the seasonal buildup of methane in the deep water column of SBB to the seasonal water column oxygen deprivation. Several factors may contribute to the accumulation of methane. First, seasonal deoxygenation of deep SBB water column usually happens after spring, when primary producers thrive utilizing the upwelled

nutrients (Bograd et al., 2002; Goericke et al., 2015). The increased productivity in the surface supplies the sediment with more organic materials, which may lead to enhanced methanogenesis in shallow sediment layers or suspended particulate matter (Bange et al., 2010; Steinle et al., 2017). Second, the establishment of seasonal deoxygenation in the deep SBB water column after spring coincides with the development of water column stratification, which hinders vertical mixing of water (Steinle et al., 2017). Stratification has been shown to facilitate the accumulation of methane (Naqvi et al., 2010). Third, reduced water column oxygen concentration is expected to reduce the flux of oxygen available to sediment-hosted methanotrophs. This could lead to an increased methane flux from the sediments driven by substrate (oxygen) limitation or habitat reduction for methanotrophs. Importantly, we suggest that water column oxygen deprivation has an indirect (rather than any direct) controlling effect on methane concentration, potentially modulating spatial distributions and activities of methanogenic and or methanotrophic communities and processes.

We attribute the rapid loss of methane in the water column in November 2019 to the highly active methanotroph community that started to develop and grow prior to November, rather than the additional oxygen that appeared in the basin at this time. It is indicated by our oxygen concentration alteration experiment that – even at low oxygen concentration – oxygen is not rate limiting for methanotrophy in the SBB. This implies that additional oxygen would not have a significant influence on MOx rate for the deep SBB methanotroph community. We therefore inferred that the introduced oxygen would have exerted little direct effect on the methane oxidation rate, and further, the methane loss would not be caused by the additional oxygen. Similar results have been observed by Steinle et al. 2017; in their study, MOx rates were the highest for samples with sub-micromolar oxygen concentrations, and increased

oxygen concentrations either resulted in little change or decreased MOx rates. Notably, their samples originated from shallow coastal marine environments.

The methanotroph community increased in activity from June through October of 2019 (summer to fall 2019). The establishment of the methanotroph community is mainly controlled by the availability of methane in the surrounding environment. As shown by our substrate alteration experiments, oxygen concentration is not the direct limiting factor for methanotroph activity across the range tested (3.6 - 47.1 μM), and presumably the same is true for cellular growth. Methane availability, itself modulated by oxygen deprivation, appeared to be the primary factor controlling the establishment of the methanotroph community.

The methanotroph community sustained the elevated activity into February and March of 2020 (late winter and early spring 2020), despite the decline in ambient methane concentrations. The reason methanotrophic activity is sustained in the absence of elevated methane concentrations is unclear. One possible explanation is that even though the methane concentration was low, methane supply (e.g., from sediments) was sufficient to support a more active methanotroph community. Another possible explanation is that the pulse of methane observed in October and November of 2019 might have acted as a "priming" mechanism for the methanotroph community – growing the population size and creating a methane demand that persisted even after the methane was mostly consumed. Finally, low oxygen concentration in the water could also reduce the grazing pressure on methanotrophic bacteria, allowing the community to persist for months in the deep water despite an insufficient methane supply (Devlin et al., 2015; Steinle et al., 2017). Whatever the mechanism, the transient methane pulse that accompanied the observed oxygen loss in the Santa Barbara Basin triggered the development of a methanotrophic community that persisted beyond the period when methane

was elevated. This microbial memory effect is a similar phenomenon observed in the Gulf of Mexico following the transient methane release from Deepwater Horizon (Kessler et al., 2011; Valentine et al., 2012; Crespo-Medina et al., 2014).

4.2 Evidence for an Intrusion Event Over the Western Sill

Evidence for an intrusion event over the western sill is apparent in the comparison of oxygen concentration and density, for stations SDRO and NDRO, on 2019-10-30 and 2019-11-7 (Fig. 6). These plots reveal similar distributions between the two stations on 2019-10-30 giving way to more highly oxygenated waters on 2019-11-7, for both stations. Greater oxygen concentrations on 2019-11-7 indicate a substantial intrusion event, with variability between locations indicating depth dependence for processes that drive the pattern of lateral mixing.

Evidence for an intrusion event over the western sill is also shown by Fig. 4. The increased oxygen concentrations of both stations on 2019-11-7 are consistent with an intrusion of water over the western sill into the deep SBB. The resulting vertical distributions of water masses indicate vertical stratification consistent with isopycnal lenses, blobs or fingers of intruding water spilling over the western sill.

The oxygen inversions observed on 2019-11-7 are similar in form to SBB oxygen profiles sometimes captured by CALCOFI (Fig. 1) and provide useful context in interpreting those data. Specifically, oxygen variability may sometimes represent transient mixing processes along isopycnals that effectively provides a small pulse of oxygen into the deep SBB but does not represent a complete flushing event for which deep water is replaced by cascading waters of higher density.

With the above analysis, we have evidence for the occurrence of an intrusion event over the western sill. However, the substantial decline of integrated methane burden (Fig. 4) in the deep SBB from 2019-10-30 to 2019-11-7 at both NDRO and SDRO is difficult to be explained by this intrusion event, in the absence of a large-scale flushing event. Instead, the available data are consistent with a pulse of methanotrophic activity peaking around this time, after experiencing an exponential increase in September and October (Fig. 3D). The observed exponential growth in methanotrophic activity clearly preceded the intrusion event captured on 2019-11-7. Based on our observations, it is indicated that an interplay of oxygen, mixing, and bacterial population dynamics exerted non-steady-state control on the accumulation and loss of methane in the deep SBB.

5. Conclusions

This study demonstrates that seasonal deoxygenation events can lead to the buildup of deep water column methane concentrations, and in turn prompt the activity of the methanotroph community. The response of the methanotroph community leads to the removal of methane from the deep water column. We also show that MOx rate is dependent on methane but not oxygen concentration even at very low ambient oxygen concentration (the lowest oxygen tested was 3.6 μM). While other factors may structure microbial response to methane in other environments, our results provide a useful case study to understand the time scale and controls that act on the development of a marine methanotrophic community when faced with gradual deoxygenation and episodic rejuvenation. The deep water column of SBB provides a useful example of methane dynamics driven by seasonal oxygen changes. The results provide insights for the understanding of temporal dynamics and environmental controls on the

efficiency of the methanotrophic biofilter in the deep water column. Not only can insights from this work be used to understand methane dynamics in other marine basins, but these results also inform our understanding for how methane dynamics may change in the face of global expansion of oxygen minimum zones.

Acknowledgements

We thank: the *R/V Atlantis* Captain, Crew, and Science Party of Research Cruise AT42-19; Christian Orsini and Christoph Pierre for captaining sample expeditions; UCSB MSI Analytical Lab for analyzing nitrate concentrations; Dr. Craig Carlson's lab for assistance with oxygen concentration measurements; Dr. Alyson Santoro for providing oxygen concentration for December, 2019; Xiadani Moreno for assisting with methane concentration measurements; Dr. Burch Fischer for providing the SBB bathymetry map; as well as UCSB and UCLA radiation safety offices for transporting the ^{3}H-CH_4 tracer. Funding for this work was provided by the US National Science Foundation, NSF OCE-1756947 and OCE-1830033 (to DLV) and OCE-1829981 (to TT).

Research Data

Research Data associated with this article can be accessed at the Biological & Chemical Oceanography Data Management Office, DOIs: https://doi.org/10.26008/1912/bco-dmo.872703.1; https://doi.org/10.26008/1912/bco-dmo.872687.1; https://doi.org/10.26008/1912/bco-dmo.872665.1; https://doi.org/10.26008/1912/bco-dmo.872652.1.

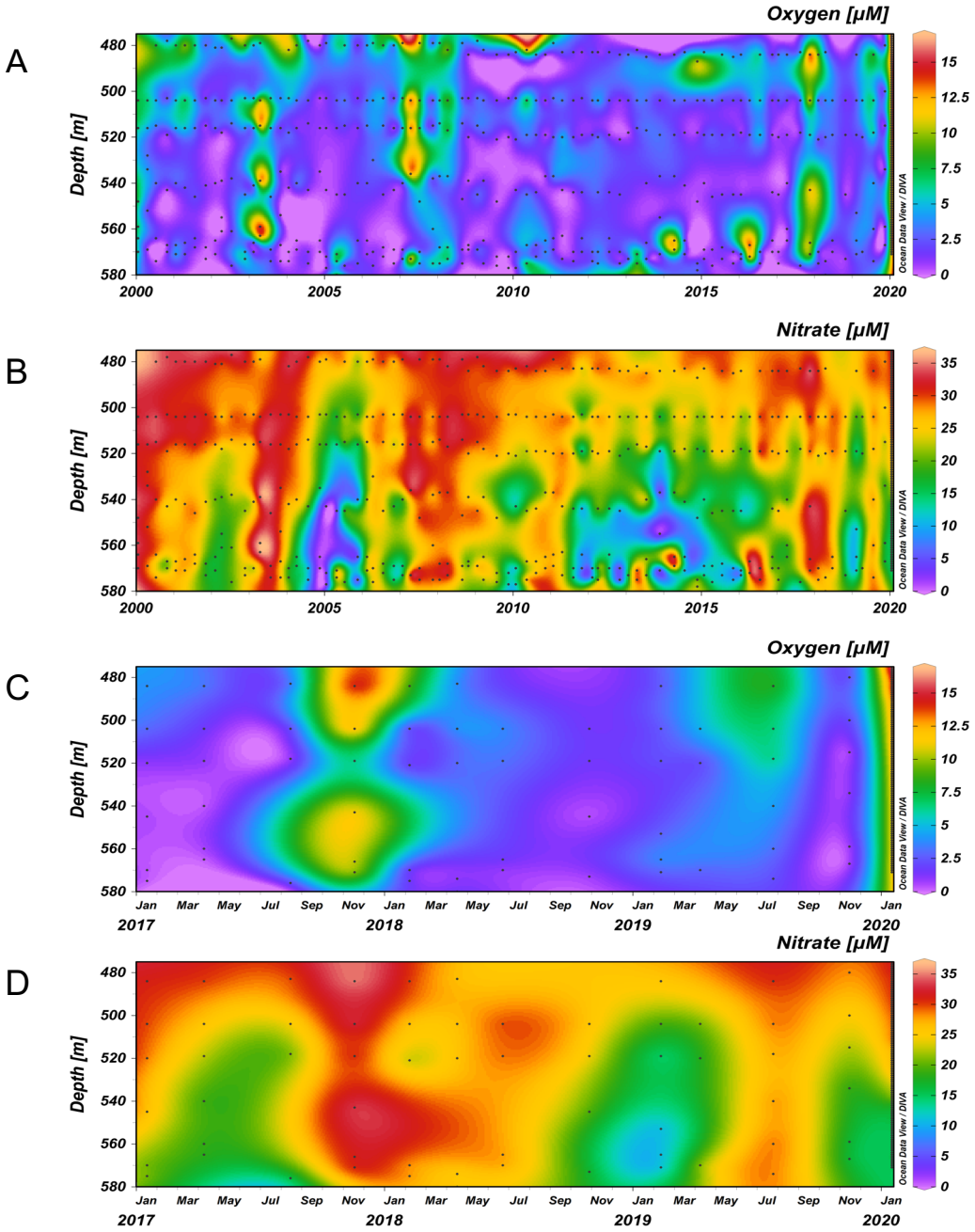

Figure 1. SBB deep water column (475m-580m) heat maps from 2000-2020 of A) oxygen concentration and B) nitrate concentration, as well as higher resolution heat maps from 2017-2020 of C) oxygen concentration and D) nitrate concentration. Black dots represent the original data points, all data are from CalCOFI.

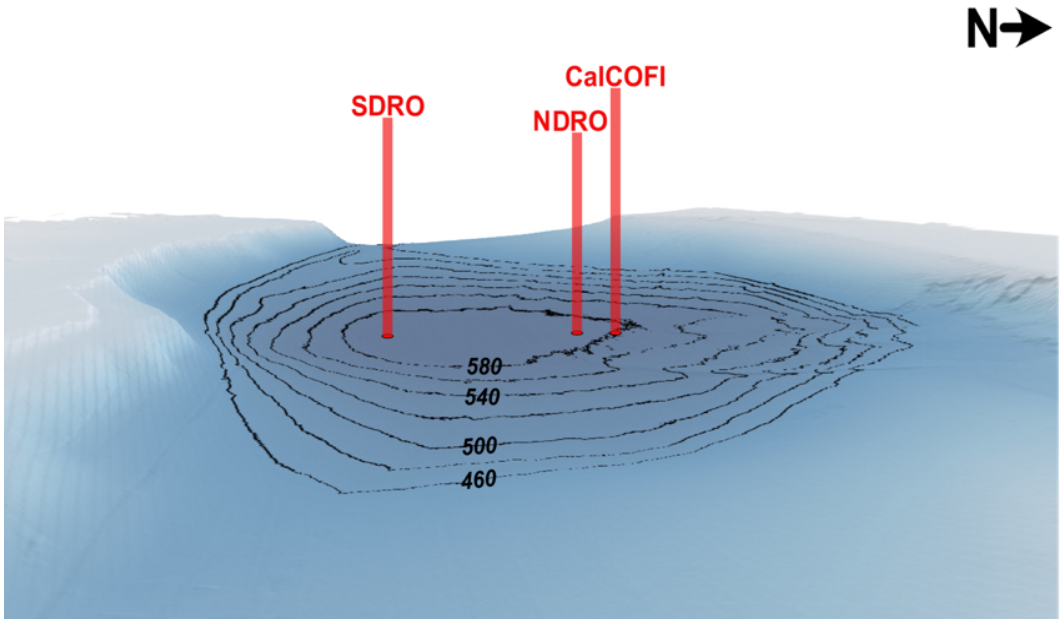

Figure 2. Bathymetry of the deep Santa Barbara Basin including the three sampling stations: SDRO, NDRO, CalCOFI – occupied in this study. The coordinates of the stations are: Station SDRO, 34.2008 N, 120.0497 W; Station NDRO, 34.2681 N, 120.0433 W; Station CALCOFI, 34.2749 N, 120.0252 W.

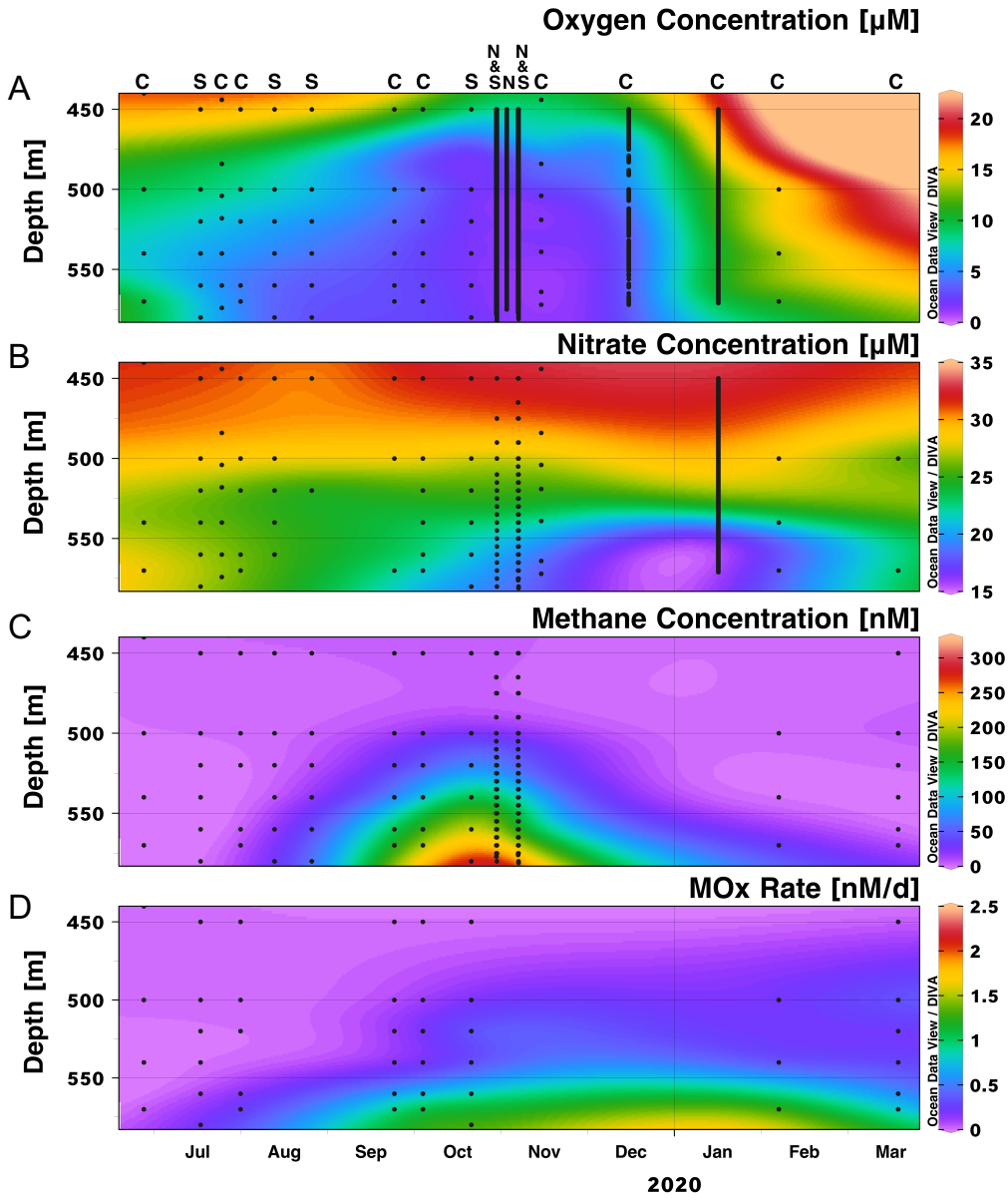

Figure 3. Interpolated time series of (from A to D) oxygen concentration, nitrate concentration, methane concentration and MOx rate of the deep SBB water column (440m-583m) from 2019-6-28 to 2020-3-19. Data are from samples of three sampling stations: SDRO, NDRO, CalCOFI. These three stations within the deep SBB were treated in aggregate and are identified as follows: S=SDRO; N=NDRO; and C= CalCOFI. Black dots denote average value of duplicate (for oxygen, nitrate and methane concentrations) or triplicate (for MOx rate) samples from each depth.

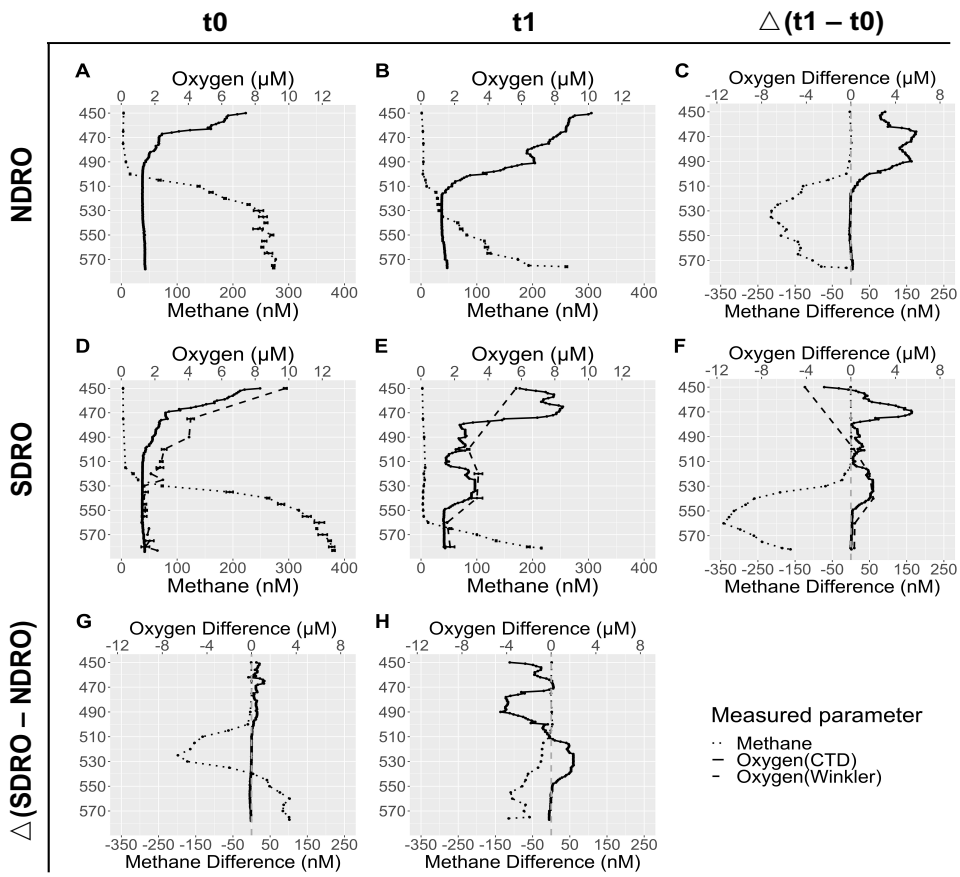

Figure 4. Depth profiles showing the variability of oxygen and methane in the deep water column of the SBB at short spatial and time scales. t0 denotes 2019-10-30, t1 denotes 2019-11-7. t1-t0 describes the difference between 8 days. Dotted lines are measured methane concentration values; Solid lines are oxygen concentration values determined by a CTD-mounted oxygen sensor, while dashed lines are oxygen concentration values determined by Winkler titration. Gray dashed vertical lines in G and H indicate no difference. All the y-axes are depths ranging from 450 m to 584 m. A) Depth profiles of NDRO on 2019-10-30; B) Depth profiles of NDRO on 2019-11-7; C) Time difference profiles of NDRO, positive values indicate concentration increase over time, negative values indicate concentration decrease over time; D) Depth profiles of SDRO on 2019-10-30; E) Depth profiles of SDRO on 2019-11-7; F) Time difference profiles of SDRO; G) Station difference profiles of 2019-10-30, positive values indicate higher concentrations at SDRO, negative values indicate higher concentrations at NDRO; H) Station difference profiles of 2019-11-7.

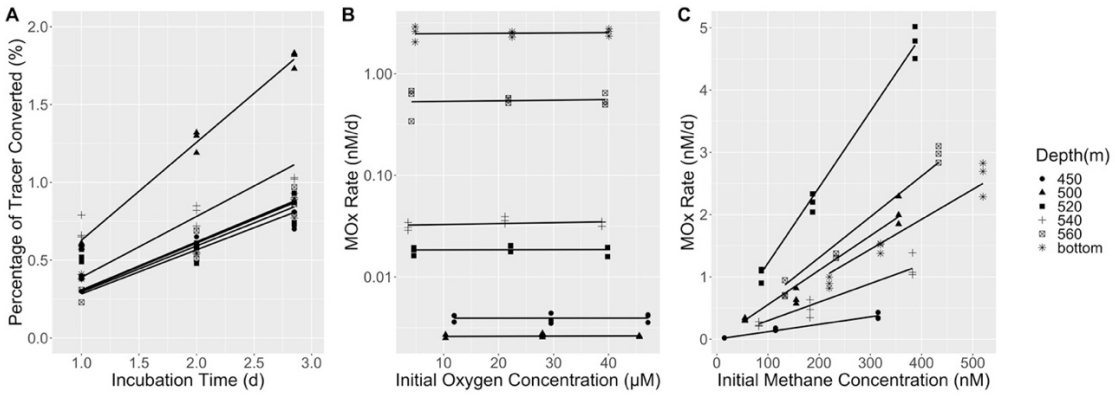

Figure 5. A) Percentage of ^{3}H-CH_4 tracer that was converted to ^{3}H-H_2O during the time-course incubation. Adjusted R^2 values of the linear regressions range from 0.937 - 0.999. B) Influence of the initial oxygen concentration on the resulting MOx rates. Note that the y-axis is on a logarithmic scale. Linear regressions generated for each sampling depth indicate no statistical support for a non-zero slope. C) Influence of the initial methane concentration on the resulting MOx rates. Adjusted R^2 values of the linear regressions range from 0.971 - 0.997. Symbols denote samples from different depths.

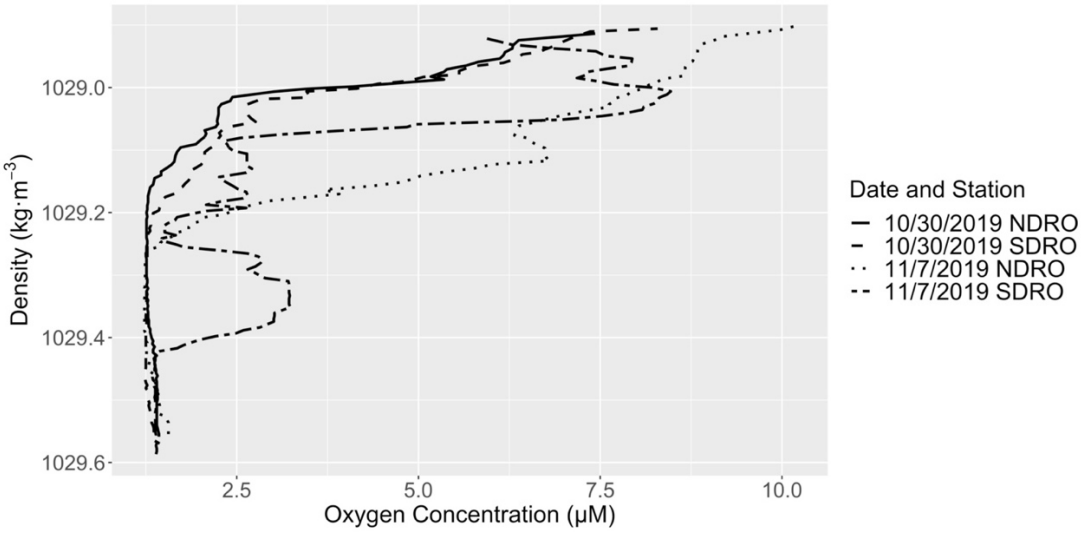

Figure 6. Profiles of density versus oxygen concentration for the SBB deep water column (450 m-bottom). Four profiles are shown and provide additional evidence for an intrusion event from the western sill between 2019-10-30 and 2019-11-7.

Sampling Date	Season	Cruise Number	Station	Sampling Depths (m)	Analyses Performed
6/28/19	Summer	Connell-062819	CalCOFI	50, 300, 440, 500, 540, 570	a, c, e, f
7/18/19	Summer	Connell-071819	SDRO	450, 500, 520, 540, 560, 580	a, c, e, f
7/26/19	Summer	CalCOFI 1907BH	CalCOFI	444, 484, 504, 518, 540, 560, 574	a, c
8/1/19	Summer	Connell-080119	CalCOFI	450, 500, 520, 540, 560, 570	a, c, e, f
2019-08-13*	Summer	Connell-081319	SDRO	450, 500, 520, 540, 560, 580	a, c, e,
2019-08-26*	Summer	Connell-082619	SDRO	450, 500, 520, 540, 560, 580	a, c, e,
9/24/19	Fall	Connell-092419	CalCOFI	450, 500, 520, 540, 560, 570	a, c, e, f
10/4/19	Fall	Connell-100419	CalCOFI	450, 500, 520, 540, 560, 570	a, c, e, f
10/21/19	Fall	Connell-102119	SDRO	450, 500, 520, 540, 560, 580	a, c, e, f
10/30/19	Fall	AT42-19 BASIN19	NDRO	b: 1m resolved from 450-577 e: 450, 465, 475, 490, 500-575 (every 5 m), 577	b, e
10/30/19	Fall	AT42-19 BASIN19	SDRO	a and c: 450, 475, 490, 500, 510-580 (every 5 m), 583 b: 1m resolved from 450-583 e: 450, 475, 515-580 (every 5 m), 583	a, b, c, e
11/3/19	Fall	AT42-19 BASIN19	NDRO	b: 1m resolved from 450-574	b
11/7/19	Fall	AT42-19 BASIN19	NDRO	b: 1m resolved from 450-576 c and e: 450, 465, 475, 490, 500-575 (every 5 m), 576	b, c, e
11/7/19	Fall	AT42-19 BASIN19	SDRO	a: 450, 500, 520, 540, 560, 580 b: 1m resolved from 450-580 c: 450, 475, 490, 500, 510-580 (every 5m), 581 e: 450, 475, 490, 500, 520-580 (every 5m), 581	a, b, c, e
11/15/19	Fall	CalCOFI 1911OC	CalCOFI	440, 480, 500, 515, 534, 559, 567	a, c
12/19/19	Winter	SR1919	CalCOFI	b: 1m resolved from 450-572	b
1/16/20	Winter	CalCOFI 2001RL	CalCOFI	1m resolved from 450-571	b, d
2020-02-06#	Winter	Connell-020620	CalCOFI	500, 560, 570	a, c, e, f
3/19/20	Spring	Connell-031920	CalCOFI	450, 500, 520, 540, 560, 570	a, c, e, f

Table 1. Data and samples used for this study.
The abbreviations stand for the following types of analyses performed:
a = oxygen concentration measured by the Winkler titration method;
b = oxygen concentration measured by the CTD attached oxygen sensor;
c = nitrate concentration;
d = nitrate concentration measured by the CTD attached nitrate sensor;
e = methane concentration;
f = fractional methane turnover rate.
*: Fractional methane turnover rate data of 2019-8-13 and 2019-8-26 were discarded because of sampling apparatus problem.
#: For 2020-2-6, all data of 450, 520 and 540 m were discarded because of sampling apparatus malfunction.

Depth (m)	Group 1/Ambient		Group 2	Group 3
	Average $[O_2]$ (μM)	Percentage difference (%)	$[O_2]$ (μM)	$[O_2]$ (μM)
450	11.9	10	29.5	47.1
500	10.4	1	28	45.6
520	4.6	7.4	22.2	39.8
540	3.6	12.3	21.2	38.8
560	4.2	NA	21.8	39.4
570	4.8	10	22.5	40.1
	Average $[CH_4]$ (nM)	Percentage difference (%)	$[CH_4]$ (nM)	$[CH_4]$ (nM)
450	15	1.7	115	315
500	55	1.5	155	355
520	87	7.6	187	387
540	82	7.2	182	382
560	133	6	233	433
580	220	12.7	320	520

Table 2. Sample and treatment information of the experiments to test controls of MOx rate by oxygen and methane concentrations.

Control of MOx rate by oxygen concentration, samples are from Connell-100419.

Control of MOx rate by methane concentration, samples are from Connell-102119.

References

de Angelis M. A., Lilley M. D., Olson E. J. and Baross J. A. (1993) Methane oxidation in deep-sea hydrothermal plumes of the endeavour segment of the Juan de Fuca Ridge. *Deep Sea Research Part I: Oceanographic Research Papers* **40**, 1169–1186.

Bange H. W., Bergmann K., Hansen H. P., Kock A., Koppe R., Malien F. and Ostrau C. (2010) Dissolved methane during hypoxic events at the Boknis Eck time series station (Eckernforde Bay, SW Baltic Sea). *Biogeosciences* **7**, 1279–1284.

Bograd S. J., Schwing F. B., Castro C. G. and Timothy D. A. (2002) Bottom water renewal in the Santa Barbara Basin. *J. Geophys. Res.* **107**, 9-1-9–9.

Bussmann I., Matousu A., Osudar R. and Mau S. (2015) Assessment of the radio ^{3}H-CH_4 tracer technique to measure aerobic methane oxidation in the water column. *Limnology and Oceanography: Methods* **13**, 312–327.

Crespo-Medina M., Meile C. D., Hunter K. S., Diercks A.-R., Asper V. L., Orphan V. J., Tavormina P. L., Nigro L. M., Battles J. J., Chanton J. P., Shiller A. M., Joung D.-J., Amon R. M. W., Bracco A., Montoya J. P., Villareal T. A., Wood A. M. and Joye S. B. (2014) The rise and fall of methanotrophy following a deepwater oil-well blowout. *Nature Geosci* **7**, 423–427.

Devlin S. P., Saarenheimo J., Syväranta J. and Jones R. I. (2015) Top consumer abundance influences lake methane efflux. *Nat Commun* **6**, 8787.

Ding H. and Valentine D. L. (2008) Methanotrophic bacteria occupy benthic microbial mats in shallow marine hydrocarbon seeps, Coal Oil Point, California. *Journal of Geophysical Research: Biogeosciences* **113**.

Du M., Yvon-Lewis S., Garcia-Tigreros F., Valentine D. L., Mendes S. D. and Kessler J. D. (2014) High Resolution Measurements of Methane and Carbon Dioxide in Surface Waters over a Natural Seep Reveal Dynamics of Dissolved Phase Air–Sea Flux. *Environ. Sci. Technol.* **48**, 10165–10173.

Fanning K. A. and Pilson M. E. Q. (1972) A model for the anoxic zone of the Cariaco Trench. *Deep Sea Research and Oceanographic Abstracts* **19**, 847–863.

Goericke R., Bograd S. J. and Grundle D. S. (2015) Denitrification and flushing of the Santa Barbara Basin bottom waters. *Deep Sea Research Part II: Topical Studies in Oceanography* **112**, 53–60.

Griffiths R. P., Caldwell B. A., Cline J. D., Broich W. A. and Morita R. Y. (1982) Field Observations of Methane Concentrations and Oxidation Rates in the Southeastern Bering Sea. *Appl Environ Microbiol* **44**, 435–446.

Gründger F., Probandt D., Knittel K., Carrier V., Kalenitchenko D., Silyakova A., Serov P., Ferré B., Svenning M. M. and Niemann H. (2021) Seasonal shifts of microbial methane oxidation in Arctic shelf waters above gas seeps. *Limnology and Oceanography* **66**, 1896–1914.

Heintz M. B., Mau S. and Valentine D. L. (2012) Physical control on methanotrophic potential in waters of the Santa Monica Basin, Southern California. *Limnology and Oceanography* **57**, 420–432.

Hill T. M., Kennett J. P. and Spero H. J. (2003) Foraminifera as indicators of methane-rich environments: A study of modern methane seeps in Santa Barbara Channel, California. *Marine Micropaleontology* **49**, 123–138.

Hinrichs K.-U., Hayes J. M., Sylva S. P., Brewer P. G. and DeLong E. F. (1999) Methane-consuming archaebacteria in marine sediments. *Nature* **398**, 802–805.

Hinrichs K.-U., Hmelo L. R. and Sylva S. P. (2003) Molecular Fossil Record of Elevated Methane Levels in Late Pleistocene Coastal Waters. *Science* **299**, 1214–1217.

Hornafius J. S., Quigley D. and Luyendyk B. P. (1999) The world's most spectacular marine hydrocarbon seeps (Coal Oil Point, Santa Barbara Channel, California): Quantification of emissions. *J. Geophys. Res.* **104**, 20703–20711.

Joung D., Leonte M., Valentine D. L., Sparrow K. J., Weber T. and Kessler J. D. (2020) Radiocarbon in Marine Methane Reveals Patchy Impact of Seeps on Surface Waters. *Geophysical Research Letters* **47**, e2020GL089516.

Kessler J. D., Valentine D. L., Redmond M. C., Du M., Chan E. W., Mendes S. D., Quiroz E. W., Villanueva C. J., Shusta S. S., Werra L. M., Yvon-Lewis S. A. and Weber T. C. (2011) A Persistent Oxygen Anomaly Reveals the Fate of Spilled Methane in the Deep Gulf of Mexico. *Science* **331**, 312–315.

Kinnaman F. S., Valentine D. L. and Tyler S. C. (2007) Carbon and hydrogen isotope fractionation associated with the aerobic microbial oxidation of methane, ethane, propane and butane. *Geochimica et Cosmochimica Acta* **71**, 271–283.

Knittel K. and Boetius A. (2009) Anaerobic Oxidation of Methane: Progress with an Unknown Process. *Annual Review of Microbiology* **63**, 311–334.

Kosiur D. R. and Warford A. L. (1979) Methane production and oxidation in Santa Barbara Basin sediments. *Estuarine and Coastal Marine Science* **8**, 379–385.

Li C., Sessions A. L., Kinnaman F. S. and Valentine D. L. (2009) Hydrogen-isotopic variability in lipids from Santa Barbara Basin sediments. *Geochimica et Cosmochimica Acta* **73**, 4803–4823.

Mau S., Blees J., Helmke E., Niemann H. and Damm E. (2013) Vertical distribution of methane oxidation and methanotrophic response to elevated methane concentrations in stratified waters of the Arctic fjord Storfjorden (Svalbard, Norway). *Biogeosciences* **10**, 6267–6268.

Mau S., Heintz M. B., Kinnaman F. S. and Valentine D. L. (2010) Compositional variability and air-sea flux of ethane and propane in the plume of a large, marine seep field near Coal Oil Point, CA. *Geo-Marine Letters* **30**, 367–378.

Mau S., Heintz M. B. and Valentine D. L. (2012) Quantification of CH_4 loss and transport in dissolved plumes of the Santa Barbara Channel, California. *Continental Shelf Research* **32**, 110–120.

Mau S., Valentine D. L., Clark J. F., Reed J., Camilli R. and Washburn L. (2007) Dissolved methane distributions and air-sea flux in the plume of a massive seep field, Coal Oil Point, California. *Geophys. Res. Lett.* **34**, L22603.

Middelburg J. J. and Levin L. A. (2009) Coastal hypoxia and sediment biogeochemistry. *Biogeosciences* **6**, 1273–1293.

Naqvi S. W. A., Bange H. W., Farias L., Monteiro P. M. S., Scranton M. I. and Zhang J. (2010) Marine hypoxia/anoxia as a source of CH_4 and N_2O. *Biogeosciences* **7**, 2159–2190.

Pack M. A., Heintz M. B., Reeburgh W. S., Trumbore S. E., Valentine D. L., Xu X. and Druffel E. R. M. (2011) A method for measuring methane oxidation rates using low-levels of ^{14}C-labeled methane and accelerator mass spectrometry. *Limnology and Oceanography: Methods* **9**, 245–260.

Pack M. A., Heintz M. B., Reeburgh W. S., Trumbore S. E., Valentine D. L., Xu X. and Druffel E. R. M. (2015) Methane oxidation in the eastern tropical North Pacific Ocean water column. *Journal of Geophysical Research: Biogeosciences* **120**, 1078–1092.

Padilla A. M., Loranger S., Kinnaman F. S., Valentine D. L. and Weber T. C. (2019) Modern Assessment of Natural Hydrocarbon Gas Flux at the Coal Oil Point Seep Field, Santa Barbara, California. *Journal of Geophysical Research: Oceans* **124**, 2472–2484.

Reay D. S., Smith P., Christensen T. R., James R. H. and Clark H. (2018) Methane and Global Environmental Change. *Annual Review of Environment and Resources* **43**, 165–192.

Reeburgh W. S. (1976) Methane consumption in Cariaco Trench waters and sediments. *Earth and Planetary Science Letters* **28**, 337–344.

Reeburgh W. S. (2007) Oceanic Methane Biogeochemistry. *Chem. Rev.* **107**, 486–513.

Reeburgh W. S., Ward B. B., Whalen S. C., Sandbeck K. A., Kilpatrick K. A. and Kerkhof L. J. (1991) Black Sea methane geochemistry. *Deep-Sea Research, Part A* **38**, S1189–S1210.

Reimers C. E., Lange C. B., Tabak M. and Bernhard J. M. (1990) Seasonal spillover and varve formation in the Santa Barbara Basin, California. *Limnology and Oceanography* **35**, 1577–1585.

Segarra Guerrero R., Gomezbenito C. and Martinez Calatayud J. (1996) Flow-injection analysis-spectrophotometric determination of nitrite and nitrate in water samples by reaction with proflavin. *Talanta* **43**, 239–246.

Sholkovitz E. (1973) Interstitial water chemistry of the Santa Barbara Basin sediments. *Geochimica et Cosmochimica Acta* **37**, 2043–2073.

Sholkovitz E. R. and Gieskes J. M. (1971) A physical-chemical study of the flushing of the Santa Barbara Basin. *Limnology and Oceanography* **16**, 479–489.

Sholkovitz E. and Soutar A. (1975) Changes in the composition of the bottom water of the Santa Barbara Basin: effect of turbidity currents. *Deep Sea Research and Oceanographic Abstracts* **22**, 13–21.

Sigman D. M., Robinson R., Knapp A. N., van Geen A., McCorkle D. C., Brandes J. A. and Thunell R. C. (2003) Distinguishing between water column and sedimentary denitrification in the Santa Barbara Basin using the stable isotopes of nitrate. *Geochemistry, Geophysics, Geosystems* **4:5**.

Solomon S., Qin D., Manning M., Marquis M., Averyt K., Tignor M. M. B., Miller H. L. Jr. and Chen Z. eds. (2007) *Climate change 2007: The physical science basis*., Cambridge University Press, Cambridge; New York.

Steinle L., Graves C. A., Treude T., Ferré B., Biastoch A., Bussmann I., Berndt C., Krastel S., James R. H., Behrens E., Böning C. W., Greinert J., Sapart C.-J., Scheinert M., Sommer S., Lehmann M. F. and Niemann H. (2015) Water column methanotrophy controlled by a rapid oceanographic switch. *Nature Geosci* **8**, 378–382.

Steinle L., Maltby J., Treude T., Kock A., Bange H. W., Engbersen N., Zopfi J., Lehmann M. F. and Niemann H. (2017) Effects of low oxygen concentrations on aerobic methane oxidation in seasonally hypoxic coastal waters. *Biogeosciences* **14**, 1631–1645.

Steinle L., Schmidt M., Bryant L., Haeckel M., Linke P., Sommer S., Zopfi J., Lehmann M. F., Treude T. and Niemannn H. (2016) Linked sediment and water-column methanotrophy at a man-made gas blowout in the North Sea: Implications for methane budgeting in seasonally stratified shallow seas. *Limnology and Oceanography* **61**, S367–S386.

Strous M. and Jetten M. S. M. (2004) Anaerobic Oxidation of Methane and Ammonium. *Annual Review of Microbiology* **58**, 99–117.

Tavormina P. L., Ussler W., Joye S. B., Harrison B. K. and Orphan V. J. (2010) Distributions of putative aerobic methanotrophs in diverse pelagic marine environments. *ISME J* **4**, 700–710.

Torres-Beltrán M., Hawley A. K., Capelle D. W., Bhatia M. P., Durno E. W., Tortell P. D. and Hallam S. J. (2016) Methanotrophic community dynamics in a seasonally anoxic fjord: Saanich Inlet, British Columbia. *Front. Mar. Sci.* **3:268**.

Treude, T. (2004) Anaerobic oxidation of methane in marine sediments. Doctoral dissertation, Universität Bremen Bremen.

Valentine D. L., Blanton D. C., Reeburgh W. S. and Kastner M. (2001) Water column methane oxidation adjacent to an area of active hydrate dissociation, Eel River Basin. *Geochimica et Cosmochimica Acta* **65**, 2633–2640.

Valentine D. L., Mezic I., Macesic S., Crnjaric-Zic N., Ivic S., Hogan P. J., Fonoberov V. A. and Loire S. (2012) Dynamic autoinoculation and the microbial ecology of a deep water hydrocarbon irruption. *Proceedings of the National Academy of Sciences* **109**, 20286–20291.

Ward B. B. and Kilpatrick K. A. (1993) Methane oxidation associated with mid-depth methane maxima in the Southern California Bight. *Continental Shelf Research* **13**, 1111–1122.

Ward B. B., Kilpatrick K. A., Novelli P. C. and Scranton M. I. (1987) Methane oxidation and methane fluxes in the ocean surface layer and deep anoxic waters. *Letters to Nature* **327**, 226–229.

Ward B. B., Kilpatrick K. A., Wopat A. E., Minnich E. C. and Lidstrom M. E. (1989) Methane oxidation in Saanich inlet during summer stratification. *Continental Shelf Research* **9**, 65–75.

Warford A. L., Kosiur D. R. and Doose P. R. (1979) Methane production in Santa Barbara basin sediments. *Geomicrobiology Journal* **1**, 117–137.

Weiss R. F. (1970) The solubility of nitrogen, oxygen and argon in water and seawater. *Deep Sea Research and Oceanographic Abstracts* **17**, 721–735.

Zhang X., Hester K. C., Ussler W., Walz P. M., Peltzer E. T. and Brewer P. G. (2011) In situ Raman-based measurements of high dissolved methane concentrations in hydrate-rich ocean sediments. *Geophysical Research Letters* **38**, L08605.

Chapter 2 - Methane Budgeting for the Deep Santa Barbara Basin Indicates Seasonal Source Variability

Abstract

This work describes the development of a conceptual simplified three-layer box model for methane dissolved in the deep Santa Barbara Basin water column, including source and sink terms as well as water column inventory. The model is applied to estimate the magnitude of methane source to the deep SBB water column using previously published methane concentration and oxidation rate data collected for contrasting environmental conditions. Results reveal a great discrepancy in needed methane source between oxygenated season (spring and summer) and deoxygenated season (fall and winter), the discrepancy is especially obvious between summer and fall, in the bottom layer. The two exhibit a ~ 13-fold discrepancy, with 103.6 $\mu mol \cdot m^{-2} \cdot d^{-1}$ sedimentary methane entering the deep SBB during the deoxygenated fall season, and 7.7 $\mu mol \cdot m^{-2} \cdot d^{-1}$ sedimentary methane entering in the oxygenated summer season. We also estimated the methanotrophic productivity in the deep SBB for the different seasons. The methanotrophic productivity fluctuated with the oxygen availability of the SBB, with the lowest of 9.1×10^{19} cells produced during the oxygenated summer, and 9.8×10^{20} cells produced in the deoxygenated winter, a difference of ~ 11-fold.

1. Introduction

1.1 Methanogenesis in the Marine Sediments

The conversion of complex organic matter to CH_4 is an essential link in the global carbon cycle. Most organic matter is cycled back to CO_2 for photosynthesis by oxygen-

requiring aerobes; however, a portion of the organic matter enters a diversity of anaerobic environments, where it is decomposed by a consortium of microbes (Ferry and Lessner, 2008). The organic matter is decomposed to CH_4 and CO_2 by a microbial food chain that terminates with methanogens that produce methane primarily by reduction of the methyl group of acetate and also reduction of CO_2. The process occurs in marine environments as well, particularly those receiving large loads of organic matter, such as coastal sediments.

1.2 Aerobic Methane Oxidation

Aerobic methane-oxidizing bacteria (methanotrophs) are distinguished by their ability to use methane (CH_4) as their sole source of metabolic energy and structural carbon. Methanotrophs inhabit a variety of terrestrial and aquatic habitats and play an important role in global carbon, oxygen and nitrogen cycling (Cicerone and Oremland, 1988). Aerobic CH_4 oxidation, together with anaerobic methane oxidation, is the predominant sink mitigating the flux of CH_4, an important greenhouse gas, to the atmosphere (Knowles, 1993). Methanotrophic bacteria can consume up to 80% of the CH_4 produced in freshwater and marine environments (Reeburgh, 2007). Methane oxidation in the ocean is believed to be an important mechanism that modulates the flux of methane from marine waters to the atmosphere, and is treated as a main reason why the ocean in not a major source of atmospheric CH_4 (Ward et al., 1987).

It has been recently studied that even in hypoxic/anoxic conditions, methanotroph-mediated methane oxidation can occur using the hypothesized intra-aerobic AOM pathway (Cheng et al., 2021, 2022). Intra-aerobic AOM is seemingly mediated by NC10 phylum

microbes like Candidatus Methylomirabilis oxyfera (M. oxyfera). M. oxyfera is a denitrifying methanotroph, which uses O_2 produced from NO to intra-aerobically oxidize methane under hypoxic/anoxic conditions. Therefore, there may be previously overlooked aerobic methanotroph-mediated methane oxidation under hypoxic/anoxic conditions, which play a key role in carbon emission control.

1.3 The Influences of Seasonal Deoxygenation on Methane Biogeochemistry

The biogeochemistry of methane in the oceanic water column was initially investigated in water bodies characterized by permanent anoxic conditions/Oxygen Minimum Zones (OMZs hereafter), such as the Black Sea and the Cariaco Basin. In these environments, methane concentrations and methane oxidation rates are notably high and easier to measure. Furthermore, water bodies with sustained anoxic conditions tend to exhibit less variability in their methane concentrations and anaerobic or aerobic methane oxidation rates over time. This characteristic makes it easier to justify model assumptions in these settings.

For the Cariaco Basin, Fanning and Pilson (Fanning and Pilson, 1972), and Reeburgh (Reeburgh, 1976) used a steady state vertical advection-diffusion model to study methane biogeochemistry in the Cariaco Basin and reached the conclusion that the deep basin sediment diagenesis was the methane source. Scranton (Scranton, 1988) challenged the steady state assumption, and used a time-dependent model to study the Cariaco Basin and stated that diagenesis of sediments at all depths was a uniform methane source to the basin.

For the Black Sea, Reeburgh et al created a sink-based methane budget based on the methane concentration and oxidation rate measurements conducted in the water column and

sediments at a central and shelf station in July 1988 (Reeburgh et al., 1991). He reached the conclusion that slope sediments are water column methane sources while abyssal sediments are water column methane sink.

With the increasing concern about the development of more OMZs, both permanent and seasonal, and the advancement of methane biogeochemistry-related measuring techniques, studies have expanded to investigate the influence of seasonal deoxygenation on methane biogeochemistry. Initially, studies focused on methane concentrations and methane oxidation rates in seasonal anoxic oceanic environments, but these studies typically provided snapshots of the studied environment (Lilley et al., 1982; Ward et al., 1989; Ward and Kilpatrick, 1993; Heintz et al., 2012). Subsequently, studies examining longer-term changes in methane biogeochemistry emerged. Capelle et al., 2019 monitored methane concentration changes in the Saanich Inlet over a 7-year period and concluded that methane concentration is greatly impacted and likely controlled by the oxygen availability of the water column. Steinle et al., 2017 conducted a 2-year time-series study, measuring MOx and physicochemical water column parameters in a coastal inlet in the southwestern Baltic Sea (Eckernförde Bay).

Our study focuses on the deep SBB water column, which experiences seasonal deoxygenation according to observations and surveys conducted by the California Cooperative Oceanic Fisheries Investigations (CalCOFI) over the past 38 years. We observed significant changes in methane concentration and aerobic methane oxidation (MOx) rates throughout the seasonal cycle. Based on measurements of oxygen and nitrate concentrations, we anticipate substantial variations in methane concentration and MOx rates during both the deoxygenation and oxygenation cycles.

Besides studying changes in methane concentration and MOx rates, we also aim to employ a simplified sink-based methane budget model for the deep SBB water column. This will enable us to compare variations in the amount of methane entering the deep water column from marine sediment under different environmental conditions throughout the year.

2. Methods

2.1 Oxygen Concentration, Nitrate Concentration, Methane Concentration and Methane Oxidation Rate Sampling and Calculation

Oxygen, nitrate, methane concentrations and methane oxidation rate samplings and measurements were conducted for SBB deep water column (450-580m) from 2019-6-28 to 2020-3-19 as described in the Materials and Methods section of Qin et al., 2022.

2.2 Depth Integration of Oxygen, Nitrate, CH_4 Concentrations and MOx Rate to Show Deep Water Column Seasonal Changes

Depth integration is performed on measured oxygen, nitrate, methane concentrations and MOx rate for total deep water column of SBB (450-580m). For each sampling day, oxygen, nitrate, methane concentrations or MOx rate of the total deep water column is summed to provide depth-integrated values. The integrated oxygen, nitrate, methane concentrations or MOx rate is then plotted against time to generate a time series of depth-integrated parameters.

In addition to the depth-integrated measured parameters, we also examined the depth-integrated methanotrophic oxygen demand, calculated based on the stoichiometry of the aerobic methane oxidation reaction (Eq. 1). It is computed as the ratio of methane concentration to twice the ambient oxygen concentration, providing insight into how the

methanotrophic community's oxygen demand compares to the available oxygen in the environment.

$$CH_4 + 2O_2 \rightarrow CO_2 + 2H_2O \quad \text{(Eq. 1)}$$

2.3 Estimation of the Seasonal Methanotroph Community Productivity

Estimations of the methanotroph community productivity in the SBB during the studied time were calculated. We performed the calculation using the 1m1d resolved MOx rates data. The 1m1d resolved MOx rates are converted to seasonal methanotroph community productivity by the following steps:

1. The seasonal summed MOx rate for each meter of the studied depth (450 m-580 m) is calculated by adding the 1m1d resolved MOx rate for each day of the season together.
2. Multiply the seasonal 1m summed MOx rate by a carbon conversion efficiency of 35% (Leak and Dalton, 1986; Dedysh et al., 2005; Trimmer et al., 2015) and the molar mass of carbon to get the production rate of carbon into the methanotroph biomass (in grams of carbon·L^{-1}) for each 1m depth.
3. Divide the above result by cell carbon percentage of 47% (Leak and Dalton, 1986; Dedysh et al., 2005) to get the methanotroph community's productivity (in grams of biomass·L^{-1}) for each 1m depth.
4. Divide the result from step 3 by methanotroph's assumed cellular biomass (20 fg/cell) (Simon and Azam, 1989; Ducklow and Carlson, 1992; Wear et al., 2015) to get an estimation of the the methanotroph community's productivity (in cells·L^{-1}) for each 1-m depth across the deep SBB water column.

5. Multiply the result from step 4 by the 1m resolved SBB water volume for each corresponding depth, and then add the products together to get an estimation of the total methanotroph community's productivity (in cells) during the applicable season.

2.4 Three-layer Box Model

A simple three-layer box model (Fig. 1) is developed to calculate the methane sinks of each layer and to estimate the magnitude of methane source needed in each layer in the SBB deep water column. The SBB deep water column is artificially divided into three layers for better describing of the characteristics of the deep water column. Top layer: 450-500 m, middle layer: 501-550 m, bottom layer 551-580 m. We assume that the deep water column is laterally homogeneous, which means there is no horizontal turbulent diffusion. The model includes the following two methane sinks: sink 1- methane loss caused by aerobic methane oxidation in the water column, sink 2 - methane loss caused by vertical turbulent diffusion between adjacent layers. We consider the sedimentary methane flux from the bottom and slopes as the main source of methane to the water column.

Our research spanned a total of 266 days, from June 28, 2019, to March 19, 2020. To provide a more comprehensive depiction of seasonal methane source and sink changes, we extended the model timeframe to cover a full year. This extension was achieved by assuming that the trend of change between June 1, 2019 to June 28, 2019, is identical to the trend between June 28, 2019 to July 18, 2019 (linear extrapolation). Additionally, we assume that on June 1, 2020, methane concentration and MOx rate were equivalent to those on June 1, 2019. Changes are assumed to be linear between March 19, 2020 and June 1, 2020 and follow the trend before March 19, 2020 (linear extrapolation). As a result, our model covers a

complete year, from June 1, 2019, to June 1, 2020. We also divide our model time span into four seasons: summer-June, July and August of 2019; fall-September, October and November of 2019; winter-December of 2019, and January, February of 2020; spring-March, April and May of 2020, to compare methane sink and source changes between seasonally contrasting environmental conditions. For the four seasons, we roughly categorize fall, and winter as the deoxygenation phase, spring and summer as the reoxygenation phase. Within each season, we assume the dissolved methane in the water column is at steady state, which means the source equals the sinks. This assumption is made in order to calculate the source of dissolved methane based on the sink terms. On top of that, we also considered the change in methane inventory between seasons to cover any additional methane source needed for the season. Need to note, we did not consider the water exchanges between the SBB and the Pacific Ocean in our simplified three-layer box model.

2.5 Calculation and Estimation of Key Parameters

2.5.1 1m Resolved Water Volume of the SBB

1m resolved SBB water volume data was obtained from Dr. David Valentine from previous research of the SBB.

2.5.2 1m1d Resolved CH_4 Concentration and MOx Rate

We employed the linear interpolation method, assuming linear vertical changes between adjacent measured depths and linear temporal changes between the same depth for adjacent sampling trips. This approach enabled us to derive CH_4 concentrations and MOx rates resolved to 1 meter and 1 day (1m1d hereafter) for the entire study period.

2.5.3 Seasonal Average CH_4 Concentration, Seasonal Average Daily MOx Rate, and Seasonal Average Methane Turnover Time

The seasonal average CH_4 concentration for each layer is determined by summing the 1m1d resolved CH_4 concentrations for the corresponding season and layer, and then dividing the result by the product of the total days in the season and the total depth of the layer.

Likewise, the seasonal average daily MOx rate for each layer was calculated by summing the 1m1d resolved daily MOx rates for the corresponding season and layer and then dividing the result by the product of the total days in the season and the total depth of the layer.

The seasonal average methane turnover time is calculated by dividing the seasonal average methane concentration of the layer by the seasonal average daily MOx rate of the same layer.

2.5.4 Seasonal CH_4 Inventory

The seasonal CH_4 inventory is calculated by summing the 1m1d CH_4 concentrations for the same depth over the course of the season, multiplying the result by the volume of water at that depth, and finally summing the values for all depths within the layer.

2.5.5 Seasonal Methane Loss by Aerobic Methane Oxidation

The seasonal methane loss due to aerobic methane oxidation is calculated by summing the 1m1d MOx rates for the same depth throughout the season, multiplying the

result by the volume of water at that depth, and finally summing these values for all depths within the layer.

2.5.6 Vertical Turbulent Diffusion Flux of Methane

Vertical turbulent diffusion flux of methane was calculated between the adjacent layers with Fick's first law of diffusion:

$$\text{Diffusion flux} = D_v \frac{\partial C}{\partial x} \quad \text{(Eq. 2)}$$

where D_v is the vertical turbulent diffusion coefficient in $m^2\ s^{-1}$ (or $cm^2\ s^{-1}$), $\frac{\partial C}{\partial x}$ is the spatial concentration gradient in nM m^{-1}. The vertical turbulent diffusion coefficient (D_v) can vary between 10^{-6} and 10^{-3} $m^2\ s^{-1}$ depending on the energy in the water column (wind, tides, etc.) and stratification (Denman and Gargett, 1983; Wunsch and Ferrari, 2004). A D_v of 4-6 $cm^2\ s^{-1}$ was measured by Yu-Chia Chung and Harmon Craig for SBB deep water column during the SBJULY-70 cruise (Broecker et al., 1970; Chung, 1973). For our model, a D_v of 5 $cm^2\ s^{-1}$ is used to calculate the vertical turbulent diffusion between adjacent layers.

For $\frac{\partial C}{\partial x}$, the concentration gradient with depth in the case of vertical diffusion, ∂C is calculated as the methane concentration difference between the adjacent layers. ∂x is calculated as the half of the added depths of the adjacent layers.

The vertical turbulent diffusion flux between the top and middle layers:

$$\text{Diffusion flux (top and middle)} = \frac{D_v(C_{mid} - C_{top})}{(Z_1 + Z_2)/2} \quad \text{(Eq. 3)}$$

The vertical turbulent diffusion between the middle and bottom layers:

$$\text{Diffusion flux (middle and bottom)} = \frac{D_v(C_{bot} - C_{mid})}{(Z_2 + Z_3)/2} \quad \text{(Eq. 4)}$$

The direction of vertical turbulent diffusion flux depends on the concentration difference. Seasonal vertical turbulent diffusion is further calculated by multiplying the vertical diffusion flux by the area of the interface and the length of the season in days.

2.6 SBB Deep Water Column Methane Sink and Source Estimation

We conducted estimations of the methane source in the deep waters of the SBB using two scenarios. In the first scenario, the deep water column methane sink of each layer is calculated by adding the two sinks – the biological methane sink which shows the methane consumption by the methanotroph community, and the physical methane sink which is caused by the vertical turbulent methane transportation between the adjacent layers. Because we assume steady state of methane within each season, the seasonal needed methane source can be calculated as the same value of the sinks. Additionally, we also considered a second scenario, which included the change of methane inventory between current and previous seasons into the estimation of methane source. In this case, if the methane inventory increases from the previous season to the current season, we would subtract the increased inventory from the added methane sink value because the increased methane inventory can be treated as a methane source to the layer. If the opposite happens, then we would add the decreased amount of methane inventory into the sink calculation because the decreased amount can be treated as another methane sink to the layer.

Below are the equations we utilized to calculate the required source of dissolved methane in the deep water column of the SBB.

Scenario 1, only steady state is considered within the season:

methane source = methane sinks = the amount of methane that's oxidized by methanotrophs + the amount of methane that's vertically transported to the adjacent layers.

Scenario 2, methane inventory change from previous season is incorporated into the source calculation:

methane source = (current – previous) season's methane inventory + the amount of methane that's oxidized by methanotrophs + the amount of methane that's vertically transported to the adjacent layers.

If we attribute the methane source to solely sedimentary diffusion, then the sedimentary methane diffusion flux (F) can be calculated by the estimated needed source of CH_4 to each layer divided by the area of the sediment intersected by the layer. The area of sediment intersected by each layer can be simplified as the difference in area between the top and bottom of the layer. However, for the bottom layer, the sediment intersected would be equivalent to the area of the top layer. This is because the bottom layer has both the slope sediments and depocenter sediments. Since the slope for the walls of the basin is very slight, the average slope of the SBB being 2.2° (Eichhubl et al., 2002), this estimation method results in a difference less than 1%.

3. Results and Discussions

3.1 Time Series of Depth-Integrated Water Column Parameters: [O_2], [CH_4], MOx rate, and [NO_3^-]

The integration of measured parameters with depth (Fig. 2) allows us to consider methane accumulation and consumption for the entirety of the deep water column of SBB, in the context of oxygen and nitrate amount changes.

Depth-integrated oxygen (Fig. 2A) started at ~ 1300 mmol·m^{-2} in early summer 2019 and then exhibited a decreasing trend from summer 2019 to mid fall 2019, reaching the lowest amount around late fall 2019 (~ 250 mmol·m^{-2}), prior to a rapid increase to ~ 1500 mmol·m^{-2} in February of 2020 (late winter). Note, however, that integrated oxygen for 2/6/20 is defined by only three depths because of sampling issues. Depth-integrated methane exhibited the inverse pattern, started at ~ 350 μmol·m^{-2} in early summer 2019, increased from summer 2019 to mid fall 2019 to a peak value of ~ 17 mmol·m^{-2}, then decreased afterward.

The methanotrophic oxygen demand was only ~ 0.05% in the summer months (Fig. 2B), indicating there was ample oxygen in the environment to support aerobic oxidation of the ambient methane pool. A rapid increase in methanotrophic oxygen demand was observed during mid fall 2019, with the peak value of 13 % observed in early November, followed by a rapid decrease in mid-November. Afterwards a gradual decrease over three months brought methanotrophic oxygen demand back to very low values. Notably, even the peak relative oxygen demand was only 13 % of the ambient oxygen concentration, indicating that oxygen concentration was not the limiting factor for aerobic methane oxidation during any sampling event. However, it is important to note that methane may be replenished from sedimentary sources, and for select conditions could drive the water column to anoxia.

Depth-integrated MOx rates were low (~ 5 μmol·m^{-2}·d^{-1}) in early summer 2019 and remained low through summer and early fall 2019 (Fig. 2C). Entering October 2019, depth-integrated MOx rates increased rapidly and peaked at the end of October 2019 at ~ 62 μmol·m^{-2}·d^{-1}. The depth integrated MOx rates dropped to about half of the peak value by February 2020 (late winter) but remained elevated relative to the initial values through March 2020 (early

spring 2020). The sustained methanotrophic activity in February and March is readily apparent in the depth-integrated results.

Depth-integrated nitrate from 450 m to the bottom fluctuated between 3050 to 3650 $mmol \cdot m^{-2}$ from early summer 2019 to late fall 2019 (Fig. 2D). Nitrate amount dropped to the lowest value of ~ 2750 $mmol \cdot m^{-2}$ in mid-November 2019. The depth integrated nitrate amount then rebounded, reaching ~ 3200 $mmol \cdot m^{-2}$ by February 2020.

3.2 Productivity of the Methanotroph Community

Our results further provide a quantitative basis to estimate the population growth in methanotrophic bacteria associated with deoxygenation and reoxygenation of the SBB, a useful value for understanding the behavior of wild marine methanotrophic populations. We used our methane oxidation rate time series measurements to interpolate the daily productivity of the methanotrophic community spanning the experimental campaign (6/28/19 – 3/19/20). We further interpolated our depth profiles and extrapolated those values to the full area of the basin in order to scale daily productivity to the full basin. Daily production of methanotrophs by depth bin is displayed in Fig. 3. The top layer and middle layer show similar change patterns over time: slight fluctuation between July to the end of September 2019, and then increased exponentially during October. Then the daily methanotroph production started to decrease until February 2020, followed by rebound in methanotroph production that was tracked from February to March 2020. Since the top and middle layers cover a total of 100 m depth of the deep SBB water column, the two together largely define the change pattern of the total deep SBB's daily methanotroph production. For the bottom layer, the exponential growth stage began earlier than the top and middle layers, it started in

late September, and we attribute this to the bottom layer's proximity to the sedimentary source of methane. A punctuated decrease followed the exponential growth stage, and after the decrease, a slow increase continued until February 2020. There was a decrease from February to March 2020, which contrasts with the top and middle layers.

Using the method described in part 2.3, we calculate a total net population growth of 1.971×10^{21} methanotrophic cells, from 3.74×10^{6} moles of methane and in a total volume of 7.14×10^{13} L deep SBB water. While this value does not account for mortality, it does provide insight as to the magnitude of the methanotrophic community that develops seasonally in this environment. As a point of reference, the pulse of hydrocarbons from the Deepwater Horizon blowout was estimated to drive productivity of ~ 10^{23} cells in the deep Gulf of Mexico (Valentine et al., 2012).

For the seasonal methanotroph community productivity, summer had the lowest productivity, with a total of 9.1×10^{19} cells, fall had an increase in productivity, a total of 3.1×10^{20} cells, winter had the highest productivity, the total number of cells was 9.8×10^{20}, spring also features a high productivity of 5. 9×10^{20} cells. For the three different layers, the top layer had the smallest productivity, even though it has the largest water column volume, followed by the bottom layer, while the middle layer contains the highest number of methanotroph cells throughout the studied time span.

At the interface of anoxic sediment and an oxic water column, the seafloor serves an important role for methane biogeochemistry by providing a stable environment for methanotrophs to capitalize on the concurrent availability of methane and oxygen (Valentine et al., 2001). From part 3.1 and 3.2, we can see that the deoxygenation that occurs in the Santa Barbara Basin appears to undermine the efficacy of this benthic biofilter, allowing

methane to transiently accumulate in the water column. The results of this work demonstrate that such a pulse of methane to the deep SBB drives the development of a methanotrophic community capable of consuming accumulated methane, even with oxygen concentrations below e.g., 5 μM. The consistency of methane oxidation at low oxygen also suggests that methanotrophy may contribute to the breakthrough of the hypoxic barrier (Giovannoni et al., 2021), which states that oxidative enzymes involved in organic matter catabolism are kinetically limited by oxygen at concentrations far higher than the thresholds for respiration. This is presumably because O_2 is directly involved in the first step of methanotrophic metabolism, with kinetics that differ from terminal oxidases.

3.3 Seasonal Average [CH_4], MOx Rate and CH_4 Turnover Time of the Three Layers

From Table 1 and Figure 4, we can observe that, layer-wise, the seasonal average methane concentrations are smallest in the top layer, medium in the middle layer, and largest in the bottom layer. Between seasons, spring exhibited the smallest methane concentration in all three layers, followed by summer with slightly increased methane concentrations in all three layers. Winter showed medium methane concentrations and fall displayed the largest methane concentrations in all three layers. Since seasonal methane inventory of the layers are calculated by the product of seasonal average methane concentration and the water volume of the layers, and the volumes of the layers stay constant for our model, the methane inventory changes follow the same trend with average methane concentration changes.

As for the seasonal average daily MOx rate of the layers, the smallest values are seen in the top layer, slightly increased rates are observed in the middle layer, while the largest values are observed in the bottom layer. Between seasons, MOx rates were the lowest during

summer months, increased in fall, reached the peak values in winter and dropped to lower but still elevated values in winter. Results are shown in Table 1 and Figure 5. Again, because seasonal methane loss by MOx is calculated by multiplying seasonal average daily MOx rate with the 1m resolved volume of the water, the resulting seasonal methane loss by MOx showed same change trends.

The calculated seasonal average methane turnover time, which is shown in Table 1 and Figure 6, is longest in the middle layer, medium in the top layer, and shortest in the bottom layer. The middle layer had relatively high methane concentration with relatively low MOx rate, resulting in long methane turnover time. The bottom layer had high methane concentration, with high MOx rate. The high MOx rate effectively consumed the methane in the bottom layer, resulting in the shortest seasonal average turnover time. For the top layer, the methane concentrations were low, and the MOx rates were very small, the results were long methane turnover times.

The seasonal average CH_4 turnover time is calculated as the ratio of the seasonal average CH_4 concentration divided by the seasonal average MOx rate. From Table 1 and Figure 6, we observe that spring exhibits the lowest CH_4 turnover time due to the combination of low CH_4 concentration and elevated MOx rate during the season. Summer and winter both have medium values of CH_4 turnover time, but for different reasons. In summer, both the CH_4 concentration and MOx rate are very low, resulting in a CH_4 turnover time of 41-139 days for the different layers. In winter, both the CH_4 concentration and MOx rate are much higher compared to summer, but the resulting ratio of the two yields values comparable to those in summer. In fall, CH_4 levels increased sharply from relatively low values to very high values, and the methanotroph community was unable to keep pace.

Consequently, the significantly elevated CH_4 concentration, combined with an increase in the MOx rate that, while elevated, was not very high, resulted in the longest CH_4 turnover time during fall.

In conclusion, regarding seasonal average CH_4 concentration, the order from highest to lowest is bottom layer > middle layer > top layer, and the order of seasons from highest to lowest is fall > winter > summer > spring. As for the seasonal average daily MOx rate, the order from highest to lowest is bottom layer > middle layer > top layer, with the order of seasons being winter > fall > spring > summer (although there are slight order differences for the bottom layer compared to the other layers). Regarding seasonal average CH_4 turnover time, the values we obtained are relatively comparable among the three layers, while among the different seasons, the order from highest to lowest is fall > summer > winter > spring.

We attribute the low methane concentration and MOx rate in summer to the previous spring's consumption of CH_4 by the methanotroph community. In fall, methane concentration increases due to seasonal deoxygenation, while the MOx rate remains relatively low due to the lag time in methanotroph community growth needed to respond to changes in methane concentration in the environment. This is reflected in a longer methane turnover time in fall. In winter, ambient methane concentration begins to decrease due to consumption by methanotrophs, while MOx rates remain high, indicating the highly active methanotroph community in the deep water column of the SBB. Finally, we attribute the extremely low methane concentrations in spring to the continued rapid consumption of CH_4 by the methanotroph community, coupled with potential CH_4 removal resulting from physical flushing and water exchanges caused by spring upwelling events from the Pacific Ocean to the deep SBB. Aerobic methane oxidation rates can still be relatively high due to the

methanotrophs' ability to sustain themselves for a period of time following the previous year's deoxygenation event, resulting in a very short methane turnover time.

3.3 Vertical Diffusion of CH_4 between Adjacent Layers

The vertical diffusion of CH_4 between adjacent layers was calculated using Fick's first law of diffusion, with the results presented in Table 2. Analysis of the results reveals that the majority of vertical transport occurs from the lower layer to the layer above, with the exception of transport in summer between the top and middle layers.

Another notable observation is the significant disparity in the amount of CH_4 vertically transported between the middle and bottom layers compared to that between the top and middle layers. This discrepancy is primarily attributed to the source of dissolved CH_4 in the water column, which is predominantly from sedimentary diffusion. As a result, the CH_4 concentration difference between the bottom and middle layers is larger than that between the middle and top layers.

Seasonally, the vertical diffusion of CH_4 between adjacent layers is highest in fall, followed by winter, summer, and lowest in spring. Since there are no significant changes in the vertical diffusion coefficient (D_v) or the shared area of the adjacent layers, the observed seasonal variations are solely dependent on changes in CH_4 concentration.

3.5 Sink-based Calculation on Needed CH_4 Source for Different Seasons

Two major sinks of dissolved methane are considered and calculated for the studied time span of our research. The first sink is a biological methane sink, and it's the consumption of CH_4 by the methanotroph community. The second sink is a physical methane

sink, and it's the methane that is transported to the adjacent layer(s) by vertical turbulent diffusion. Need to note, for the vertical diffusion transport, it does not necessarily act as a sink, under some conditions, the vertically transported methane can act as a source as well, depending on the direction and amount of vertical diffusion.

The two sinks contribute differently to the total sink across different seasons. In seasons with high CH_4 concentrations in the water column, such as fall and winter, the physical sink makes a larger contribution to the total sink. Conversely, in seasons characterized by high MOx rates, such as spring, the biological sink contributes more significantly to the total CH_4 sink.

We considered two scenarios in our sink-based estimation of required CH_4 sources. In the first scenario, we solely focused on the two methane sinks in the water column, without accounting for methane concentration changes between seasons. This approach assumes a steady state for dissolved methane in the deep SBB water column throughout the study year. Therefore, the estimation of the required CH_4 source equates to the sum of the sinks. The calculated results are presented in Table 3, under the column "Sedimentary flux needed (based on sinks)" and illustrated in Figure 7. In the second scenario, we considered changes in methane inventory between the current and previous seasons. In this case, the source estimation includes the sum of the two sinks, along with the supply/need resulting from methane inventory changes. The calculated results are displayed in Table 3, under the column "Sedimentary flux needed (based on sinks + inventory difference)" and shown in Figure 8.

In both scenarios, the greatest demand for CH_4 input into the deep water column was observed in the bottom layer. In Scenario 1, the bottom layer in fall required a sedimentary CH_4 flux of 103.6 $\mu mol \cdot m^{-2} \cdot d^{-1}$ to support both biological and physical methane sinks. In

Scenario 2, the highest sedimentary methane input across different seasons and layers was needed in the bottom layer during winter, requiring a flux of 91.2 $\mu mol \cdot m^{-2} \cdot d^{-1}$. For most seasons, the top and middle layers required minimal sedimentary methane input, with some even showing negative values. Negative values indicate that no sedimentary input is necessary for the layer; in these instances, sediment may even act as a sink for methane, as sufficient methane can be provided through vertical diffusion transport from adjacent layers.

It is important to note that, in both scenarios, we considered marine sediment as the sole methane source. Therefore, the required sedimentary flux is calculated by dividing the needed CH_4 amount by the intersected sediment area of each layer. However, it's worth acknowledging that sedimentary diffusion may not be the only methane source in the deep water column. Other potential methane sources may include methane production from microanoxic zones, such as detritus and animal guts (Oremland, 1979; de Angelis et al., 1993; de Angelis and Lee, 1994), or aerobic methylphosphonate-driven methane formation in seawater (Karl et al., 2008; Grossart et al., 2011; Tang et al., 2016; von Arx et al., 2023). If other methane sources are taken into consideration or identified, the required sedimentary methane source may be smaller than the calculated results.

Results reveal a great discrepancy in needed methane source between oxygenated season (spring and summer) and deoxygenated season (fall and winter), the discrepancy is especially obvious between summer and fall, in the bottom layer. The two have a ~ 13-fold discrepancy, with 103.6 $\mu mol \cdot m^{-2} \cdot d^{-1}$ sedimentary methane entering the deep SBB during the deoxygenated fall season, and 7.74 $\mu mol \cdot m^{-2} \cdot d^{-1}$ sedimentary methane entering in the oxygenated summer season. We also estimated the methanotrophic productivity in the deep SBB for the different seasons. The methanotrophic productivity also fluctuated with the

oxygen availability of the SBB, with the lowest of 9.1×10^{19} of cells produced in oxygenated summer, and 9.8×10^{20} of cells produced in the deoxygenated winter, a discrepancy of ~ 11-fold.

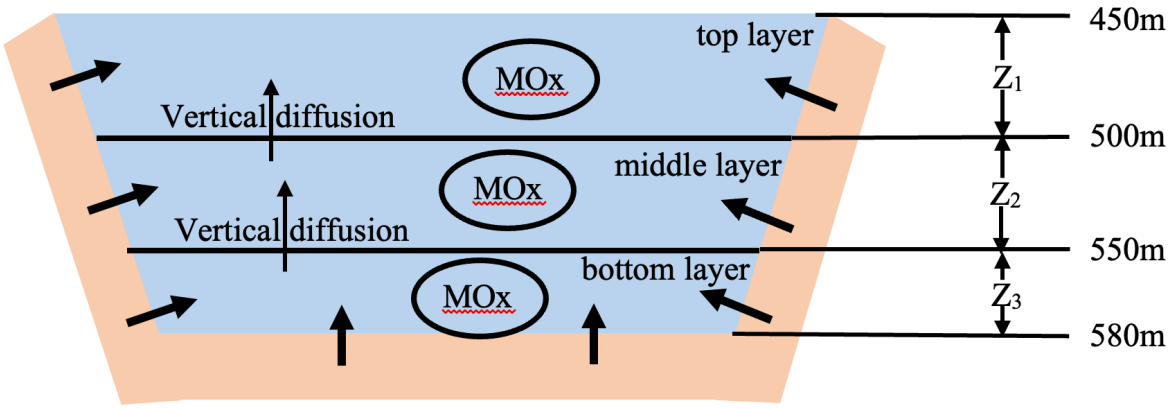

Figure 1. Schematic diagram of the three-layer box model used to describe SBB deep water column methane budget. The deep water column is divided into 3 layers. Z_1, Z_2, and Z_3 denote the depths of the three layers. Z_1=50m, Z_2=50m, Z_3=30m. Black arrows indicate flux terms considered in this box model. The two arrows at the layer interfaces indicate the vertical turbulent diffusion between the two adjacent layers. Need to note, the direction of vertical diffusion depends on the average methane concentration differences between the two adjacent layers. The arrows from benthic and slope sediment to deep water column indicate the supply of methane to the water column by diffusion from the sediments intersected by each layer. The circled MOx in each layer indicates the methane consumption by methanotrophs.

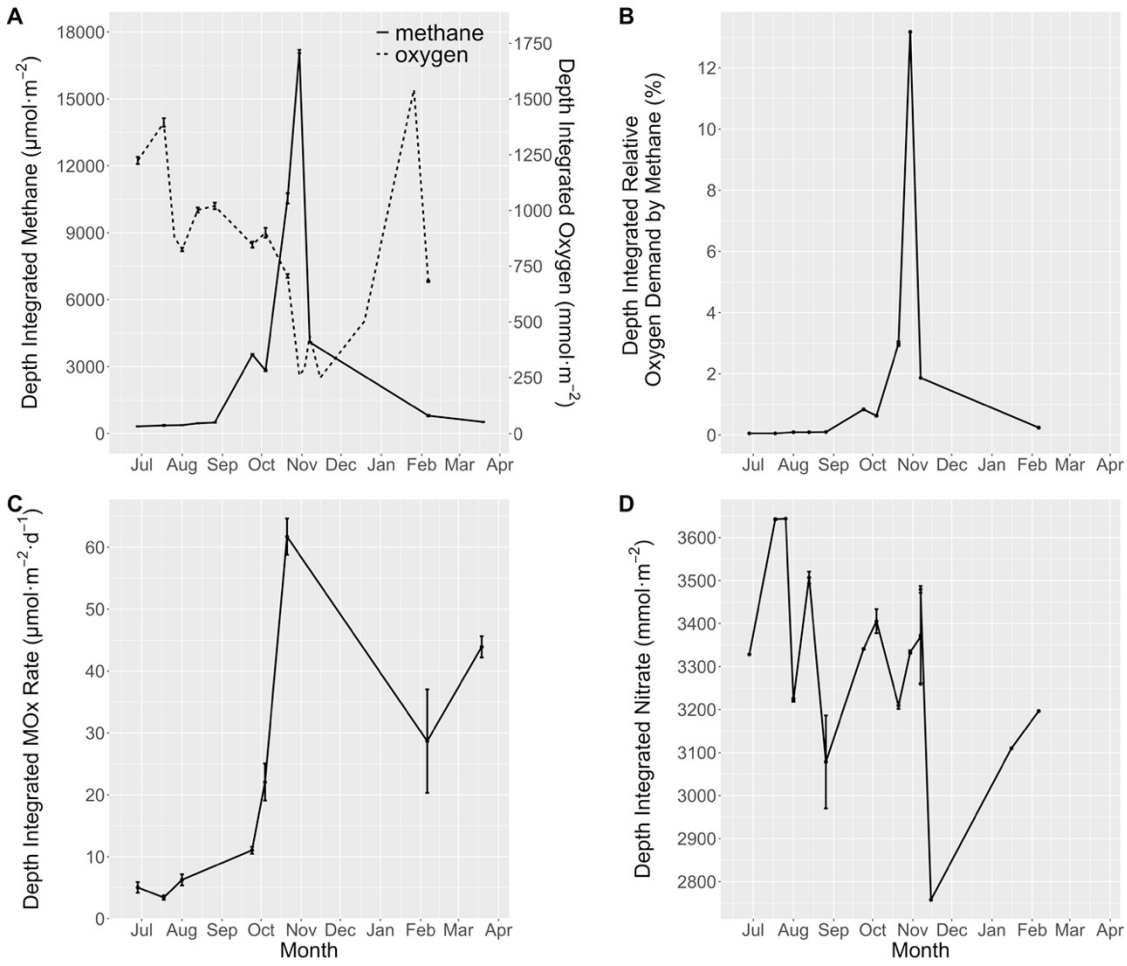

Figure 2. Temporal development of A) depth-integrated oxygen and methane, B) depth-integrated methanotrophic oxygen demand as a percentage of the available ambient oxygen, C) depth-integrated MOx rates. D) depth-integrated nitrate concentrations. Each error bar represents the integrated error from all the depths measured on the corresponding sampling event, as calculated following error propagation equations.

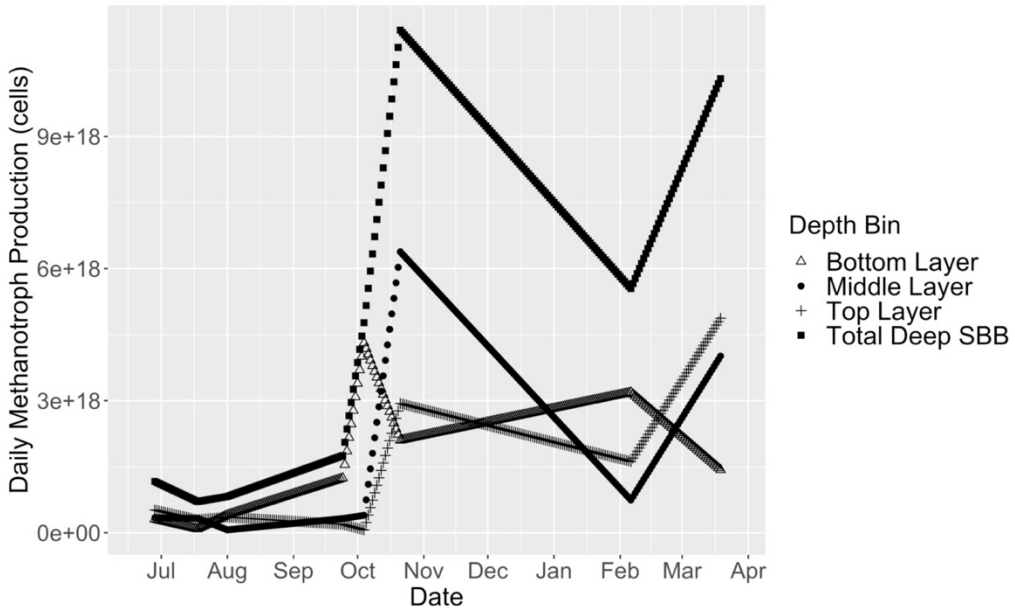

Figure 3. Daily methanotroph production over the research time span. Different symbols denote different depth bins. Bottom layer is 551-580 m, middle layer is 501-550 m, top layer is 450-500 m.

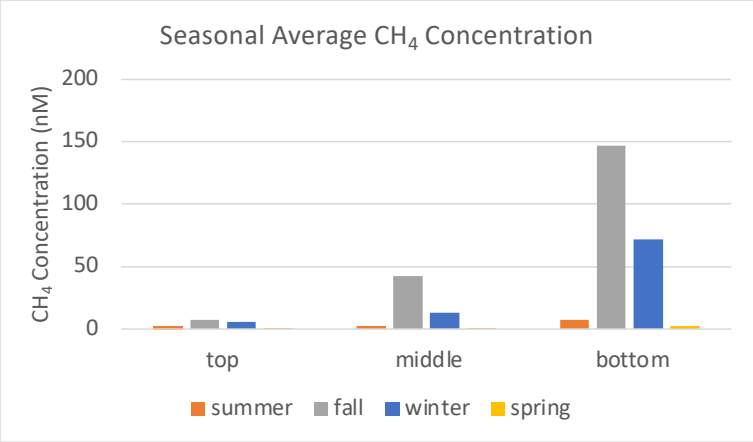

Figure 4. Seasonal average CH_4 concentrations of the three different layers of the SBB for the four studied seasons.

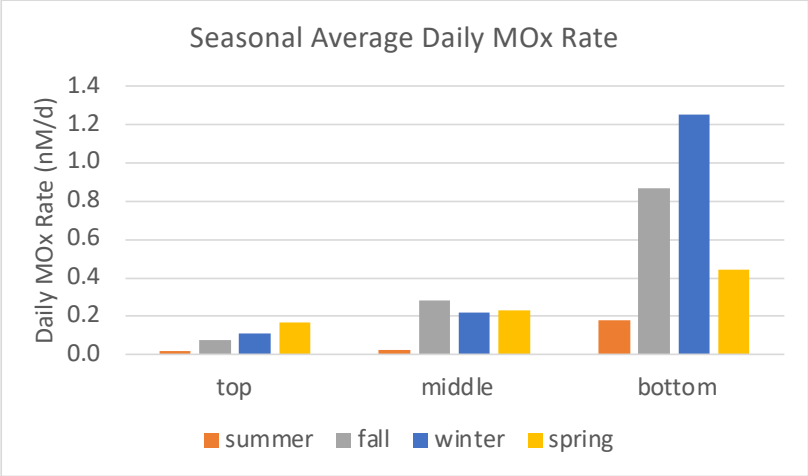

Figure 5. Seasonal average daily MOx rate of the three layers for the four studied seasons.

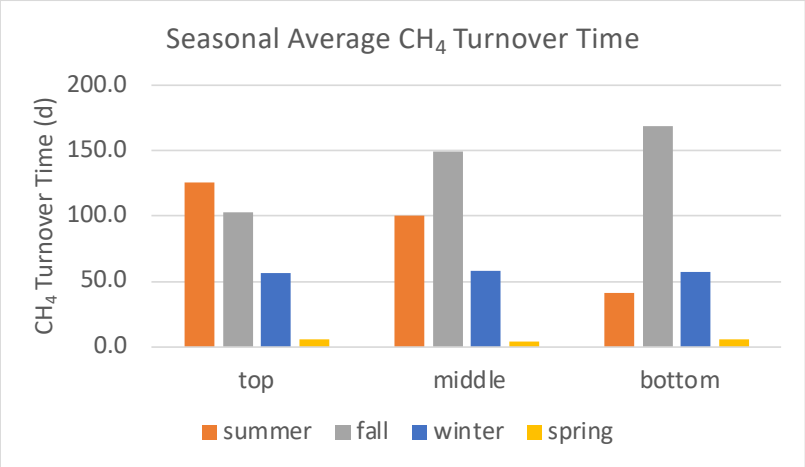

Figure 6. Seasonal average CH_4 turnover time of the three layers of the SBB deep water column during the studied time.

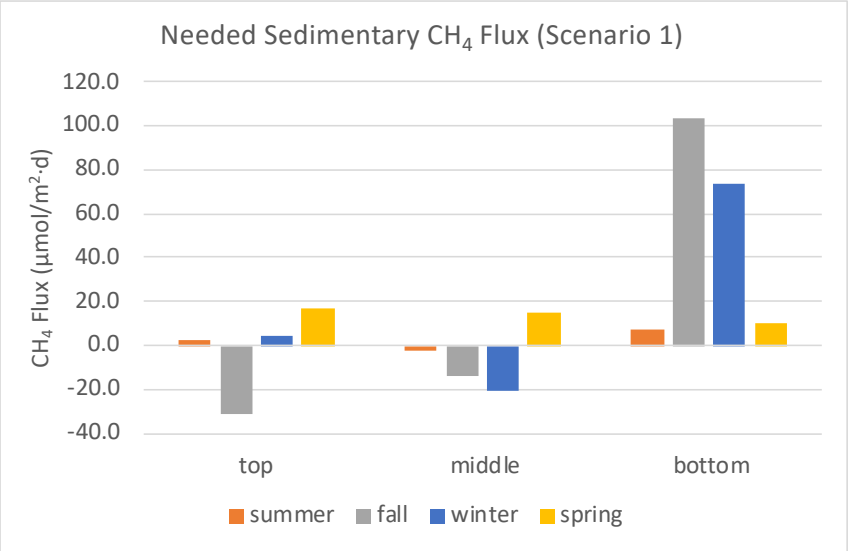

Figure 7. The needed sedimentary CH_4 flux calculated from Scenario 1.

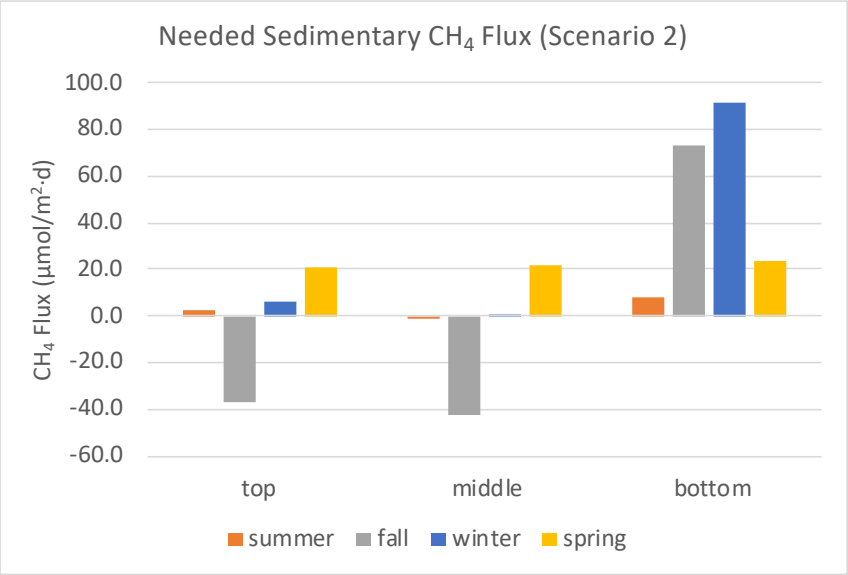

Figure 8. The needed sedimentary CH_4 flux calculated from Scenario 2.

	Top Layer (450-500m)				Middle Layer (501-550m)				Bottom Layer (551-580m)			
Season	Summer	Fall	Winter	Spring	Summer	Fall	Winter	Spring	Summer	Fall	Winter	Spring
Seasonal average methane concentration of the layer (nM)	2.41	7.76	6.21	0.91	2.28	42.71	12.87	1	7.25	146.58	71.64	2.33
Seasonal average daily MOx rate of the layer (nM/d)	0.019	0.076	0.11	0.167	0.023	0.285	0.221	0.232	0.177	0.869	1.255	0.442
Seasonal Average Methane Turnover Time (d)	126	103	56	5	100	150	58	4	41	169	57	5
Seasonal Methane Inventory of the layer (mol)	$1.02*10^5$	$3.31*10^5$	$2.62*10^5$	$1.24*10^5$	$5.31*10^4$	$1.02*10^6$	$3.08*10^5$	$7.91*10^4$	$4.56*10^4$	$9.18*10^5$	$4.51*10^5$	$4.77*10^4$
Seasonal methane Loss by MOx (mol)	$4.84*10^4$	$1.26*10^5$	$5.93*10^5$	$6.02*10^5$	$6.78*10^4$	$2.87*10^5$	$8.02*10^5$	$4.63*10^5$	$1.03*10^5$	$3.24*10^5$	$8.94*10^5$	$2.02*10^5$
Seasonal Methanotroph Community Productivity (cells)	$2.04*10^{19}$	$5.21*10^{19}$	$2.55*10^{20}$	$2.65*10^{20}$	$2.72*10^{19}$	$1.28*10^{20}$	$3.54*10^{20}$	$2.15*10^{20}$	$4.31*10^{19}$	$1.3*10^{20}$	$3.72*10^{20}$	$1.09*10^{20}$

Table 1. Values of key parameters calculated from 1m1d resolved CH_4 concentration data, 1m1d resolved MOx rate data and the 1m resolved SBB water volume data.

	Summer	Fall	Winter	Spring
mols of vertical diffused CH_4 between top and middle layer (A500*flux*day)	-6.19E+03	1.72E+06	3.28E+05	4.56E+03
mols of vertical diffused CH_4 between middle and bottom layer (A550*flux*day)	1.47E+05	3.04E+06	1.72E+06	3.91E+04

Table 2. Total amount of CH_4 (in mol) that's vertically diffused across the adjacent layers for different seasons, whether the values are positive or negative shows the direction of transport, positive values mean the transport is upward, negative values mean the transport is downward.

Layers and Season	Sink 1: CH_4 loss by MOx (mol) using 1m1d MOx rate	Sink 2: vertical diffusion from adjacent layer (mol) (positive means lose, negative means gains)	Sink 1 + Sink 2 (mol) = needed CH_4 source	Inventory difference (mol) (current-previous)	Need a methane source of (mol) considering CH_4 inventory changes	Layer corresponding intersected sediment area (m^2)	Needed sedientary flux ($\mu mol/m^2 \cdot d$) (based on sinks)	Needed sedientary flux ($\mu mol/m^2 \cdot d$) (based on sinks+inventory difference)
top summer	72,637	4,828	77,465	-21,444	98,909	3.80E+08	2.21	2.83
top fall	267,731	-1,344,377	-1,076,647	211,263	-1,287,909	3.80E+08	-30.76	-36.80
top winter	406,986	-256,203	150,783	-49,922	200,705	3.80E+08	4.31	5.74
top spring	594,920	-3,559	591,361	-139,897	731,258	3.80E+08	16.90	20.90
middle summer	45,824	-119,487	-73,663	-28,336	-45,327	3.30E+08	-2.43	-1.49
middle fall	602,437	-1,025,443	-423,006	861,385	-1,284,391	3.30E+08	-13.95	-42.36
middle winter	456,567	-1,084,779	-628,212	-643,517	15,305	3.30E+08	-20.72	0.50
middle spring	490,400	-26,973	463,428	-189,532	652,960	3.30E+08	15.28	21.53
bottom summer	97,293	114,660	211,952	-6,105	218,057	2.98E+08	7.74	7.96
bottom fall	466,244	2,369,821	2,836,064	843,246	1,992,818	2.98E+08	103.57	72.78
bottom winter	681,625	1,340,982	2,022,607	-473,695	2,496,302	2.98E+08	73.87	91.17
bottom spring	253,943	30,532	284,475	-363,447	647,921	2.98E+08	10.39	23.66

Table 3. Calculation results of two considered methane sinks – biological methane sink that's caused by methane oxidation by methanotrophs, and physical methane sink that's caused by the vertical turbulent diffusion resulting from CH_4 concentration difference between adjacent layers. And the calculation results for sink-based methane source estimations for two scenarios – scenario 1, not including CH_4 inventory changes from the previous season into account; scenario 2, taking CH_4 inventory changes from the previous season into account.

References

de Angelis M. A. and Lee C. (1994) Methane production during zooplankton grazing on marine phytoplankton. *Limnology and Oceanography* **39**, 1298–1308.

de Angelis M. A., Lilley M. D., Olson E. J. and Baross J. A. (1993) Methane oxidation in deep-sea hydrothermal plumes of the endeavour segment of the Juan de Fuca Ridge. *Deep Sea Research Part I: Oceanographic Research Papers* **40**, 1169–1186.

von Arx J. N., Kidane A. T., Philippi M., Mohr W., Lavik G., Schorn S., Kuypers M. M. M. and Milucka J. (2023) Methylphosphonate-driven methane formation and its link to primary production in the oligotrophic North Atlantic. *Nat Commun* **14**, 6529.

Broecker W., Kaufman A., Ku T.-L., Chung Y.-C. and Craig H. (1970) Radium 226 measurements from the 1969 North Pacific Geosecs Station. *Journal of Geophysical Research (1896-1977)* **75**, 7682–7685.

Capelle D. W., Hallam S. J. and Tortell P. D. (2019) Time-series CH_4 measurements from Saanich Inlet, BC, a seasonally anoxic fjord. *Marine Chemistry* **215**, 103664.

Cheng C., He Q., Zhang J., Chen B. and Pavlostathis S. G. (2022) Is the role of aerobic methanotrophs underestimated in methane oxidation under hypoxic conditions? *Science of The Total Environment* **833**, 155244.

Cheng C., Zhang J., He Q., Wu H., Chen Y., Xie H. and Pavlostathis S. G. (2021) Exploring simultaneous nitrous oxide and methane sink in wetland sediments under anoxic conditions. *Water Research* **194**, 116958.

Chung Y. (1973) Excess radon in the Santa Barbara basin. *Earth and Planetary Science Letters* **17**, 319–323.

Cicerone R. J. and Oremland R. S. (1988) Biogeochemical aspects of atmospheric methane. *Global Biogeochemical Cycles* **2**, 299–327.

Dedysh S. N., Knief C. and Dunfield P. F. (2005) Methylocella Species Are Facultatively Methanotrophic. *Journal of Bacteriology* **187**, 4665–4670.

Denman K. L. and Gargett A. E. (1983) Time and space scales of vertical mixing and advection of phytoplankton in the upper ocean. *Limnology and Oceanography* **28**, 801–815.

Ducklow H. W. and Carlson C. A. (1992) Oceanic Bacterial Production. In *Advances in Microbial Ecology* (ed. K. C. Marshall). Advances in Microbial Ecology. Springer US, Boston, MA. pp. 113–181.

Eichhubl P., Greene H. G. and Maher N. (2002) Physiography of an active transpressive margin basin: high-resolution bathymetry of the Santa Barbara basin, Southern California continental borderland. *Marine Geology* **184**, 95–120.

Fanning K. A. and Pilson M. E. Q. (1972) A model for the anoxic zone of the Cariaco Trench. *Deep Sea Research and Oceanographic Abstracts* **19**, 847–863.

Ferry J. G. and Lessner D. J. (2008) Methanogenesis in Marine Sediments. *Annals of the New York Academy of Sciences* **1125**, 147–157.

Giovannoni S., Chan F., Davis E., Deutsch C. and Wolf S. (2021) *Biochemical Barriers on the Path to Ocean Anoxia?*, Microbiology.

Grossart H.-P., Frindte K., Dziallas C., Eckert W. and Tang K. W. (2011) Microbial methane production in oxygenated water column of an oligotrophic lake. *Proceedings of the National Academy of Sciences* **108**, 19657–19661.

Heintz M. B., Mau S. and Valentine D. L. (2012) Physical control on methanotrophic potential in waters of the Santa Monica Basin, Southern California. *Limnology and Oceanography* **57**, 420–432.

Karl D. M., Beversdorf L., Björkman K. M., Church M. J., Martinez A. and Delong E. F. (2008) Aerobic production of methane in the sea. *Nature Geoscience* **1**, 473–478.

Kendall, M. M., & Boone, D. R. (2006). The order methanosarcinales. The prokaryotes, 3, 244-256.

Knowles R. (1993) Methane: Processes of Production and Consumption. In *Agricultural Ecosystem Effects on Trace Gases and Global Climate Change* John Wiley & Sons, Ltd. pp. 145–156.

Leak D. J. and Dalton H. (1986) Growth yields of methanotrophs 1. Effect of copper on the energetics of methane oxidation. *Appl Microbiol Biotechnol* **23**, 470–476.

Lilley M. D., Baross J. A. and Gordon L. I. (1982) Dissolved hydrogen and methane in Saanich Inlet, British Columbia. *Deep Sea Research Part A. Oceanographic Research Papers* **29**, 1471–1484.

Oremland R. S. (1979) Methanogenic activity in plankton samples and fish intestines A mechanism for in situ methanogenesis in oceanic surface waters. *Limnology and Oceanography* **24**, 1136–1141.

Qin Q., Kinnaman F. S., Gosselin K. M., Liu N., Treude T. and Valentine D. L. (2022) Seasonality of water column methane oxidation and deoxygenation in a dynamic marine environment. *Geochimica et Cosmochimica Acta* **336**, 219–230.

Reeburgh W. S. (1976) Methane consumption in Cariaco Trench waters and sediments. *Earth and Planetary Science Letters* **28**, 337–344.

Reeburgh W. S. (2007) Oceanic Methane Biogeochemistry. *Chem. Rev.* **107**, 486–513.

Reeburgh W. S., Ward B. B., Whalen S. C., Sandbeck K. A., Kilpatrick K. A. and Kerkhof L. J. (1991) Black Sea methane geochemistry. *Deep-Sea Research, Part A* **38**, S1189–S1210.

Scranton M. I. (1988) Temporal variations in the methane content of the Cariaco Trench. *Deep Sea Research Part A. Oceanographic Research Papers* **35**, 1511–1523.

Simon M. and Azam F. (1989) Protein content and protein synthesis rates of planktonic marine bacteria. *Mar. Ecol. Prog. Ser.* **51**, 201–213.

Steinle L., Maltby J., Treude T., Kock A., Bange H. W., Engbersen N., Zopfi J., Lehmann M. F. and Niemann H. (2017) Effects of low oxygen concentrations on aerobic methane oxidation in seasonally hypoxic coastal waters. *Biogeosciences* **14**, 1631–1645.

Tang K. W., McGinnis D. F., Ionescu D. and Grossart H.-P. (2016) Methane Production in Oxic Lake Waters Potentially Increases Aquatic Methane Flux to Air. *Environ. Sci. Technol. Lett.* **3**, 227–233.

Trimmer M., Shelley F. C., Purdy K. J., Maanoja S. T., Chronopoulou P.-M. and Grey J. (2015) Riverbed methanotrophy sustained by high carbon conversion efficiency. *ISME J* **9**, 2304–2314.

Valentine D. L., Blanton D. C., Reeburgh W. S. and Kastner M. (2001) Water column methane oxidation adjacent to an area of active hydrate dissociation, Eel River Basin. *Geochimica et Cosmochimica Acta* **65**, 2633–2640.

Valentine D. L., Mezic I., Macesic S., Crnjaric-Zic N., Ivic S., Hogan P. J., Fonoberov V. A. and Loire S. (2012) Dynamic autoinoculation and the microbial ecology of a deep water hydrocarbon irruption. *Proceedings of the National Academy of Sciences* **109**, 20286–20291.

Ward B. B. and Kilpatrick K. A. (1993) Methane oxidation associated with mid-depth methane maxima in the Southern California Bight. *Continental Shelf Research* **13**, 1111–1122.

Ward B. B., Kilpatrick K. A., Novelli P. C. and Scranton M. I. (1987) Methane oxidation and methane fluxes in the ocean surface layer and deep anoxic waters. *Letters to Nature* **327**, 226–229.

Ward B. B., Kilpatrick K. A., Wopat A. E., Minnich E. C. and Lidstrom M. E. (1989) Methane oxidation in Saanich inlet during summer stratification. *Continental Shelf Research* **9**, 65–75.

Wear E. K., Carlson C. A., James A. K., Brzezinski M. A., Windecker L. A. and Nelson C. E. (2015) Synchronous shifts in dissolved organic carbon bioavailability and bacterial community responses over the course of an upwelling-driven phytoplankton bloom. *Limnology and Oceanography* **60**, 657–677.

Wunsch C. and Ferrari R. (2004) Vertical Mixing, Energy, and the General Circulation of the Oceans. *Annual Review of Fluid Mechanics* **36**, 281–314.

Chapter 3 - Stable Carbon Isotope Signatures of Methane and Carbon Dioxide Produced by Methylotrophic Methanogenesis

Abstract

The biological disproportionation of methylated compounds, such as methanol, methylated amines and methylated sulfides, is performed by anaerobic archaea, yielding methane and carbon dioxide as catabolic end products. Stable carbon isotope fractionation associated with this process of methylotrophic methanogenesis has been measured for methane production, but the underlying dynamics have not been explored and the branch point fractionation leading to methane and carbon dioxide is unexplored. Here we examine the fractionation factors during methylotrophic methanogenesis with type strain methanogens capable of growth on methanol or trimethylamine solely, and a mutant methanogen capable of growth on methanol reduction coupled to H_2 oxidation or acetate oxidation. From these studies we find evidence that the large fractionations observed from methylotrophic methanogenesis derive from the initial methyl transferase step, not from the terminal reaction, and are further modulated by the metabolic branch point at which carbon dioxide becomes more ^{13}C enriched and methane becomes more ^{13}C depleted.

1. Introduction

1.1 Methylotrophic methanogenesis pathway

Methane is a potent greenhouse gas, and marine sediments are the largest global reservoir of methane. Much of the methane present in marine sediments is generated from microbial methanogenesis during organic matter degradation (Zhuang et al., 2018 a, b).

Hydrogenotrophic and acetoclastic methanogenesis pathways have long been considered the principal methane generation pathways. However, these two processes are thermodynamically inhibited by the presence of sulfate reduction. Thus, mainly occurring in the deeper reaches of marine sediments (Zhuang et al., 2018a). Unlike the major methanogenic substrates, CO_2 and acetate, the utilization of methylated substrates by methylotrophic methanogens is not subject to strong competition with sulfate-reducing bacteria (Oremland and Polcin, 1982; Kiene et al., 1986). It has been found that methylotrophic methanogens are major contributors to the limited methane production in sulfate-rich sediments, especially in the surface and shallow marine sediments. The methylotrophic methanogenesis pathway is thus also called the non-competitive or alternative methanogenesis pathway. Methanol and methylated amines are the common substrates for the methylotrophic methanogenesis pathways, along with methyl sulfides. These compounds are not utilized efficiently by the sulfate-reducing bacteria and are termed non-competitive substrates (Oremland and Polcin, 1982), although evidence clearly shows that oxidation and methylotrophic methanogenesis occur simultaneously (Krause et al., 2023). Identified methanogens capable of methylotrophic methanogenesis include members of the genera Methanococcoides, Methanosarcina, and Methanolobus (Kendall and Boone, 2006).

1.2 Methanol in the marine system

Methylated compounds are generated in marine sediments from osmolytes of marine bacteria, algae, phytoplankton, and some plants (Liu and Whitman, 2008). Methanol sources in marine systems are attributed to both in situ production and external depositions from

terrestrial origins. Terrestrial methanol mainly originates as a by-product of plant growth and to a lesser degree through fermentation of pectin (Jacob et al., 2005; Millet et al., 2008; Fischer et al., 2021). Terrestrially produced methanol evaporates into the atmosphere readily because of its volatility. A large amount of this methanol is deposited in the oceans through air-sea exchange, diffusion, and rainfall (Beale et al., 2013; Fischer et al., 2021). Methanol is also produced in situ in the oceans. Sources of this methanol are primary production by phytoplankton where methanol is an exudate by-product and through microbial fermentation of algal carbohydrates such as galactins and pectin (Sieburth and Keller, 1989; Riemer et al., 1998; Dixon et al., 2013; Fischer et al., 2021). Phytoplankton accounts for almost half of the global primary production and as such is suspected to be a major contributor to marine methanol production, the same equivalent to terrestrial primary production (Cloern et al., 2014; Mincer and Aicher, 2016; Fischer et al., 2021). However, it is unclear if and how methanol produced in surface water or exchanged with the air reaches the sediment of marine systems.

Chemolithotrophic microorganisms present in anaerobic sediments are capable of producing methanol. It has been studied that in freshwater sediments, methane oxidation by nitrate- and nitrite-dependent facultative anaerobic organisms (NC10 phylum bacteria) occur via particulate methane monooxygenase, with methanol as a key intermediate (van Grinsven et al., 2020). These processes with methanol as intermediary are leaky, and diffused methanol can be used by surrounding methylotrophic microorganisms (Chistoserdova and Kalyuzhnaya, 2018). NC10 phylum bacteria and transcripts of particulate methane monooxygenase have also been found in several marine environments by metagenomic and transcriptomic studies (He et al., 2015, 2016; Padilla et al., 2016, 2019).

1.3 Trimethylamine in the marine system

Trimethylamine (TMA) could be derived from a number of potential precursors (e.g., glycine betaine, trimethylamine oxide, and choline). The precursors are largely, but not solely, formed within phytoplankton (i.e., functioning as osmolytes) and can be converted to TMA in the water column or upon deposition at the seafloor (Keller et al., 1999; Curson et al., 2017). In addition to TMA supplied directly to marine sediments by marine algae, animals and bacteria (Budd and Spencer, 1968; King, 1988), TMA may be produced as intermediates during the anaerobic degradation of quaternary amines such as choline and glycine betaine (King, 1988).

1.4 Isotopic signature of CH_4 and CO_2

Stable carbon isotope ratios ($^{13}C/^{12}C$) provide important constraints in the development of global CH_4 budgets. Their usefulness is largely a consequence of significant kinetic isotope effects (KIEs) associated with the metabolism of microorganisms that produce and consume CH_4 within natural and anthropogenic systems (Stevens and Engelkemeir, 1988; Hornibrook et al., 2000). However, different biogeochemical processes often happen simultaneously in situ and makes it difficult to distinguish the contribution of each process. And the in situ measured $\delta^{13}C\text{-}CH_4$ values are usually the average of several different processes. The study of the individual methane biogeochemical processes is useful to better constrain the relative importance of different contributing processes, to understand the cause and nature of the variability of $\delta^{13}C\text{-}CH_4$ in natural environments, and to refine the usage of stable carbon isotope ratios as a mass balance tool.

Additionally, very little has been studied for the stable carbon isotopic compositions of the non-competitive substrates and the products of the methylotrophic methanogenesis pathways (Summons et al., 1998; Penger et al., 2012; Zhuang et al., 2016, 2017), most studies focused on the two major methanogenic pathways (Krzycki et al., 1987; Alperin et al., 1992; Gelwicks et al., 1994; Valentine et al., 2004; Conrad, 2005; Galand et al., 2010). In particular, the isotopic signatures of the produced CO_2 by methylotrophic pathway have not yet been measured by any researchers to our knowledge. The produced CO_2 is a key precursor for many reactions that occur in marine sediments, such as hydrogenotrophic methanogenesis and autotrophic acetogenesis. The $\delta^{13}C$-CO_2 of methylotrophic produced CO_2 may influence the isotope signatures of the products of the processes that use CO_2 as substrates.

1.5 Branch Point and isotopic fractionations at branch point

One feature that distinguishes the methylotrophic methanogenesis pathway from other methanogenic pathways is that the methyl groups of the substrate serve both as the electron acceptor and the electron donor. In such way, methylotrophic methanogenesis process is a considered a disproportionation reaction. This means a reaction branch point exists in the methanogenesis pathway. It has been suggested that one molecule of the methylated substrate is oxidized to provide electrons for reduction of three additional molecules to methane.

It has also been suggested that the presence of a branching pathway with an unequal isotope effect means that significant fractionation can be expressed even in a closed system. The ratio of the division of the carbon flow at the branch point, together with the carbon

isotope effects of the branched pathways, will introduce different isotope signals for the products (Hayes 2001).

This research is driven by the interest in how the existence and the degree of effectiveness of this branch point can influence the stable carbon isotopic signatures of the two products – CH_4 and CO_2 of the methylotrophic methanogenesis pathway. The two scientific questions we are particularly interested in are: What the isotopic fractionations are for CH_4 and CO_2 from methylated substrates? What metabolic steps control fractionation during methylotrophic methanogenesis and what factors modulate that fractionation?

2. Material and Method

2.1 Four Methanogen Strains and Five Cultivation Settings

Four methylotrophic methanogen strains were cultivated to study the stable carbon isotopic fractionations from methylated substrates to the two metabolic products - CH_4 and CO_2.

Methanosarcina barkeri Fusaro (M. b hereafter) strain and its mutant strain Methanosarcina barkeri ⊿mtr (M. b ⊿mtr hereafter) were provided by Professor William W. Metcalf's lab at University of Illinois - Urbana Champaign. Methanosarcina acetivorans (M. a hereafter) and Methanococcoides methylutens (M. m hereafter) were purchased through German Collection of Microorganisms and Cell Cultures GmbH (DSMZ hereafter).

M. b uses methanol as carbon and energy source and produces CO_2 and CH_4 as metabolic products. M. b ⊿mtr strain is a genetically modified strain with the deletion of the mtr operon. The mtr operon encodes the N5-methyl-tetrahydrosarcinapterin (CH_3-H_4SPT): coenzyme M (CoM) methyltransferase, which catalyzes the energy-conserving methyl

transfer from CH_3-H_4SPT to CoM during growth on H_2/CO_2 or acetate. And it also catalyzes the reverse endergonic methyl transfer from CH_3-CoM yielding CH_3-H_4SPT in the methylotrophic disproportionation methanogenesis reactions. The deletion of the mtr operon means the mutant strain cannot use methanol alone because the gene controlling Mtr enzyme is knocked out. But it was tested by Welander and Metcalf, 2005 that the mutant strain was able to grow with methanol+H_2 or methanol+acetate. M. a is similar to M. b, it uses methanol as carbon and energy source. M. m uses TMA as carbon and energy source.

2.2 Phosphate-buffered media and Growth Conditions

M. b and M. b ∆mtr strains were grown at 35°C in phosphate buffered high salt (HS hereafter) broth medium. Phosphate-buffered HS medium is composed of 0.4 M NaCl, 54 mM $MgCl_2 \cdot 6H_2O$, 19 mM NH_4Cl, 13 mM KCl, 2 mM $CaCl_2 \cdot 2H_2O$, and 2 μM resazurin. 100x DSMZ 141 trace metal solution was also added into the medium, based on the volume of media made each time (e.g. 10 ml into 1 L medium). Then the medium was aliquoted under nitrogen (Airgas Ultra High Purity Grade Nitrogen, Manufacturer Part #:UHP300) into 160 mL serum bottles, capped with thick chlorobutyl rubber stoppers and then crimp sealed by aluminum caps, and autoclaved using liquid 15 min autoclaving cycle. The volume of medium needed in each 160 mL serum bottle is back calculated according to the volume of solutions needs to be added and the volume of inoculum planned to be used, see calculation below.

0.5 M pH=7 sodium phosphate buffer, which is composed of 70% 0.5 M Na_2HPO_4 and 30% 0.5 M NaH_2PO_4, was made in 160 mL serum bottles, capped, crimp sealed and

autoclaved. Later, 2.5 mL 0.5 M pH=7 sodium phosphate buffer was added to autoclaved and cooled HS medium.

Besides the phosphate buffer, 0.4 mL 100x DSMZ 141 vitamin solution, 0.4 mL $Na_2S \cdot 9H_2O$ solution were filtered through 0.22 μm MF-Millipore MCE Membrane respectively, and then added into each bottle of HS medium. Then the medium bottles are stored at room temperature in dark for up to two months. Before transfer, medium bottles were put in incubator at desired incubation temperature for 2 hours, then 125 mM (0.2 mL 100%) methanol (for M. b) or 125 mM (0.2 mL 100%) methanol and 24.4 mM (0.4 mL 2.44 M) sodium acetate solution (for M. b ∆mtr cultivated using methanol+sodium acetate), or 125mM (0.2mL 100%) methanol and 150 mL H_2:CO_2 = 80:20 gas mixture (for M. b ∆mtr cultivated using methanol+H_2) was added to each medium bottle. And 10% of inoculum from a parent bottle was transferred to a new bottle of medium.

Medium volume in each M. b bottle: 40-4(10% inoculum)-2.5(0.5 M pH=7 sodium phosphate buffer)-0.4(100x DSMZ 141 vitamin solution)-0.4(100x Na_2S solution)-0.2(100% methanol) = 32.5 mL

Medium volume in each M. b ∆mtr bottle: 40-4(10% inoculum)-2.5(0.5 M pH=7 sodium phosphate buffer)-0.4(100x DSMZ 141 vitamin solution)-0.4(100x Na_2S solution)-0.2(100% methanol)-0.4(2.44 M sodium acetate solution) = 32.1 mL

M. a and M. m strains were grown in modified, phosphate buffered DSMZ 141c media, at 35 °C and 18 °C respectively. Phosphate-buffered 141c media contains 0.31 M NaCl, 19.68 mM $MgCl_2 \cdot 6H_2O$, 4.67 mM NH_4Cl, 4.56 mM KCl, 0.95 mM $CaCl_2 \cdot 2H_2O$, 2 μM resazurin, and 0.4 mM $Na_2S \cdot 9H_2O$. 100x DSMZ 141 trace metal solution was also added into the medium, based on the volume of media made each time (e.g. 10 ml into 1 L

medium). Then the medium was aliquoted, autoclaved same as described in HS medium preparation. The volume of medium needed in each 160 mL serum bottle is back calculated according to the volume of solutions needs to be added and the volume of inoculum planned to be used, see calculation below.

After the autoclaved medium bottles completely cooled to room temperature, 2.5 mL 0.5 M pH=7 sodium phosphate buffer solution, 0.4 mL 100x DSMZ 141 vitamin solution, 0.4 mL $Na_2S \cdot 9H_2O$ solution were added into each bottle of DSMZ 141c medium. Then the medium bottles are stored at room temperature in the dark for up to two months. Before transfer, medium bottles were placed in the incubator at desired incubation temperature for 2 hours, then 125 mM (0.2 mL 100%) methanol (for M. a) or 84 mM (0.4 mL 8.4M) TMA·HCl solution (for M. m) was added into the medium bottle, and 10% of inoculum from a parent bottle was transferred to a new bottle of medium.

Medium volume in each M. a bottle: 40-4(10% inoculum)-2.5(0.5 M pH=7 sodium phosphate buffer)-0.4(Vitamin)-0.4(Na_2S)-0.2(methanol) = 32.5 mL

Medium volume in each M. m bottle: 40-4(10% inoculum)-2.5(0.5 M pH=7 sodium phosphate buffer)-0.4(Vitamin)-0.4(Na_2S)- 0.4(TMA·HCl) = 32.3 mL

All the strains were transferred and maintained in phosphate-buffered media at least 3 times before the final cultivation to minimize the carryover effect of DIC from bicarbonate-buffered media.

2.3 Cultivation Setting

A short-term cultivation approach was employed to study the isotopic fractionation of methylotrophic methanogenesis pathways. This approach was designed as the open system

analogue, in which strains were cultivated for a short time with ample substrates. An open system is defined as one in which both matter and energy are exchanged with the surroundings (Hayes, 2004). Even though our experimental setting is not exactly an open system since the serum bottles are capped and sealed. However, for the initial growth phase of the strains (early exponential stage), the substrates can be seen as unlimited, and the amounts of products are very little compared to the substrates, so the system can be treated as an open system analogue for the early exponential phase. And the resulting isotopic fractionation between substrate and products can reflect the isotopic fractionation of the methylotrophic methanogenesis in open system condition.

An experiment was also performed to approximate a closed system analogue as comparison, wherein the strains were cultivated for a long time with limited substrates. Results from this experiment are not included in this dissertation because of delays in receiving the results of some analyses. The raw data of the measured $\delta^{13}C$-CH_4, $\delta^{13}C$-CO_2 and $\delta^{13}C$-DIC of the four strains under five cultivation conditions in a long-term cultivation setting, approximating a closed system analogue, are included in the appendix of this thesis.

For the short-term cultivation, 4 strains were cultivated under 5 different conditions (M. b with methanol, M. b ΔmtrA with methanol+H_2, M. b ΔmtrA with methanol+sodium acetate, M. a with methanol, M. m with TMA·HCl). For each condition, triplicates/duplicates were conducted (Table 1).

2.4 Sample Collection

For the short-term cultivation, each bottle was sampled every day for headspace pressure, headspace CH_4 concentration ([CH_4] hereafter), stable isotope ratios of carbon in

the produced CH_4 in the headspace ($\delta^{13}C$-CH_4 hereafter), headspace CO_2 concentration ([CO_2] hereafter), stable isotope ratios of carbon in the produced CO_2 in the headspace ($\delta^{13}C$-CO_2 hereafter); and every bottle was sampled every other day for dissolved inorganic carbon concentration ([DIC] hereafter) and stable carbon isotopic signature of produced CO_2 that's dissolved in the medium ($\delta^{13}C$-DIC hereafter). Headspace pressure was measured before any headspace gas sample is taken, to calculate the amount of gas in the headspace. The detailed sampling conducted is shown in Table 2.

For the headspace pressure, a pressure gauge (Omega Engineering Inc. Model DPG1000B-100A) was connected to a sterile 25G needle to puncture through the butyl rubber stopper and measure the headspace pressure of the cultivation bottle. The pressure gauge together with the sterile needle have a dead volume of 0.5 mL. Gas loss from the headspace into volume is corrected for as we calculate the total amount of CO_2 and CH_4 produced.

2.5 Analytical

2.5.1 Headspace CH_4 Concentration and $\delta^{13}C$-CH_4

Certain volumes of headspace gas were taken by N_2 flushed syringes and 25G sterile needles for [CH_4] and $\delta^{13}C$-CH_4 measurements on each sampling day (see Table 3 for the detailed volumes of samples taken), and then injected into helium-filled 12 mL septum capped vials (Exetainers, Labco, High Wycombe, UK). Then, [CH_4] of samples were measured using Shimadzu GC-14A equipped with flame ionization detector. For GC-14A, a 100 μL sample loop and a 3.66 m, 2-mm inner-diameter, n-octane Res-Sil C packed column (Restek) with N_2 as the carrier gas (20 mL min^{-1} flow rate) were used (Kinnaman et al.,

2007). Sub-dilutions were performed for $\delta^{13}C\text{-}CH_4$ samples whose concentrations exceeded the suggested range of measurement by UC Davis. A combined dilution factor is calculated by multiplying the dilution factor from serum bottle to the 12 mL Exetainer vial and the sub-dilution factor from the 12 mL Exetainer vial to the secondary 12 mL Exetainer vial for sub-diluted samples.

Sample harvest and preparation were performed according to UC Davis stable isotope facility's requirements. $\delta^{13}C\text{-}CH_4$ analyses were conducted by UC Davis stable isotope facility. $\delta^{13}C\text{-}CH_4$ are measured using a Thermo Scientific Precon concentration unit interfaced to a Thermo Scientific Delta V Plus isotope ratio mass spectrometer (ThermoScientific, Bremen, Germany). Gas samples are purged from vials through a double-needle sampler into a helium carrier stream (20 mL/min), which is passed through a H_2O/CO_2 scrubber ($Mg(ClO_4)_2$, Ascarite) and a cold trap (90 cm piece of coiled divinylbenzene 0.32 mm GS-Q column) cooled by liquid nitrogen. The CH_4 is separated from residual gases by a GS-CarbonPLOT GC column (30 m x 0.32 mm x 3 μm, 30 °C, 1.5 mL/min). After CH_4 elutes from the separation column, methane is oxidized to CO_2 by reaction with nickel oxide at 1000 °C (^{13}C), and subsequently transferred to the IRMS. A pure reference gas (CO_2) is used to calculate provisional delta values of the sample peak. Final delta values are obtained after adjusting the provisional values for changes in linearity and instrumental drift such that correct delta values for laboratory reference materials are obtained. Laboratory reference materials are commercially prepared CH_4 gas diluted in helium or air and are calibrated against NIST 8559, 8560, and 8561. Final delta values, are expressed relative to the international standards V-PDB (Vienna PeeDee Belemnite).

2.5.2 Headspace CO_2 Concentration and $\delta^{13}C$-CO_2

Certain volumes of headspace gas were taken by N_2 flushed syringes and 25G sterile needles for [CO_2] and $\delta^{13}C$-CO_2 measurements on each sampling day (see Table 3 for the detailed volumes of samples taken), and then injected into helium-filled 12 mL septum capped vials (Exetainers, Labco, High Wycombe, UK). Then, [CO_2] of samples were measured using a Thermo Scientific GC Trace 1310 equipped with a TCD detector. For GC Trace 1310, Agilent CARBOPLOT column is used, with He as the carrier gas.

Sample harvest and preparation were performed according to UC Davis stable isotope facility's requirements. $\delta^{13}C$-CO_2 analyses were conducted by UC Davis stable isotope facility. $\delta^{13}C$-CO_2 are measured using a Thermo Scientific GasBench system interfaced to a Thermo Scientific Delta V Plus isotope ratio mass spectrometer (ThermoScientific, Bremen, Germany). CO_2 is sampled by a six-port rotary valve (Valco, Houston TX) with either a 100 µL, 50 µL, or 10 µL loop programmed to switch at the maximum CO_2 concentration in the helium carrier gas. The CO_2 is then separated from N_2O and other residual gases by a Poraplot Q GC column (25 m x 0.32 mm ID, 45 °C, 2.5 mL/min). A pure reference gas (CO_2) is used to calculate provisional delta values of the sample peak. Final ^{13}C delta values are obtained after adjusting the provisional values for changes in linearity and instrumental drift such that correct ^{13}C delta values for laboratory reference materials are obtained. At least two laboratory reference materials are analyzed with every 10 samples. Laboratory reference materials are calibrated directly against NIST 8545. Final ^{13}C delta values, are expressed relative to the international standard V-PDB (Vienna PeeDee Belemnite).

2.5.3 Dissolved Inorganic Carbon Concentration and δ^{13}C-DIC

For DIC samples, each time 0.5 mL of medium was taken from the cultivation serum bottle by N_2 flushed syringes and 25G sterile needles, then injected into helium-filled 12 mL septum capped vials (Exetainers, Labco, High Wycombe, UK) containing 1 mL 85% phosphoric acid, which forces the equilibrium between CO_2 and H_2CO_3 to gaseous CO_2. Vials were shaken 20 times to make sure DIC in the medium is fully released to the headspace as CO_2.

The evolved CO_2 from DIC is purged from vials through a double-needle sampler into a helium carrier stream (20 mL/min). The gas is sampled using a six-port rotary valve (Valco, Houston TX) with either a 100 µL, 50 µL, or 10 µL loop programmed to switch at the maximum CO_2 concentration in the helium carrier. The CO_2 is passed to the IRMS through a Poraplot Q GC column (25m x 0.32mm ID, 45 °C, 2.5 mL/min). A reference CO_2 peak is used to calculate provisional delta values of the sample CO_2 peak. Final ^{13}C delta values are obtained after adjusting the provisional delta values for changes in linearity and instrumental drift such that correct ^{13}C delta values for laboratory reference materials are obtained. At least two laboratory reference materials are analyzed with every 10 samples. Laboratory reference materials are lithium carbonate dissolved in degassed deionized water and a deep seawater (both calibrated against NIST 8545). Final ^{13}C delta values, delivered to the customer, are expressed relative to the international standard V-PDB (Vienna PeeDee Belemnite).

2.5.4 δ^{13}C-sodium acetate and δ^{13}C-TMA

Sample preparation was performed according to UC Davis stable isotope facility's requirements. δ^{13}C-acetate and δ^{13}C-TMA analyses were conducted by UC Davis stable isotope facility.

Sodium acetate trihydrate (Ensure, 6131-90-4) were taken out from storage chemical bottle, pulverized and then weighed, and packaged into tin capsules (Costech Analytical Technologies Inc. 5×9 mm). TMA·HCl (Aldrich, T72761-100G, 98%) were taken out from storage chemical bottle, weighed and packaged into tin capsules. Sodium acetate and TMA samples are analyzed for ^{13}C isotope ratios using a Micro Cube elemental analyzer (Elementar Analysensysteme GmbH, Hanau, Germany) interfaced to an Isoprime VisION IRMS (Elementar UK Ltd, Cheadle, UK). Samples are combusted at 1080°C in a reactor packed with chromium oxide and silvered copper oxide. Following combustion, oxides are removed in a reduction reactor (reduced copper at 650°C). The helium carrier then flows through a water trap (magnesium perchlorate and phosphorous pentoxide). CO_2 is released to the IRMS.

2.5.5 δ^{13}C-methanol

δ^{13}C-methanol measurement was also performed by UC Davis Stable Isotope facility. 1 mL 100% methanol (Fisher Chemical, HPLC Grade, 0.2 μm filtered, UN1230) sample was taken using a N_2 flushed syringe with 25G sterile needle directly from chemical storage bottle and transferred into 2 mL septum capped amber GC vial.

Compound-specific ^{13}C isotope analysis was performed to measure the δ^{13}C of methanol**,** using GC-combustion isotope ratio mass spectrometry (GC-C-IRMS). Methanol is entirely combusted to CO_2, and subsequently introduced into the isotope-ratio mass

spectrometer. Analysis is performed using Thermo GC-C-IRMS systems composed of a Trace GC 1310 gas chromatographs (Thermo Electron Corp., Milan, Italy) coupled to a Thermo Finnigan MAT 253 isotope-ratio mass spectrometer via a GC IsoLink II combustion interface (Thermo Electron Corp., Bremen, Germany). Compound identification support for the CSIA laboratory is been provided by a Thermo ISQ single-quadrupole MS (Thermo Electron Corp., Bremen, Germany).

3. Results and Discussions

3.1 Isotope Systematics and Calculation of Fractionation Factors

All carbon isotope values are given in the per mil notation (‰) relative to the V-PDB standard (Pee Dee belemnite carbonate, as established by the International Atomic Energy Agency in Vienna, Austria (Gonfiantini et al., 1995)).

Fractionation factors reported in this study are expressed using either the α or ε notation. In the case where isotopic equilibrium is achieved, α is defined as:

$$\alpha = R_b/R_a \quad \text{(Eq. 1)}$$

where R_b and R_a are the isotope ratios of products and reactants, respectively. In cases where fractionations are small (less than 10‰; (O'Neil, 1986) the fractionation factor, ε, can be used:

$$\varepsilon = (\alpha - 1) \times 1000\ (‰) \quad \text{(Eq. 2)}$$

An isotopically open system is one in which both matter and energy are exchanged with the surroundings (Hayes, 2004), or to say, reactants are constantly added, and products are constantly withdrawn (Valentine et al., 2004). During the early stages of our growth experiments, the conditions can be treated as open systems. The ample supply of reactants

resembles the constantly added reactants, and the small amount of products produced would dilute into the cultivation container quickly, resemble the constantly withdrawn products.

For an open system model, the isotopic fractionation factors between the product and reactant can be calculated following the definition equation of isotopic fractionation factor α (Eq. 1), and the definition of the delta notation (Eq. 3):

$$\delta^{A}X_{STD} = \left(\frac{{}^{A}R_{sample}}{{}^{A}R_{STD}} - 1\right) \times 1000 \quad (‰) \qquad \text{(Eq. 3)}$$

where δ expresses the abundance of isotope A of element X in a sample relative to the abundance of that same isotope in an arbitrarily designated reference material, or isotopic standard. In our study, V-PDB standard for the stable carbon isotope.

By plugging Eq. 3 into Eq. 1, we can get an equation for the isotopic fractionation factor α by the delta notation of the product and reactant (Eq. 4):

$$\alpha = \frac{\delta_b + 1000}{\delta_a + 1000} \qquad \text{(Eq. 4)}$$

where δ_b denotes the $\delta^{13}C$ values of the products, and δ_a denotes the $\delta^{13}C$ values of the reactants.

For the cultivation conditions of M. b, M. a and M. m strains, there's one type of carbon in the studied methylotrophic methanogenesis substrates (methanol or TMA), and that carbon supplies the production of both CO_2 and CH_4. So, an isotopic fractionation factor can be calculated from the isotopic signatures of the produced CO_2 and the substrate (α based on $\delta^{13}C$-(CO_2+DIC) hereafter), while another isotopic fractionation factor can be calculated from the isotopic signatures of the produced CH_4 and the substrate (α based on $\delta^{13}C$-CH_4 hereafter). For M. b ΔmtrH with H_2, the only product is CH_4, no CO_2 is produced. So, we can only calculate α based on $\delta^{13}C$-CH_4. For M. b ΔmtrH with sodium acetate, α based on $\delta^{13}C$-CH_4 is calculated by the stable carbon isotopic signatures between the produced CH_4 and the

corresponding substrate methanol, while α based on $\delta^{13}C$-(CO_2+DIC) is calculated by the stable carbon isotopic signatures between the produced CO_2+DIC and the corresponding substrate sodium acetate (assuming both positions of acetate have the same $\delta^{13}C$).

3.2 Methylotrophic Methanogenesis Pathways of the Four Strains Under Five Cultivation Settings

Figure 1 shows the different methylotrophic methanogenesis metabolic pathways of the four methanogen strains under the five cultivation conditions.

For the M. b strain (Fig. 1A), CH_3OH is take up by the cell, and the methyl group transferred to CoM by methanol:coenzyme M methyltransferase MtrABC (Fricke et al., 2006; Borrel et al., 2013; Bennett et al., 2018). CH_3-CoM is then split into two routes at the reaction branch point, one route leads to the oxidation of CH_3-CoM to CO_2. This route starts with turning CH_3-CoM to CH_3-H_4SPT, and then step by step into CH_2=H_4SPT, CH≡H_4SPT, CHO-H_4SPT, CHO-MF, and finally to CO_2. The other route leads to the reduction of CH_3-CoM to CH_4. It has been suggested that the oxidation of one moiety of CH_3-CoM can provide the electrons needed for the reduction of three moieties of CH_3-CoM to CH_4. Following this reaction stoichiometry and the measured isotopic signatures of the produced CO_2 and CH_4, we are able to calculate the isotopic fractionation factors of the two routes at the reaction branch point. Need to note, the stable carbon isotopic signatures of the produced CH_4 potentially reflect the combined effects of 2 steps, from CH_3OH to CH_3-CoM, and then from CH_3-CoM to CH_4. The stable carbon isotopic signatures of the produced CO_2 potentially reflect the combined effects of 7 steps, from CH_3OH to CH_3-CoM, then to CH_3-H_4SPT, then to CH_2=H_4SPT, CH≡H_4SPT, CHO-H_4SPT, CHO-MF, and finally to CO_2.

For the M. b ΔmtrA strain, since the mtr operon is deleted, the expression of the Mtr enzyme is blocked, so CH_3-CoM cannot be turned to CH_3-H_4SPT and further oxidized to CO_2. The oxidation branch of the disproportionation reaction is blocked. It has been tested by Welander and Metcalf, 2005 that, the mutant strain can still utilize a small amount of CH_3OH, but only for a short period of time, which is not able to support the growth of the strain. The utilization without the Mtr enzyme suggested that a bypass of the energy consuming Mtr step exists, however, why this bypass cannot support the growth of the cells are not clear. It has also been tested whether other sources of reducing power can be used to support the reduction from CH_3OH to CH_4. And it was shown that reducing power provided by either the oxidation of H_2, or the oxidation of sodium acetate, can be coupled to the reduction of CH_3-CoM to CH_4 and thus enable growth of the mutant strain.

The methanogenesis pathway of CH_3OH reduction coupled to H_2 oxidation of the M. b ΔmtrA strain is shown in Fig. 1B. One moiety of H_2 is oxidized to 2 protons, providing the reducing power to convert one moiety of CH_3OH to CH_4.

The methanogenesis pathway of CH_3OH reduction coupled to sodium acetate oxidation of the M. b ΔmtrA strain is not fully understood yet. However, it has been tested by Welander and Metcalf, 2005 that all the produced CO_2 comes from sodium acetate, and all the CH_4 comes from CH_3OH. When the carbonyl group of acetate was labeled, 62% of the CO_2 produced was labeled, whereas 36% of the CO_2 produced was labeled when the label was on the methyl group of acetate. It has been expected that the oxidation of one moiety CH_3COOH to CO_2 can support the reduction of four moieties of CH_3OH to CH_4, but was shown that in reality, the ratio is lower than expected, because about a quarter of the CH_3COOH was oxidized to formate, not able to provide enough reducing power for the

reduction of four moieties of CH_3OH to CH_4. Our proposed metabolic pathway is shown in Fig. 1C.

The methylotrophic methanogenesis pathway for the M. a strain is the same with the M. b strain, shown in Fig. 1A.

Lastly, for the M. m strain, the methylotrophic methanogenesis pathway is also the same to M. b strain and M. a strain, the only difference being that the substrate was fed TMA, instead of CH_3OH.

Need to note, in all cases here, fractionation factors represent net fractionation associated with a series of physical and chemical steps; however, fractionation factors are presented as if they were associated with a single step. Fractionation factors associated with specific and individual reactions remain constant; such fractionation factors reflect isotope discrimination due to kinetic and/or thermodynamic isotope effects. Fractionation factors associated with multistep reactions are variable and may be expressed at different levels. See Hayes (1983, 2001) for a detailed consideration of these issues.

3.3 Stable Carbon Isotopic Fractionation Factors Calculated Using Open System Model

Each day's CO_2 amount, CH_4 amount in the serum bottle is corrected by adding the loss because of headspace pressure measurement and sampling. We used a fixed volume of 0.5 mL for each headspace pressure measurement. For headspace sampling, the volume depends on each sampling day's arrangement. The volume is converted into total gas amount using the ideal gas law equation, $PV=nRT$, where P denotes the pressure of gas in the headspace, R is the ideal gas law constant, T is the temperature of cultivation in Kelvin, V

denotes the volume of gas in the headspace. The resulting moles of gases in the headspace is then multiplied by either the [CO_2] or [CH_4] measured in the headspace on the sampling day.

Each sampling day's DIC concentration was first corrected by adding the DIC that's lost as samples back, and this was simply done by multiplying the 0.5 mL sample volume by the DIC concentration measured for the sampling day. And then a second correction is performed for each sampling day by subtracting the DIC amount of day 0, to avoid any initial CO_2 that's dissolved in the medium, and to avoid the carry over effect caused by the inoculation from parent bottles. Then CO_2 and DIC amounts of the same sampling day of the same strain are combined to represent the total amount of CO_2 produced by the strains.

δ^{13}C-DIC of each sampling day is also corrected for the δ^{13}C-DIC of day 0 and the DIC amount of day 0 following the correction equation Eq. 7. δ^{13}C-(CO_2+DIC) is calculated following Eq. 8.

Correction of experimental results for the effects of blanks (for DIC) are conducted according to the mass-balance calculation equations as below (Hayes, 2004).

$$\delta_{\Sigma} = \frac{\Sigma m_i \delta_i}{\Sigma m_i} \quad \text{(Eq. 5)}$$

The above equation can be further simplified. When a sample has been contaminated during its preparation by contributions from an analytical blank, the isotopic abundance actually determined during the mass spectrometric measurement is that of the sample plus the blank. Using Σ to represent the sample prepared for mass spectroscopic analysis and x and b to represent the sample and blank, we can write:

$$m_{\Sigma}\delta_{\Sigma} = m_x\delta_x + m_b\delta_b \quad \text{(Eq. 6)}$$

In our experiment, the $(\delta^{13}C - DIC)_{t\ corrected}$ can be calculated following the equation below:

$$(\delta^{13}C - DIC)_{t\ corrected} = \frac{(\delta^{13}C-DIC)_t \times (m_{DIC})_t - (\delta^{13}C-DIC)_0 \times (m_{DIC})_0}{(m_{DIC})_t - (m_{DIC})_0} \quad \text{(Eq. 7)}$$

where $(\delta^{13}C - DIC)_t$ means the $\delta^{13}C$ of DIC at any sampling day, $(\delta^{13}C - DIC)_0$ means the $\delta^{13}C$ of DIC at day 0, $(m_{DIC})_t$ denotes the measured DIC amount of any sampling day, $(m_{DIC})_0$ denotes the DIC amount of day 0. $(\delta^{13}C - DIC)_{t\ corrected}$ indicates the corrected $\delta^{13}C$ of DIC of any sampling day.

$$(\delta^{13}C - (CO_2 + DIC))_t = \frac{(\delta^{13}C-CO_2)_t \times (m_{CO_2})_t + (\delta^{13}C-DIC)_{t\ corrected} \times (m_{DIC})_{t\ corrected}}{((m_{CO_2})_t + (m_{DIC})_{t\ corrected})} \quad \text{(Eq. 8)}$$

$(\delta^{13}C - (CO_2 + DIC))_t$ means the $\delta^{13}C$ of the total produced CO_2 of any sampling day. $(m_{CO_2})_t$ means the headspace CO_2 amount of the sampling day, and $(\delta^{13}C - CO_2)_t$ denotes the $\delta^{13}C$ of the headspace CO_2 in the cultivation bottles; $(m_{DIC})_{t\ corrected}$ means the corrected DIC concentration of the sampling day, and $(\delta^{13}C - DIC)_{t\ corrected}$ denotes the corrected $\delta^{13}C$ of DIC of the sampling day.

Stable carbon isotopic fractionation factors are calculated for both routes of the disproportionation of methylotrophic methanogenesis. The fractionation factor between the produced CH_4 and corresponding substrate is calculated using the $\delta^{13}C$-CH_4 of each sampling day, and the initial $\delta^{13}C$ of the substrate (CH_3OH for M. b, M. b ΔmtrA with H_2, M. b ΔmtrA with sodium acetate, M. a; TMA for M. m), following Eq. 4. The fractionation factor between the total produced CO_2 and corresponding substrate is calculated using the $\delta^{13}C$-(CO_2+DIC) of each sampling day, and the initial $\delta^{13}C$ of the substrate (CH_3OH for M. b, M. a; sodium acetate for M. b ΔmtrA with sodium acetate; TMA for M. m), also following Eq. 4.

The $\delta^{13}C$ of the reactants were measured as pure chemicals, using either GC-C-IRMS (for methanol) or EA-IRMS (for sodium acetate and TMA) analytical methods. The measurement results are listed in Table 4.

α values are calculated based on Eq. 4, for the same strain, the denominator of the equation $\delta_a + 1000$ would be a constant value, because the substrate used for CH_4, or CO_2 production would be the same for the same strain. So, the α values are strongly dependent on the numerator, $\delta_b + 1000$. Ideally, the most negative δ_b values are supposed to appear on day 1, when the kinetic isotope effect is the most obvious, where the methanogens tend to use the lightest carbons first. However, even though the parent bottle was flushed with N_2 gas before inoculation, we still saw carry-over effect in some of the cultivations. So, the most negative values don't always appear in day 1. As a result, we picked the most negative values from day 1 to day 4 as representative α values for the open system calculation results. The same is true for the calculation and selection of ε values.

Need to notice, the ε values for M. a strains are probably too enriched. This is because DIC and CO_2 samples were both collected only on day 2 and day 4, but the M. a strains grew very fast, and the most ideal condition of the open system isotopic resemblance was likely already missed on day 2.

For strains utilizing the same substrate, a more negative value indicates that the product has more depleted $\delta^{13}C$ values. The M. b strains and M. a strains had very similar average $\delta^{13}C$-CH_4 based ε values (-85.31‰ and -85.05‰), and we attribute this to the fact that both strains use methanol as substrates for CH_4 production, and experienced similar metabolic processes. However, the $\delta^{13}C$-(CO_2+DIC) based ε values for the two strains are very different, -43.57‰ for M. b strains while -15.91‰ for M. a strains. Again, the (CO_2+DIC) based ε values for M. a strains are probably too enriched. Because DIC and CO_2 samples were both collected only on day 2 and day 4, but the M. a strains grew very fast, and

the most ideal condition of the open system isotopic resemblance was likely already missed on day 2.

It's obvious that for strains utilizing different substrates for methylotrophic methanogenesis, the resulting $\delta^{13}C$-CH_4 based ε values and $\delta^{13}C$-(CO_2+DIC) based ε values can be different according to our cultivation experiments. M. m strains that use TMA as substrates have much more enriched $\delta^{13}C$-CH_4 based ε values and $\delta^{13}C$-(CO_2+DIC) based ε values compared to the strains using methanol as substrates (M. b strains and M. a strains), even though the current studied metabolic pathways of methylotrophic methanogenesis for the two substrates are very similar.

For the M. b strains and M. b ∆mtr strains, the resulting $\delta^{13}C$-CH_4 based ε values and $\delta^{13}C$-(CO_2+DIC) based ε values are also different. The wild type strains produced more depleted CH_4 compared to the mutant strains. The comparison between the M. b strain and the M. b ∆mtr growing using CH_3OH+H_2 is the most representative to show the difference at the branch point. The M. b strain had a ε of -85.31‰ from CH_3OH to CH_4, and a ε of -43.57‰ from CH_3OH to CO_2. While the ε(CH_4) value we got from the M. b ∆mtr strain is -79.53‰, 5.78‰ greater than the wild strain. This comparison indicates that the branch point introduces more isotopic fractionations to the resulting products and causes products to be more depleted in isotopic values.

For the M. b ∆mtr strain that grew under CH_3OH+H_2 condition and M. b ∆mtr strain that grew under CH_3OH+sodium acetate condition, the $\delta^{13}C$-CH_4 based ε values measured were similar (-79.53‰ for strains with CH_3OH+H_2, and -77.87‰ for strains with CH_3OH + sodium acetate) indicating that the isotopic fractionation from CH_3OH to CH_4 remains

relatively stable, whether the reduction of CH_3OH to CH_4 is coupled to H_2 oxidation or acetate oxidation.

3.4 Open System Steady State Calculations to Estimate $\delta^{13}C$-(CH_3-CoM), ε(CH_3-CoM to CH_4), and ε(CH_3-CoM to CO_2) of Strains Utilizing Methanol as Substrate

A further delve into the comparison between M. b strain and M. b ∆mtr strain that grew with CH_3OH+H_2 gives us a better understanding of the isotope systematics at the reaction branch point. A first important consideration is the reversibility of metabolism for carbon entering the methanogenic pathway through methanol to CH_3-CoM. The Gibbs Free Energy yield for this reaction step has been calculated at -27 kJ/mol, making the reaction highly exergonic in vivo (Deppenmeier et al., 1989). While the reaction has been shown to be reversible (Timmers et al., 2017), the exergonic character of the reaction indicates that the extent of equilibration in vivo will be limited, and isotopic equilibration is therefore unlikely during active metabolism. To test this assumption, we compared the isotope fractionation from methanol to CH_4 for M. b strain and M. b ∆mtr. If isotopic equilibration was achieved between CH_3OH and CH_3-CoM, we would predict that the produced methane would have the same $\delta^{13}C$ for both cases, which it does not. In contrast, if isotopic equilibrium was not achieved between CH_3OH and CH_3-CoM, we would predict additional fractionation arising from different epsilon factors at the branch point, and indeed a 5.8‰ shift is observed. Together the thermodynamic and isotopic evidence point to the initial step of methyl transfer as the primary source of fractionation in the system and as a reaction with minimal isotopic equilibration for these experimental conditions.

In order to explore our inference, we employ the open system steady state model described in Hayes, 2004 (Fig. 2). Here we treat the initial exponential phase of growth in the cultivation bottles as open system at steady state, in which reactant flows steadily into a reaction chamber and products flow from the chamber. The amount of material in the reaction chamber is constant.

For M. b strain, the flux of carbon entering the box f_i equals the flux of products out of the chamber f_1+f_2. δ_i denotes the $\delta^{13}C$ of carbon entering the system, while δ_1 and δ_2 show the $\delta^{13}C$ of two carbon related products leaving the system. According to isotope mass balance equation (Eq. 6),

$$f_i\delta_i = f_1\delta_1 + f_2\delta_2 \quad \text{(Eq. 9)}$$

Since we already know the reaction stoichiometry of the methylotrophic reaction from methanol to CH_4 and CO_2, $f_1=0.75f_i$, $f_2=0.25f_i$. And then according to our short-term cultivation experiment, δ_2 has an average value of -68.9‰, and δ_1 has an average value of -110.3‰, so δ_i can be calculated as 0.75*(-110.3‰) + 0.25*(-68.9‰) = -99.95‰.

Because of the definition of $\delta_i = \delta^{13}C\text{-}CH_3OH + \varepsilon_i$, ε_i = -72.65‰, this value shows the isotopic fractionation of the methyl transferase step, from the provided substrate CH_3OH to the intermediate CH_3-CoM, based on our assumptions.

δ_{ss} denotes the $\delta^{13}C$-(CH_3-CoM) at steady state. At steady state, $\delta_1 = \delta_{ss} + \varepsilon_1$ (δ_{ss} = -110.3‰ - ε_1), and $\delta_2 = \delta_{ss} + \varepsilon_2$ (δ_{ss} = -68.9 - ε_2), so

$$\varepsilon_1-\varepsilon_2 = \delta_1-\delta_2 \quad \text{(Eq. 10)}$$

In order to estimate the δ_{ss}, ε_1, and ε_2 values, we made a figure (Fig. 3) to estimate the values of ε_1 and ε_2 based on the potential δ_{ss} values at the steady state. Since the δ_i entering the box is -99.95‰, and in the box only equilibrium isotope effect takes place, the tested δ_{ss}

values range from -99.95‰ to -9.95‰. The corresponding ε_1 and ε_2 values are shown in Figure 3. A more reasonable estimated value range for δ_{ss} would be -59.95 to -39.95‰, which corresponds to a ε_2 value range of -28.9 to -8.95‰, and a ε_1 value range of -70.35 to -50.35‰.

For M. b ∆mtr strain, the flux of carbon entering the box f_i equals the flux of products out of the chamber f_1', $f_i\delta_i = f_1'\delta_1'$, so $\delta_i = \delta_1'$. According to our short-term experiment measurements, $\delta_i = \delta_1' = -104.7‰$. Again, according to the definition $\delta_i = \delta^{13}C\text{-}CH_3OH + \varepsilon_i$, $\varepsilon_i = \delta_i - \delta^{13}C\text{-}CH_3OH = -77.4‰$. We expected that for the M. b strain and the M. b ∆mtr strain, the δ_i and ε_i should have the same value, because it's the same metabolic pathway. However, the δ_i value we get from M. b ∆mtr strain is slightly more negative than the δ_i value we get from M. b strain (-99.95‰). This might be caused by the reason that we did not sample DIC for the M. b strain every day, and we may have missed the most negative values of the $\delta^{13}C\text{-}(CO_2+DIC)$. Another possible reason behind this might be related to the uptake of carbon for biomass.

At steady state, $\delta_1' = \delta_{ss}' + \varepsilon_1$. $\delta_{ss}' = \delta_1' - \varepsilon_1$, if we use the estimated range of ε_1 for M. b, then δ_{ss}' would be in the range of -54.35 to -34.35‰. This indicates that when the oxidative route from the branch point is blocked, the $\delta^{13}C$ value of the $CH_3\text{-}CoM$ responds to a more enriched value.

From these studies we find evidence that the large fractionations observed from methylotrophic methanogenesis likely derive from the initial methyl transferase step, not from the terminal reaction, and are further modulated by the metabolic branch point at which carbon dioxide becomes more ^{13}C enriched and methane becomes more ^{13}C depleted, relative to the carbon entering the metabolic pathway.

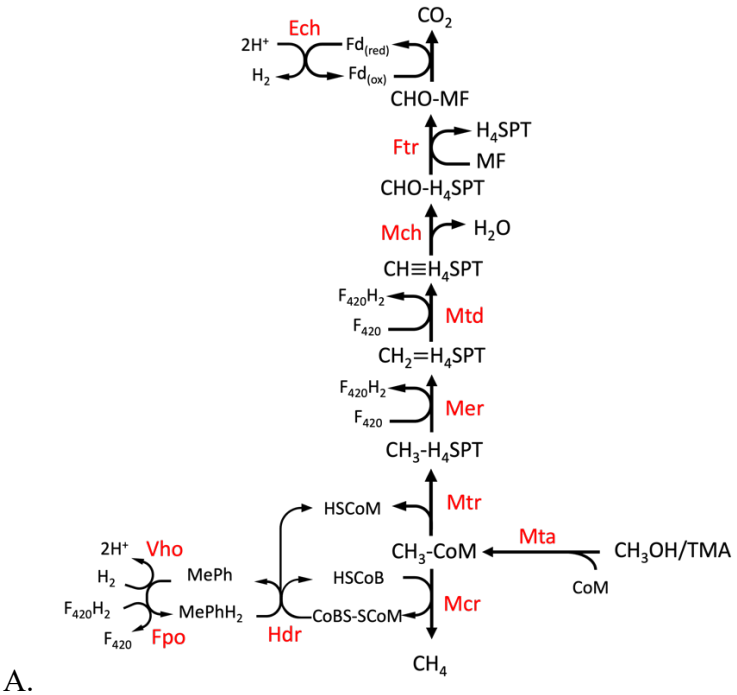

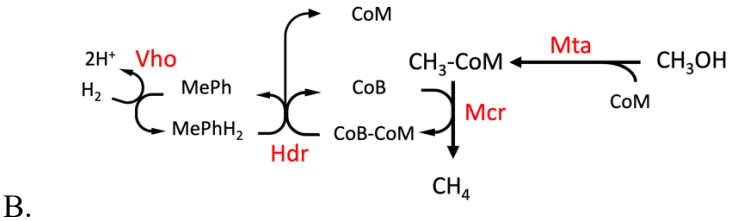

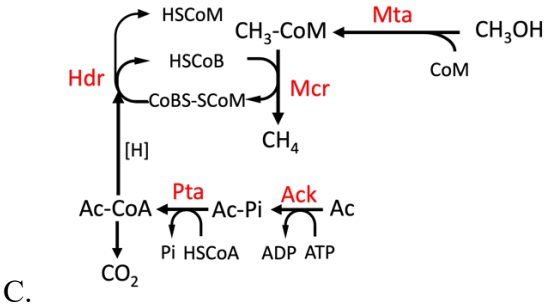

Figure 1. Three different methylotrophic methanogenesis metabolic pathways of the four methanogen strains under the five cultivation conditions. Chemicals involved are indicated in black font, while enzymes involved are highlighted in red font. A) Methylotrophic methanogenesis using methanol or TMA, used for M. b, M. a, and M. m; B) Methanol reduction coupled to H_2 oxidation, utilized by M. b ΔmtrC) Methanol reduction coupled to acetate reduction, utilized by M. b Δmtr.

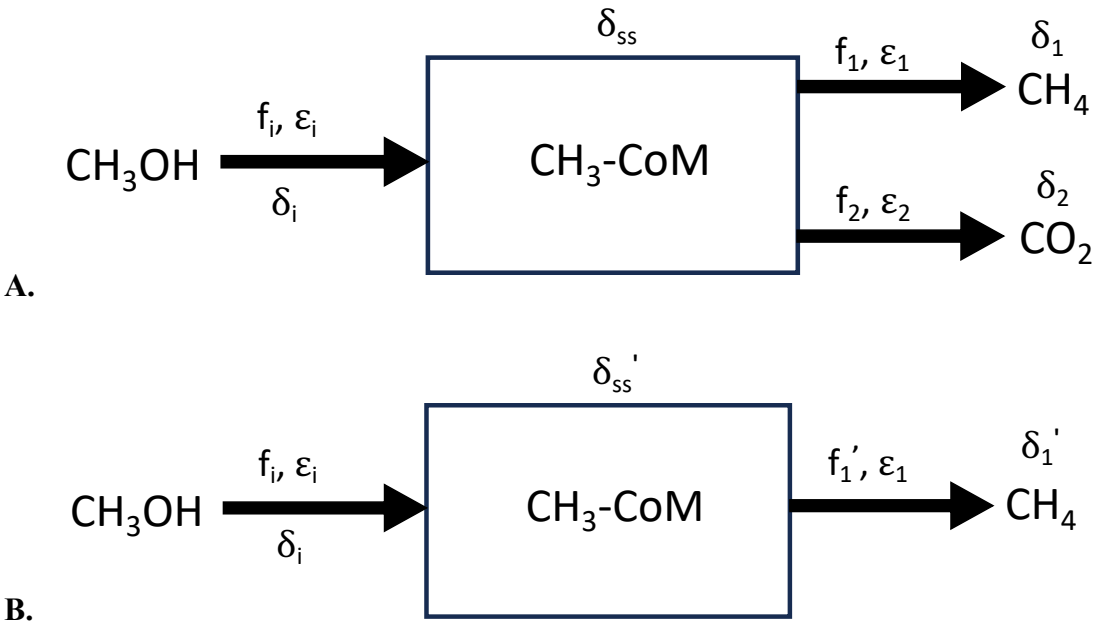

Figure 2. A) Schematic view of M. b strain cultivation as an open system at steady state. The system is supplied with reactant CH_3OH and from which products CH_4 and CO_2 are withdrawn. f_i describes the relative flux of carbon into the system, while f_1 and f_2 describe the relative flux of carbon out of the system as products CH_4 and CO_2 respectively. δ_i denotes the $\delta^{13}C$ value of carbon entering the system, and δ_1 and δ_2 show the $\delta^{13}C$ values of products CH_4 and CO_2. ε_i means the isotopic fractionation factor associated with the methyl transferase step from the provided substrate CH_3OH to CH_3-CoM. And ε_1 and ε_2 show the isotopic fractionation factors from CH_3-CoM to CH_4 ($\varepsilon(CH_3\text{-CoM to } CH_4)$) and CH_3-CoM to CO_2 ($\varepsilon(CH_3\text{-CoM to } CO_2)$) respectively. δ_{ss} depicts the $\delta^{13}C$ of CH_3-CoM at steady state condition. B) Schematic view of M. b ∆mtr strain cultivation as an open system at steady state. The system is supplied with reactant CH_3OH and from which product CH_4 is withdrawn. δ_i denotes the $\delta^{13}C$ value of carbon entering the system, and δ_1' means $\delta^{13}C$ value of product CH_4. ε_i means the isotopic fractionation factor associated with the methyl transferase step from the provided substrate CH_3OH to CH_3-CoM. And ε_1 shows the isotopic fractionation factors from CH_3-CoM to CH_4 ($\varepsilon(CH_3\text{-CoM to } CH_4)$). δ_{ss}' depicts the $\delta^{13}C$ of CH_3-CoM at steady state condition.

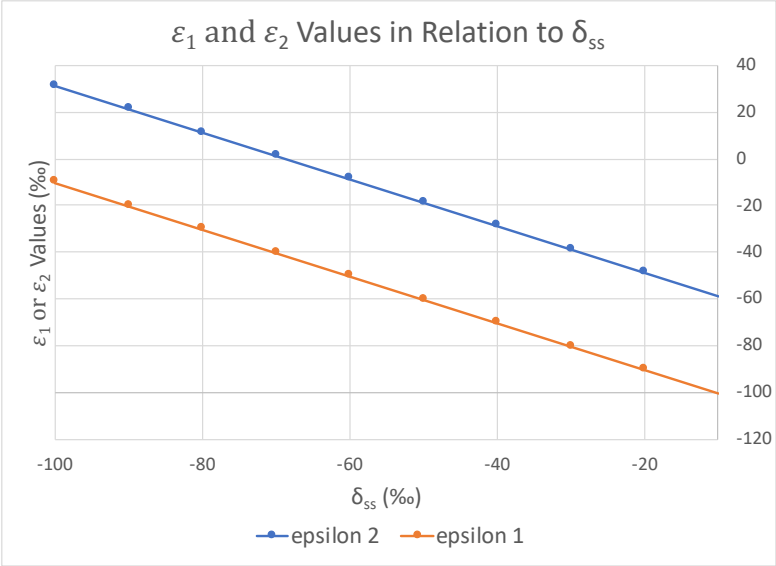

Figure 3. Estimated δ_{ss}, ε_1, and ε_2 values based on the relationship between them.

Strain name	Substrates and amounts for cultivation, short-term setting	Substrates and amounts for cultivation, long-term setting	Headspace gas for short-term setting	Headspace gas for long-term setting	Substrate utilized for CH_4 production	Substrate utilized for CO_2 production	Methylotrophic methanogenesis reaction
M. b	CH_3OH (5mmol)	CH_3OH (2.5mmol)	N_2 (120 mL)	N_2 (120 mL)	CH_3OH	CH_3OH	$4CH_3OH \rightarrow CO_2+3CH_4+2H_2O$
M. b Δmtr	CH_3OH (5mmol) + H_2 (5.08 mmol)	CH_3OH (2.5mmol) + H_2 (2.47 mmol)	H_2 (120 mL=5.08 mmol), CO_2 (30 mL=1.27 mmol)	H_2 (58.4 mL=2.47 mmol), CO_2 (14.6 mL=0.62 mmol), N_2 (120 mL)	CH_3OH	NA (no CO_2 production)	$CH_3OH+H_2 \rightarrow CH_4+H_2O$
M. b Δmtr	CH_3OH (5mmol) + CH_3COONa (0.976mmol)	CH_3OH (2.5mmol) + CH_3COONa (0.61mmol)	N_2 (120 mL)	N_2 (120 mL)	CH_3OH	CH_3COONa	$4CH_3OH+CH_3COOH \rightarrow 4CH_4+2CO_2+2H_2O$
M. a	CH_3OH (5mmol)	CH_3OH (2.5mmol)	N_2 (120 mL)	N_2 (120 mL)	CH_3OH	CH_3OH	$4CH_3OH \rightarrow CO_2+3CH_4+2H_2O$
M. m	TMA·HCl (3.36mmol)	TMA·HCl (1.68mmol)	N_2 (120 mL)	N_2 (120 mL)	TMA ·HCl	TMA ·HCl	$4NH(CH_3)_3Cl+6H_2O \rightarrow 9CH_4+3CO_2+4NH_4Cl$

Table 1. Growth conditions (substrates and headspace gas compositions) and methylotrophic methanogenesis reactions of four methanogen strains under five cultivation settings, for both the short-term and long-term cultivation settings.

	D0	D1	D2	D3	D4
M. b	d	a, b, c	a, b, c, d	a, b, c	a, b, c, d
M.b ∆mtr MeH $_2$	d	a, b, c	a, b, c, d	a, b, c	a, b, c, d
M.b ∆mtr MeAc3	d	a, b, c	a, b, c, d	a, b, c	a, b, c, d
M. a	d	a, b, c	a, b, c, d	a, b, c	a, b, c, d
M. m	d	a, b, c	a, b, c, d	a, b, c	a, b, c, d

Table 2. Short-term cultivation samplings and analyses conducted.

a, Headspace pressure

b, [CH_4] and δ^{13}C-CH_4

c, [CO_2] and δ^{13}C-CO_2

d, [DIC] and δ^{13}C-DIC

	D0					D1					D2					D3					D4				
	CH_4			CO_2		CH_4			CO_2		CH_4			CO_2		CH_4			CO_2		CH_4			CO_2	
	Volume of headspace sample (mL)	Volume of subdilution sample (mL)	Combined dilution factor	Volume of headspace sample (mL)	Dilution factor	Volume of headspace sample (mL)	Volume of subdilution sample (mL)	Combined dilution factor	Volume of headspace sample (mL)	Dilution factor	Volume of headspace sample (mL)	Volume of subdilution sample (mL)	Combined dilution factor	Volume of headspace sample (mL)	Dilution factor	Volume of headspace sample (mL)	Volume of sub-dilution sample (mL)	Combined dilution factor	Volume of headspace sample (mL)	Dilution factor	Volume of headspace sample (mL)	Volume of subdilution sample (mL)	Combined dilution factor	Volume of headspace sample (mL)	Dilution factor
Mb1	NA	NA	NA	NA	NA	1	NA	13	1	13	1	2	91	1	13	1	1	169	1	13	1	1	169	1	13
Mb2	NA	NA	NA	NA	NA	1	NA	13	1	13	1	NA	13	1	13	1	1	169	1	13	1	1	169	1	13
Mb3	NA	NA	NA	NA	NA	1	NA	13	1	13	1	1	169	1	13	1	1	169	1	13	1	1	169	1	13
Mb Δntr MeAc1	NA	NA	NA	NA	NA	1	NA	13	1	13	1	NA	13	1	13	1	1	169	1	13	1	1	169	1	13
Mb Δntr MeAc2	NA	NA	NA	NA	NA	1	NA	13	1	13	1	1	169	1	13	1	1	169	1	13	1	1	169	1	13
Mb Δntr MeAc3	NA	NA	NA	NA	NA	1	NA	13	1	13	1	1	169	1	13	1	1	169	1	13	1	1	169	1	13
Mb Δntr MeH1	NA	NA	NA	0.5	25	1		325	NA	NA	0.25	1	637	1	13	0.25	1	637	NA	NA	0.25	1	637	1	13
Mb Δntr MeH2	NA	NA	NA	0.5	25	1		325	NA	NA	0.25	1	637	1	13	0.25	1	637	NA	NA	0.25	1	637	1	13
Mb Δntr MeH3	NA	NA	NA	0.5	25	1		325	NA	NA	0.25	1	637	1	13	0.25	1	637	NA	NA	0.25	1	637	1	13
Ma1	NA	NA	NA	NA	NA	1		169	1	13	1	1	169	1	13	1	1	169	1	13	1.5	0.2	549	1.5	9
Ma2	NA	NA	NA	NA	NA	1		169	1	13	1	1	169	1	13	1	1	169	1	13	1	0.2	793	1	13
Ma3	NA	NA	NA	NA	NA	1		169	1	13	1	1	169	1	13	1	1	169	1	13	1	0.2	793	1	13
Mm1	NA	NA	NA	NA	NA	0.5	1	325	1.5	9	0.25	1	637	1.5	9	0.25	1	637	1.5	9	0.25	1	637	1.5	9
Mm2	NA	NA	NA	NA	NA	0.5	1	325	1.5	9	0.25	1	637	1.5	9	0.25	1	637	1.5	9	0.25	1	637	1.5	9
Mm3	NA	NA	NA	NA	NA	0.5	1	325	1.5	9	0.25	1	637	1.5	9	0.25	1	637	1.5	9	0.25	1	637	1.5	9

Table 3. Volumes of gas samples taken from each serum bottle to 12 mL sampling vial, and from 12 mL sampling vial to sub-dilution sampling vial (for CH_4 samples) each sampling day, and the calculated combined dilution factors.

	Measurement 1	Measurement 2	Measurement 3	Measurement 4	average
δ^{13}C-CH_3OH	-27.32‰	-27.27‰	NA	NA	-27.30‰
δ^{13}C-CH_3COONa	-41.97‰	-42.09‰	-42.01‰	-41.62‰	-41.92‰
δ^{13}C-TMA·HCl	-44.58‰	-44.54‰	-44.28‰	-44.52‰	-44.48‰

Table 4. Stable carbon isotopic signatures of substrates used for methylotrophic methanogenesis. Two replicates were performed for δ^{13}C-CH_3OH measurements, four replicates were measured for δ^{13}C-sodium acetate and δ^{13}C-TMA·HCl respectively.

	D1	D2	D3	D4
M.b1	-81.96	-85.52	-84.33	-79.02
M.b2	-79.87	-85.45	-83.41	-82.8
M.b3	-81.66	-81.71	-84.96	-82.88
M.b Δmtr MeAc1	-74.47	-78.49	-77.61	-76.92
M.b Δmtr MeAc2	-74.24	-75.23	-77.49	-76.63
M.b Δmtr MeAc3	-60.31	-69.07	-76.19	-77.62
M.b Δmtr $MeH_2$1	-79.44	-79.17	-78.69	-73.36
M.b Δmtr $MeH_2$2	-79.71	-78.93	-77.97	-71.92
M.b Δmtr $MeH_2$3	-79.44	-73.11	-78.1	-72.3
M.a1	-84.68	-62.82	-24.72	-17.73
M.a2	-85.22	-65.15	-21.85	-20.56
M.a3	-85.26	-67.95	-20.75	-19.75
M.m1	-60.77	-56.42	-54.25	-45.78
M.m2	-60.92	-57.43	-57.04	-54.27
M.m3	-60.4	-57.47	-54.79	-51.57

Table 5. ε values calculated based on $\delta^{13}C$-CH_4 and $\delta^{13}C$ of corresponding substrates for the four methanogen strains cultivated under five different cultivation settings. Numbers in red color show the most negative ε values that we use as representative values in open system model calculation.

	D2	D4
M.b1	-41.85	-39.52
M.b2	-33.75	-42.35
M.b3	-36.1	-46.52
M.b ∆mtr MeAc1	-17.21	-20.28
M.b ∆mtr MeAc2	-18.22	-19.9
M.b ∆mtr MeAc3	-21.29	-19.14
M.a1	-15.4	46.92
M.a2	-13.42	54.48
M.a3	-18.92	54.5
M.m1	-25.79	-19.38
M.m2	-26.24	-18.37
M.m3	-24.05	-12.95

Table 6. ε values calculated based on $\delta^{13}C$-(CO_2+DIC) and $\delta^{13}C$ of corresponding substrates for the four methanogen strains cultivated under four different cultivation settings. Numbers in red color show the most negative ε values that we use as representative values in open system model calculation.

Strain	Substrate used for methylotrophic methanogenesis	Average $\delta^{13}C$-CH_4 based ε values	Average $\delta^{13}C$-(CO_2+DIC) based ε values
M. barkeri	methanol	-85.31	-43.57
M. barkeri Δmtr MeAc	methanol+sodium acetate	-77.87	-20.49
M. barkeri Δmtr MeH_2	methanol+H_2	-79.53	NA (no CO_2 production)
M. activorans	methanol	-85.05	-15.91
M. methylutens H_2	TMA	-60.70	-25.36

Table 7. Average $\delta^{13}C$-CH_4 based ε values and $\delta^{13}C$-(CO_2+DIC) based ε values of the four strains under five cultivation settings.

References

Alperin M. J., Blair N. E., Albert D. B., Hoehler T. M. and Martens C. S. (1992) Factors that control the stable carbon isotopic composition of methane produced in an anoxic marine sediment. *Global Biogeochemical Cycles* **6**, 271–291.

Beale R., Dixon J. L., Arnold S. R., Liss P. S. and Nightingale P. D. (2013) Methanol, acetaldehyde, and acetone in the surface waters of the Atlantic Ocean. *Journal of Geophysical Research: Oceans* **118**, 5412–5425.

Bennett R. K., Steinberg L. M., Chen W. and Papoutsakis E. T. (2018) Engineering the bioconversion of methane and methanol to fuels and chemicals in native and synthetic methylotrophs. *Current Opinion in Biotechnology* **50**, 81–93.

Borrel G., O'Toole P. W., Harris H. M. B., Peyret P., Brugère J.-F. and Gribaldo S. (2013) Phylogenomic Data Support a Seventh Order of Methylotrophic Methanogens and Provide Insights into the Evolution of Methanogenesis. *Genome Biology and Evolution* **5**, 1769–1780.

Budd J. A. and Spencer C. P. (1968) The utilisation of alkylated amines by marine bacteria. *Marine Biol.* **2**, 92–101.

Chistoserdova L. and Kalyuzhnaya M. G. (2018) Current Trends in Methylotrophy. *Trends in Microbiology* **26**, 703–714.

Cloern J. E., Foster S. Q. and Kleckner A. E. (2014) Phytoplankton primary production in the world's estuarine-coastal ecosystems. *Biogeosciences* **11**, 2477–2501.

Conrad R. (2005) Quantification of methanogenic pathways using stable carbon isotopic signatures: a review and a proposal. *Organic Geochemistry* **36**, 739–752.

Curson A. R. J., Liu J., Bermejo Martínez A., Green R. T., Chan Y., Carrión O., Williams B. T., Zhang S.-H., Yang G.-P., Bulman Page P. C., Zhang X.-H. and Todd J. D. (2017) Dimethylsulfoniopropionate biosynthesis in marine bacteria and identification of the key gene in this process. *Nat Microbiol* **2**, 1–9.

Deppenmeier U., Blaut M. and Gottschalk G. (1989) Dependence on membrane components of methanogenesis from methyl-CoM with formaldehyde or molecular hydrogen as electron donors. *European Journal of Biochemistry* **186**, 317–323.

Dixon J. L., Beale R. and Nightingale P. D. (2013) Production of methanol, acetaldehyde, and acetone in the Atlantic Ocean. *Geophysical Research Letters* **40**, 4700–4705.

Fischer P. Q., Sánchez-Andrea I., Stams A. J. M., Villanueva L. and Sousa D. Z. (2021) Anaerobic microbial methanol conversion in marine sediments. *Environmental Microbiology* **23**, 1348–1362.

Fricke W. F., Seedorf H., Henne A., Krüer M., Liesegang H., Hedderich R., Gottschalk G. and Thauer R. K. (2006) The Genome Sequence of Methanosphaera stadtmanae Reveals Why This Human Intestinal Archaeon Is Restricted to Methanol and H_2 for Methane Formation and ATP Synthesis. *Journal of Bacteriology* **188**, 642–658.

Galand P. E., Yrjälä K. and Conrad R. (2010) Stable carbon isotope fractionation during methanogenesis in three boreal peatland ecosystems. *Biogeosciences* **7**, 3893–3900.

Gelwicks J. T., Risatti J. B. and Hayes J. M. (1994) Carbon isotope effects associated with aceticlastic methanogenesis. *Applied and Environmental Microbiology* **60**, 467–472.

Gonfiantini R., Stichler W. and Rozanski K. (1995) Standards and intercomparison materials distributed by the International Atomic Energy Agency for stable isotope measurements.

van Grinsven S., Sinninghe Damsté J. S., Harrison J. and Villanueva L. (2020) Impact of Electron Acceptor Availability on Methane-Influenced Microorganisms in an Enrichment Culture Obtained From a Stratified Lake. *Front. Microbiol.* **11**.

Hayes, J. M. (1983). Practice and principles of isotopic measurements in organic geochemistry. *Organic geochemistry of contemporaneous and ancient sediments*, 5, e5.

Hayes, J. M. (2001). Fractionation of carbon and hydrogen isotopes in biosynthetic processes. *Reviews in mineralogy and geochemistry*, 43, 225-278.

Hayes J. (2004) *An Introduction to Isotopic Calculations*., Woods Hole Oceanographic Insitution.

He Z., Cai C., Wang J., Xu X., Zheng P., Jetten M. S. M. and Hu B. (2016) A novel denitrifying methanotroph of the NC10 phylum and its microcolony. *Sci Rep* **6**, 32241.

He Z., Geng S., Cai C., Liu S., Liu Y., Pan Y., Lou L., Zheng P., Xu X. and Hu B. (2015) Anaerobic Oxidation of Methane Coupled to Nitrite Reduction by Halophilic Marine NC10 Bacteria. *Applied and Environmental Microbiology* **81**, 5538–5545.

Hornibrook E. R. C., Longstaffe F. J. and Fyfe W. S. (2000) Evolution of stable carbon isotope compositions for methane and carbon dioxide in freshwater wetlands and other anaerobic environments. *Geochimica et Cosmochimica Acta* **64**, 1013–1027.

Jacob D. J., Field B. D., Li Q., Blake D. R., de Gouw J., Warneke C., Hansel A., Wisthaler A., Singh H. B. and Guenther A. (2005) Global budget of methanol: Constraints from atmospheric observations. *Journal of Geophysical Research: Atmospheres* **110**.

Keller M. D., Kiene R. P., Matrai P. A. and Bellows W. K. (1999) Production of glycine betaine and dimethylsulfoniopropionate in marine phytoplankton. I. Batch cultures. *Marine Biology* **135**, 237–248.

Kiene R. P., Oremland R. S., Catena A., Miller L. G. and Capone D. G. (1986) Metabolism of reduced methylated sulfur compounds in anaerobic sediments and by a pure culture of an estuarine methanogen. *Applied and environmental microbiology* **52**, 1037–45.

King G. M. (1988) Distribution and Metabolism of Quaternary Amines in Marine Sediments. *John Wiley and Sons, Chichester, United Kingdom*.

Kinnaman F. S., Valentine D. L. and Tyler S. C. (2007) Carbon and hydrogen isotope fractionation associated with the aerobic microbial oxidation of methane, ethane, propane and butane. *Geochimica et Cosmochimica Acta* **71**, 271–283.

Krause S. J. E., Liu J., Yousavich D. J., Robinson D., Hoyt D. W., Qin Q., Wenzhöfer F., Janssen F., Valentine D. L. and Treude T. (2023) Evidence of cryptic methane cycling and non-methanogenic methylamine consumption in the sulfate-reducing zone of sediment in the Santa Barbara Basin, California. *Biogeosciences* **20**, 4377–4390.

Krzycki J. A., Kenealy W. R., DeNiro M. J. and Zeikus J. G. (1987) Stable Carbon Isotope Fractionation by Methanosarcina barkeri during Methanogenesis from Acetate, Methanol, or Carbon Dioxide-Hydrogen. *Applied and Environmental Microbiology* **53**, 2597–2599.

Liu Y. and Whitman W. B. (2008) Metabolic, Phylogenetic, and Ecological Diversity of the Methanogenic Archaea. *Annals of the New York Academy of Sciences* **1125**, 171–189.

Millet D. B., Jacob D. J., Custer T. G., de Gouw J. A., Goldstein A. H., Karl T., Singh H. B., Sive B. C., Talbot R. W., Warneke C. and Williams J. (2008) New constraints on terrestrial and oceanic sources of atmospheric methanol. *Atmospheric Chemistry and Physics* **8**, 6887–6905.

Mincer T. J. and Aicher A. C. (2016) Methanol Production by a Broad Phylogenetic Array of Marine Phytoplankton. *PLOS ONE* **11**, e0150820.

O'Neil J. R. (1986) Theoretical and Experimental Aspects of Isotopic Fractionation. *Reviews in Mineralogy* **16**, 1–40.

Oremland R. S. and Polcin S. (1982) Methanogenesis and Sulfate Reduction: Competitive and Noncompetitive Substrates in Estuarine Sediments. *Applied and Environmental Microbiology* **44**, 1270–1276.

Padilla A. M., Loranger S., Kinnaman F. S., Valentine D. L. and Weber T. C. (2019) Modern Assessment of Natural Hydrocarbon Gas Flux at the Coal Oil Point Seep Field, Santa Barbara, California. *Journal of Geophysical Research: Oceans* **124**, 2472–2484.

Padilla C. C., Bristow L. A., Sarode N., Garcia-Robledo E., Gómez Ramírez E., Benson C. R., Bourbonnais A., Altabet M. A., Girguis P. R., Thamdrup B. and Stewart F. J. (2016) NC10 bacteria in marine oxygen minimum zones. *The ISME Journal* **10**, 2067–2071.

Penger J., Conrad R. and Blaser M. (2012) Stable Carbon Isotope Fractionation by Methylotrophic Methanogenic Archaea. *Appl. Environ. Microbiol.* **78**, 7596–7602.

Riemer D., Pos W., Milne P., Farmer C., Zika R., Apel E., Olszyna K., Kliendienst T., Lonneman W., Bertman S., Shepson P. and Starn T. (1998) Observations of nonmethane hydrocarbons and oxygenated volatile organic compounds at a rural site in the southeastern United States. *Journal of Geophysical Research: Atmospheres* **103**, 28111–28128.

Sieburth J. Mcn. and Keller M. D. (1989) Methylaminotrophic Bacteria in Xenic Nanoalgal Cultures: Incidence, Significance, and Role of Methylated Algal Osmoprotectants. *Biological Oceanography* **6**, 383–395.

Stevens C. M. and Engelkemeir A. (1988) Stable carbon isotopic composition of methane from some natural and anthropogenic sources. *Journal of Geophysical Research: Atmospheres* **93**, 725–733.

Summons R. E., Franzmann P. D. and Nichols P. D. (1998) Carbon isotopic fractionation associated with methylotrophic methanogenesis. *Organic Geochemistry* **28**, 465–475.

Timmers P. H. A., Welte C. U., Koehorst J. J., Plugge C. M., Jetten M. S. M. and Stams A. J. M. (2017) Reverse Methanogenesis and Respiration in Methanotrophic Archaea. *Archaea* **2017**, e1654237.

Valentine D. L., Chidthaisong A., Rice A., Reeburgh W. S. and Tyler S. C. (2004) Carbon and hydrogen isotope fractionation by moderately thermophilic

methanogens11Associate editor: N. E. Ostrom. *Geochimica et Cosmochimica Acta* **68**, 1571–1590.

Welander, P. V., & Metcalf, W. W. (2005). Loss of the mtr operon in Methanosarcina blocks growth on methanol, but not methanogenesis, and reveals an unknown methanogenic pathway. *Proceedings of the National Academy of Sciences*, 102(30), 10664-10669.

Zhuang G.-C., Elling F. J., Nigro L. M., Samarkin V., Joye S. B., Teske A. and Hinrichs K.-U. (2016) Multiple evidence for methylotrophic methanogenesis as the dominant methanogenic pathway in hypersaline sediments from the Orca Basin, Gulf of Mexico. *Geochimica et Cosmochimica Acta* **187**, 1–20.

Zhuang G.-C., Heuer V. B., Lazar C. S., Goldhammer T., Wendt J., Samarkin V. A., Elvert M., Teske A. P., Joye S. B. and Hinrichs K.-U. (2018a) Relative importance of methylotrophic methanogenesis in sediments of the Western Mediterranean Sea. *Geochimica et Cosmochimica Acta* **224**, 171–186.

Zhuang G.-C., Lin Y.-S., Bowles M. W., Heuer V. B., Lever M. A., Elvert M. and Hinrichs K.-U. (2017) Distribution and isotopic composition of trimethylamine, dimethylsulfide and dimethylsulfoniopropionate in marine sediments. *Marine Chemistry* **196**, 35–46.

Zhuang G.-C., Montgomery A., Sibert R. J., Rogener M.-K., Samarkin V. A. and Joye S. B. (2018b) Effects of pressure, methane concentration, sulfate reduction activity, and temperature on methane production in surface sediments of the Gulf of Mexico. *Limnology and Oceanography* **63**, 2080–2092.

Appendix. $\delta^{13}C\text{-}CH_4$, $\delta^{13}C\text{-}CO_2$ and $\delta^{13}C$-DIC values of the four methylotrophic methanogen strains under five cultivation conditions, utilizing long-term cultivation setting to approximate a closed system analogue.

Strain and Sampling Day	**$\delta^{13}C\text{-}CH_4$ (‰)**	**$\delta^{13}C\text{-}CO_2$ (‰)**	**$\delta^{13}C$-DIC (‰)**
LMbw2D0	NA	NA	1.36
LMbw3D0	NA	NA	1.86
LMbw2D2	-111.94	-64.60	-53.73
LMbw3D2	-93.91	-65.66	-58.78
LMbw2D5	-49.02	6.37	8.45
LMbw3D5	-47.33	10.47	12.46
LMbw2D8	-52.26	3.27	3.52
LMbw3D8	-48.20	8.12	9.71
LMbw2D10	-46.35	3.63	5.55
LMbw3D10	-45.88	7.78	9.70
LMbw2D12	-46.00	3.31	5.17
LMbw3D12	-47.01	7.42	9.24
LMbw2D13	-45.90	3.19	NA
LMbw3D13	-47.06	7.19	NA
LMbw2D14	-45.64	2.98	4.94
LMbw3D14	-47.12	6.73	8.57
LMbw2D15	-45.93	2.94	NA
LMbw3D15	-47.12	6.29	NA
LMbw2D16	-45.49	2.62	4.33
LMbw3D16	-46.80	5.62	7.56

Table 1. The measured $\delta^{13}C\text{-}CH_4$, $\delta^{13}C\text{-}CO_2$ and $\delta^{13}C$-DIC of two replicates of strain M. b cultivated with methanol in the long-term cultivation setting.

Strain and Sampling Day	$\delta^{13}C$-CH_4 (‰)	$\delta^{13}C$-CO_2 (‰)	$\delta^{13}C$-DIC (‰)
LMbm1MeH2D0	NA	NA	-38.53
LMbm2MeH2D0	NA	NA	-38.23
LMbm3MeH2D0	NA	NA	-38.32
LMbm1MeH2D2	-100.21	-36.91	-34.18
LMbm2MeH2D2	-99.30	-36.76	-34.03
LMbm3MeH2D2	-99.83	-37.55	-35.02
LMbm1MeH2D4	-97.47	-34.24	-31.65
LMbm2MeH2D4	-97.43	-34.36	-31.70
LMbm3MeH2D4	-99.13	-35.01	-32.69
LMbm1MeH2D6	-95.25	-32.12	-29.53
LMbm2MeH2D6	-94.80	-32.48	-29.62
LMbm3MeH2D6	-96.05	-32.86	-30.57
LMbm1MeH2D8	-87.45	-30.01	-27.82
LMbm2MeH2D8	-86.83	-30.13	-27.78
LMbm3MeH2D8	-87.69	-30.02	-28.18
LMbm1MeH2D10	-86.37	-28.14	-26.04
LMbm2MeH2D10	-86.33	-28.63	-26.28
LMbm3MeH2D10	-87.74	-28.61	-26.38
LMbm1MeH2D12	-85.58	-26.30	-24.04
LMbm2MeH2D12	-83.08	-26.90	-24.44
LMbm3MeH2D12	-85.05	-26.83	-24.71
LMbm1MeH2D13	-82.05	-25.68	NA
LMbm2MeH2D13	-81.63	-26.30	NA
LMbm3MeH2D13	-84.38	-26.29	NA
LMbm1MeH2D14	-81.71	-24.98	-22.96
LMbm2MeH2D14	-81.22	-25.72	-23.21
LMbm3MeH2D14	-81.08	-25.55	-23.50
LMbm1MeH2D15	-81.22	-24.27	NA
LMbm2MeH2D15	-80.24	-25.07	NA
LMbm3MeH2D15	-82.84	-24.95	NA
LMbm1MeH2D16	-79.96	-23.68	-21.45
LMbm2MeH2D16	-79.38	-24.54	-21.94
LMbm3MeH2D16	-82.01	-24.49	-22.26

Table 2. The measured $\delta^{13}C$-CH_4, $\delta^{13}C$-CO_2 and $\delta^{13}C$-DIC of two replicates of strain M. b Δmtr cultivated with methanol + H_2 in the long-term cultivation setting.

Strain and Sampling Day	δ^{13}C-CH_4 (‰)	δ^{13}C-CO_2 (‰)	δ^{13}C-DIC (‰)
LMbm1MeAcD0	NA	NA	-47.58
LMbm2MeAcD0	NA	NA	-47.00
LMbm1MeAcD2	-103.27	-60.62	-54.83
LMbm2MeAcD2	-103.68	-59.35	-53.06
LMbm1MeAcD5	-75.79	-54.10	-49.86
LMbm2MeAcD5	-78.09	-53.95	-49.76
LMbm1MeAcD8	-72.00	-49.78	-46.18
LMbm2MeAcD8	-74.75	-49.33	-45.75
LMbm1MeAcD10	-71.87	-49.64	-46.34
LMbm2MeAcD10	-74.86	-49.36	-45.68
LMbm1MeAcD12	-71.87	-49.75	-46.27
LMbm2MeAcD12	-74.84	-49.29	-45.74
LMbm1MeAcD13	-71.84	-49.73	NA
LMbm2MeAcD13	-74.75	-49.33	NA
LMbm1MeAcD14	-71.41	-49.44	-46.12
LMbm2MeAcD14	-74.33	-49.37	-45.73
LMbm1MeAcD15	-71.88	-49.74	NA
LMbm2MeAcD15	-74.56	-49.30	NA
LMbm1MeAcD16	-71.50	-49.70	-46.06
LMbm2MeAcD16	-74.29	-49.18	-45.63

Table 3. The measured δ^{13}C-CH_4, δ^{13}C-CO_2 and δ^{13}C-DIC of three replicates of strain M. b ∆mtr cultivated with methanol + sodium acetate in the long-term cultivation setting.

Strain and Sampling Day	$\delta^{13}C$-CH_4 (‰)	$\delta^{13}C$-CO_2 (‰)	$\delta^{13}C$-DIC (‰)
LMa2D0	NA	NA	5.18
LMa3D0	NA	NA	4.80
LMa2D2	-50.88	4.48	29.10
LMa3D2	-58.03	10.14	43.18
LMa2D4	-44.54	11.97	15.67
LMa3D5	-46.58	15.58	19.06
LMa2D6	-44.19	11.23	15.46
LMa2D8	-30.44	10.12	13.35
LMa3D8	-44.99	15.82	18.67
LMa2D10	-44.86	9.48	12.63
LMa3D10	-46.07	15.59	18.57
LMa2D12	-44.44	9.47	12.73
LMa3D12	-45.17	15.41	18.48
LMa2D13	-44.37	9.56	NA
LMa3D13	-44.84	15.28	NA
LMa2D14	-44.58	9.66	13.10
LMa3D14	-44.89	15.08	17.66
LMa2D15	-44.69	9.62	NA
LMa3D15	-44.76	14.71	NA
LMa2D16	-44.41	9.58	13.57
LMa3D16	-45.31	14.04	16.96

Table 4. The measured $\delta^{13}C$-CH_4, $\delta^{13}C$-CO_2 and $\delta^{13}C$-DIC of two replicates of strain M. a cultivated with methanol in the long-term cultivation setting.

Strain and Sampling Day	$\delta^{13}C$-CH_4 (‰)	$\delta^{13}C$-CO_2 (‰)	$\delta^{13}C$-DIC (‰)
LMm1D0	NA	NA	-8.68
LMm2D0	NA	NA	-10.91
LMm3D0	NA	NA	-9.85
LMm1D2	-89.57	-52.86	-50.56
LMm2D2	-93.23	-41.15	-46.67
LMm3D2	-90.58	-37.28	-45.61
LMm1D5	-54.02	0.80	9.89
LMm2D5	-47.89	9.85	14.81
LMm3D5	-46.50	9.94	14.65
LMm3D8	-44.90	9.49	14.15
LMm1D8	-46.85	10.26	14.91
LMm2D8	-46.48	9.97	14.18
LMm1D10	-44.99	9.37	14.11
LMm2D10	-45.99	10.28	14.86
LMm3D10	-47.36	9.89	14.49
LMm1D12	-46.92	9.37	14.15
LMm2D12	-46.43	10.11	15.02
LMm3D12	-46.10	9.84	14.61
LMm1D13	-46.78	9.36	NA
LMm2D13	-46.49	10.21	NA
LMm3D13	-46.20	9.44	NA
LMm1D14	-46.78	9.35	14.09
LMm2D14	-46.29	10.23	14.97
LMm3D14	-45.92	9.65	14.50
LMm1D15	-46.78	9.34	NA
LMm2D15	-46.32	10.18	NA
LMm3D15	-45.88	9.67	NA
LMm1D16	-47.03	9.25	14.15
LMm2D16	-46.37	10.26	14.92
LMm3D16	-45.76	9.74	14.36

Table 5. The measured $\delta^{13}C$-CH_4, $\delta^{13}C$-CO_2 and $\delta^{13}C$-DIC of three replicates of strain M. m cultivated with TMA in the long-term cultivation setting.